Non-invasive single cell imaging in bacterial biofilms under controlled physicochemical environments

Ji Zhang

Sichuan, China

B.S. in Chemistry, Sichuan University, 2013

M.S. in Analytical Chemistry, Sichuan University, 2016

A Dissertation presented to the Graduate Faculty of the University of Virginia in Candidacy for the Degree of Doctor of Philosophy

Department of Chemistry

University of Virginia

November 2021

Andreas Gahlmann

Ian Harrison

Kateri H. DuBay

Cassandra L. Fraser

Liheng Cai

ACKNOWLEDGEMENTES

As I come to the end of my graduate career, there are many people that I must thank for their help and support in the pursuit of my education.

First, I would like to thank my advisor Dr. Andreas Gahlmann. Through ups and downs of my graduate career, he was always patient and supportive. We worked on many wonderful projects through the years and he was always showing great enthusiasm, which is truly inspiring. His unwavering support for me and our work offers me the success that I've had in my graduate school career. I wish him great success in the future.

It is not possible to tell my story without mentioning my wonderful lab mates. Dr. Mingxing Zhang and I worked closely on the biofilm project since I joined the lab. We worked cooperatively to construct the lattice light sheet microscope, design biofilm imaging protocols and develop microfluidic system. I want to thank Yibo Wang for his help in Rivanna computing system and his great contribution to the bacterial segmentation project. Dr. Jie Wang of the Scott lab gave me lots of support in learning and later developing imaging processing methods for bacterial biofilms. I need to also thank Alecia, I got numerous help from her in biological related issues and we also collaborated on the *Myxococcus xanthus* project. Dr. Ting Yan and I are both excited of learning novel microscopy, and we have lots of deep discussion of the future direction of microscopy. Alecia, Olivia, Josh and Eric gave me generous help when I was writing my dissertation, which I really appreciate. If you find there are more grammar mistakes in the acknowledge part, an obvious reason is that I haven't ask their help in this part. I also want to thank Dr. Charles Richardson and Dr. Jackie Corbitt, two former post-docs, for their great suggestion

not only in the scientific research but also about future career life. I wish them great success in work and life.

My committee members, Dr. Ian Harrison, Dr. Kateri H. DuBay, Dr. Cassandra L. Fraser and Dr. Liheng Cai, need to be mentioned here. I would like to thank them for both overseeing and supporting my research work.

Of course, I need to thank my family, as they have continued to support me throughout my life. Without their support I would never have been able to pursue the level of education that I have and I would not be the person I am today.

Finally, I need to thank my wife, Dr. Yulu Zhang, for her never-ending love and support. I have known her as classmate, roommate, lover and my better half, since I met her. I would not have made it this far without the joy and energy she brings to me.

Abstract

Bacteria commonly live in dense and diverse communities, known as biofilms. As the major mode of microbial life, biofilms have been widely recognized for their impact on global biogeochemical cycling and the health of higher living organisms. Commonly used assays to study biofilm probe biofilm formation and behavior using ensemble averaged data. However, to better understand how the individual behaviors of biofilm dwelling cells contribute to the emergent macroscopic properties of biofilms, cellular level information needs to be extracted from densely packed bacterial biofilms. In this work, we integrated lattice light sheet microscopy (LLSM) and microfluidic systems for non-invasive, high-resolution time-lapse imaging of live bacterial communities under precisely controlled physical and chemical conditions. With this combination, we successfully imaged the colonization of glass surfaces by *S. oneidensis* MR-1 biofilms, a well-studied biofilm formation species, under media flow over a time period of three days, visualizing the evolution of single surface-attached cells into a dense 3D biofilm. To quantitatively analyze biofilm-dwelling cells, we developed Bacterial Cell Morphometry 3D (*BCM3D*), an integrated image analysis package that combines deep learning with conventional image analysis, and its novel extension version *BCM3D 2.0,* which enables measurement of cellular phenotypes such as cell size and distance to the nearest neighboring cell. With this quantitative analysis ability, we demonstrated that the presence of bile salts leads to aggregation of *S. flexneri*, an intracellular pathogen that causes watery or bloody diarrhea, at a cellular level, which had previously only been shown at an ensemble level. This cellular level imaging and analysis ability enables us to study the emergent properties of bacterial biofilms in terms of the fully-resolved behavioral phenotypes of individual cells, which provides a more complete understanding of bacterial biofilms.

Contents

Chapter 1 Introduction

1.1 Overview

Bacteria commonly live in dense and diverse communities, named biofilms, which colonize various biotic and abiotic surfaces[1-3]. As the major mode of microbial life, biofilms have been widely recognized for their impact on the global biogeochemical cycling[4-6] and the health of higher living organisms[7-9], including humans. Stream biofilms[4], the major mode of microbial life in streams and rivers for example, contribute substantially to the nitrogen cycle by denitrifying streams and emitting the resulting nitrogen gas or nitrous oxide into the atmosphere. Besides the nitrogen cycle, stream biofilms are also recognized as substantial contributors to the global carbon flux by degrading organic matter and ultimately emitting a large amount of carbon dioxide into the atmosphere, which makes them an indispensable component of global biogeochemical fluxes. In human health, commensal biofilms benefit us by warding off pathogens, performing key digestive functions, and being directly involved in host homeostasis[10]. On the other hand, biofilms are responsible for 75% of human microbial infection in medical treatments[11]. In American hospitals alone, these biofilm infections account for over 1 million healthcare related infections and an estimated 100,000 deaths per year[12].

Dense multicellular communities promote intimate interaction and phenotypic diversity among individual cells. Phenotypic behaviors, such as gene expression or growth rate, vary dramatically in spatial and temporal scales among biofilms[13, 14]. Phenotypic diversity and coordination of cellular behaviors provide bacterial biofilms with emergent functional capabilities beyond those of planktonic cells through division of labor and nutrient sharing strategies[1, 15, 16]. In fact, owing to their cooperative and collective behaviors, biofilm-dwelling cells have shown

substantial advantages compared to planktonic cells, including a higher resilience against external threats[7, 17] and an increased efficiency in digesting complex nutrients[15, 18].

To enable either efficient suppression of pathogenic biofilm formations or sufficient utilization of beneficial properties of biofilms, it is necessary to better understand how macroscopic biofilm properties, such as its biochemical metabolism and its geometry shape, emerge from the collective behaviors of individual cells. Specifically, we need to understand the cellular biochemical and mechanical mechanisms used by biofilm-dwelling cells to cooperate or antagonize each other in temporally and spatially heterogeneous biofilm microenvironments[19-21]. To gain this understanding, non-invasive imaging systems and powerful image analysis methods that are capable of resolving and tracking individual cells in 3D dense biofilms are required.

1.2 Biofilm constitution

As the term biofilm suggests, the microorganisms in biofilms are encased in a self-produced extracellular matrix, known as extracellular polymeric substances (EPS). In fact, in most biofilms, the microorganisms only account for less than 10% of the dry mass, whereas EPS can account for more than 90%[22]. As the major component of biofilms, EPS forms the scaffold for the three-dimensional structure of biofilms and provides an immediate environment for biofilm-dwelling cells, which enables a lifestyle that is entirely different from the planktonic state.

Though important, our current understanding of EPS is still at a very early stage[23]. In fact, EPS were initially denoted as ‘extracellular polysaccharides’ but redefined, as it is clear that the matrix also contains DNAs, proteins and other biopolymers such as lipids[24]. Although the precise functions and molecule level interactions of the various matrix components are still poorly understood[25], several functions of EPS have been determined, showcasing the benefits of the biofilm lifestyle. Extracellular enzymes, for example, make the matrix act as an external digestive

system that breaks down polymers, like trapped organic particles[22], into low-molecular mass products that can then be utilized by biofilm-dwelling cells as energy and carbon sources. As a major fraction of the EPS matrix[26], polysaccharides are responsible for the mechanical stability of biofilms and are involved in the maintenance of biofilm architecture[27], which provides biofilms with better tolerance towards mechanical stress, such as shear forces[3]. Extracellular DNA is also a major structural component in some biofilms[28], for example, the formation of *P.aeruginosa* biofilms is inhibited by DNase[29]. Put simply, these EPS components work closely with each other, providing biofilm-dwelling cells substantial advantages compared with solitary cells. Though important for biofilms, EPS could be a problem in biofilm imaging, as the light scattering caused by them will result in lower signal and higher background[30], thus presenting an additional challenge for imaging biofilms with sufficient resolution and contrast to monitor individual cells.

1.3 Biofilm imaging

Optical microscopy has long been an important tool for characterizing and understanding microbial communities. A key advantage of optical microscopy over other techniques, such as electron microscopy, for characterizing microbes is that it is capable of monitoring live cells[31]. Among various optical microscopies, fluorescence microscopy, which combines high spatial-temporal resolution with highly specific fluorescence probes[32, 33], provides a unique way to study the spatial and temporal contexts that affect cellular behaviors in biofilm environments.

For simple systems, such as monolayer bacterial communities on surfaces, imaging is straightforward. With proper sample preparation, a simple wide-field fluorescence microscope is adequate for obtaining cellular level images with high temporal resolution. In fact, with properly designed experiments, many important properties of biofilms, such as inter-bacterial signaling[34], periodic growth of biofilms[21], have been revealed by using wide-field fluorescence microscopy.

Most bacterial biofilms of interest, however, are more challenging to image. The most obvious obstacle is dimensionality. Without the ability to block out-of-focus light, wide-field microscopy is not able to resolve the intrinsic 3D structure of biofilms[35]. In addition, fast dynamics and long developing time of biofilms also requires fast acquisition speeds and a long imaging duration. Confocal microscopy, the current standard approach to 3D fluorescence imaging, makes use of a pinhole conjugate to the focal point to filter out-of-focus light and only allow signal from the focal point to reach the detector[36]. While versatile and powerful, it suffers from limitations in acquisition speeds and photodamage[37, 38]. As any information is collected from a single point, constructing a 3D image requires scanning this point through all three spatial dimensions. This issue can be partially resolved by parallelizing with multi pinholes, but nonetheless creates limitations on overall acquisition speed[39, 40]. More importantly, though useful information is obtained from the focal point, the entire biofilm is under repeated and strong illumination. This inefficient use of the photon budget leads to severe phototoxicity as well as photobleaching, which limits total imaging duration and temporal resolution[41, 42].

Light sheet fluorescence microscopy, in contrast, utilizes a separate excitation lens perpendicular to the wide-field detection objective to confine the illumination to the vicinity of the focal plane by generating a thin light sheet and is thus more photon efficient[38, 43]. Constructing 3D images only requires scanning the light sheet along the axial axis of the detection objective thus enabling high speed acquisition. Furthermore, as illumination light is evenly distributed along the focal plane rather than concentrated at a single point, the illumination intensity of light sheet microscopy is much lower than that of confocal microscopy, which significantly reduces photodamage[38, 42, 44, 45]. With these characteristics and newly achieved high spatial resolution, light

sheet microscopy has become a unique non-invasive high spatial-temporal resolution imaging technique for not only biofilms but also the overall microbial world[46, 47].

1.4 Sample system for biofilm imaging

In addition to a non-invasive imaging technique, a suitable device that can provide a proper environment for biofilms is also required for live imaging[48-50]. Among various biofilm formation devices, microtiter plates or microwell plates have long been the most commonly used due to their low cost and ease of use. However, microwell plates can only provide static environments, which limits their ability to mimic natural environments and achieve long term imaging[51]. Furthermore, due to the non-custom forms of microwell plates, it is extremely difficult to integrate them into the limited sample space of a conventional light sheet microscope[52, 53].

Luckily, microfluidic devices, which combine easily changeable flow conditions and various custom forms, now provide a promising platform for live bacterial biofilm imaging [54, 55]. The continuous flow not only provides a continuous supply of nutrients that is necessary for biofilms' long-term growth, but also presents opportunities for studying effects of hydrodynamics on biofilm formation[56, 57]. Furthermore, customizable microfluidic systems can mimic various conditions, which enable us to study biofilms in various conditions and their responses to environmental change. In fact, many important properties have been revealed by imaging biofilms in microfluidic systems. For example, Nadell *et al.* demonstrated that matrix organization and hydrodynamic flow interact to shape competitive dynamics in *P. aeruginosa* biofilms by imaging biofilms under conditions that mimical natural flow[58]. Similarly, Singh *et al*. have shown that biofilm-dwelling *V. cholerae* cells integrate nutrient starvation pathways and quorum sensing to govern active dispersal by imaging biofilms in various flow and nutrient conditions[59]. Ultimately,

as an easily customizable device, microfluidic devices can be integrated with various imaging systems including light sheet microscopy[60].

1.5 Biofilm imaging analysis

Combining the non-invasive imaging technique with the microfluidic system allows for long duration, high resolution imaging of biofilms. Indeed, lattice light sheet microscopy (LLSM) can be combined with microfluidic systems to provide unique information about biofilms, including long term growth dynamics of biofilms, 3D complex structure of mature biofilms, and quick motion of bacteria within biofilms. After the acquisition of fluorescence images, the extraction of quantitative information from such images is a crucial step in the imaging analysis[31]. In order to quantitatively analyze biofilm-dwelling cells, each individual cell needs to be detected from images, and this is typically referred to as segmentation[61]. To this end, image processing pipelines based on intensity thresholding and the watershed algorithm have been developed over the years[31]. These pipelines have shown their ability to achieve reasonable single-cell segmentations at certain conditions[55, 62, 63]. Their wide applicability is limited, however, because reasonable segmentations from these pipelines require manual optimization of many user selected parameters. Usually, these parameters need to be optimized according to characteristics of input images, such as image backgrounds, cell sizes, cell densities and signal-to-background ratios (SBRs)[64]. As a result, especially when SBRs are low, cell densities high, and fluorescence intensity not uniform across cells, even with optimal parameters, these imaging processing pipelines often only produce suboptimal segmentation results[30, 65].

To overcome the limitations of traditional image analysis approaches, deep learning methods, such as convolutional neural networks (CNNs), have been used in recent years with great success not only in biofilm image analysis but also in general biology image analysis[66]. Given

sufficient training data and computing resources, a properly designed CNN can achieve highly accurate segmentation results on a wide variety of cell and image types[67-69]. For object detection tasks, training data are typically composed of raw data and its corresponding segmentation in which the position of each cell is annotated. However, obtaining sufficient training data is not a trivial task. When using experimentally acquired images as raw data in training pairs, this ground truth usually needs to be obtained through manual annotation, a labor-intensive task that simply becomes impossible when thousands or even more cells need to be annotated, which is very common in biofilm data[70, 71]. Besides, it is noteworthy that manual annotation is not free from errors and uncertainty[31, 65]. Inaccuracies in training data can be inherited by the CNNs and cause systematic errors in segmentation results.

An alternative way to generate sufficient training data without any manual annotation is to provide simulated training data rather than experimentally obtained images. With simulated training data, flawless ground truth is automatically available, as spatial arrangements among individual cells are known precisely and accurately[30, 72]. It is worth noting that current methods do have some limitations, such as spatial differences of background and resolution potentially not being reflected in the simulated images, thus examples of training CNNs with simulated data is still rare. Fortunately, recently developed deep learning based image transfer methods, such as CycleGAN, have shown their potential for resolving these limitations[73, 74].

With the introduction of user-friendly tools, now even a non-expert user can easily manipulate and train CNNs, which allows CNNs based image processing to be widely used in microbiology studies[75, 76]. In addition, CNNs or machine learning methods in general don't necessarily need to be used alone; combined with the conventional image processing methods, more efficient image analysis pipelines are now available[30, 77].

1.6 Shigella flexneri biofilm

S. flexneri is an intracellular pathogen that causes watery or bloody diarrhea by invading epithelial cells in the colonic mucosa[78, 79]. Though many aspects of the *S. flexneri* invasion process have been thoroughly studied, there is a significant knowledge gap in how the bacterium survives during host gastrointestinal transit, where it is exposed to numerous hazardous factors such as antimicrobial peptides, proteases, and particularly bile salts in the small intestine[80-84]. As an essential component of digestion, the amphipathic structure of bile salts results in detergent-like properties that provide antimicrobial activity by compromising bacterial membrane integrity[85]. Recent studies have indicated the possibility of *S. flexneri* using biofilm formation as a survival strategy in the presence of bile salts[83, 86]. Though biofilm formation is a commonly adaptive trait of microorganisms under harsh conditions, previous studies have shown that *S. flexneri* lacks various adherence factors that are thought to be important to biofilm formation, including type 1 fimbria, flagella, and Type IV [86, 87]. Thus, this observation may reveal some different mechanisms utilized by microorganisms in biofilm formation. However, current studies of *S. flexneri* biofilms are limited to static culture conditions and ensemble-level analysis[83, 86]. To further confirm biofilm formation of *S. flexneri* in the presence of bile salts, an experiment performed at biologically relevant conditions with single cell level information of live *S. flexneri* biofilms is necessary. Our above-mentioned tools are well matched with these experimental requirements, and some preliminary results of *S. flexneri* biofilm formation in the presence of bile salts have been obtained.

1.7 Dissertation overview

A non-invasive 3D imaging system with advanced computational image analysis algorithms enables studies of live 3D bacterial biofilms at the cellular level. In this dissertation,

descriptions of the non-invasive 3D imaging system will be divided into two chapters, **Chapter 2** and **Chapter 3**. While **Chapter 2** will detail the imaging platform, the LLSM, **Chapter 3** will describe the LLSM integrated flow system that provides suitable environmental conditions for biofilm imaging. **Chapter 4** and **5** will move to the computational image analysis part, covering *BCM3D 1.0*, *BCM3D 2.0*, respectively, both automatic image analysis workflows that can extract cellular information of 3D biofilms. In **Chapter 6**, I will describe how we combine and apply these methods for the study of *S. flexneri* biofilm. Finally, significance and future directions of the work will be discussed in **Chapter 7**.

References

1. Nadell, C. D.; Drescher, K.; Foster, K. R., Spatial structure, cooperation and competition in biofilms. *Nature Reviews Microbiology* **2016,** *14* (9), 589-600.

2. Jayathilake, P. G.; Gupta, P.; Li, B., et al., A mechanistic Individual-based Model of microbial communities. *PloS one* **2017,** *12* (8), e0181965.

3. Persat, A.; Nadell, C. D.; Kim, M. K., et al., The mechanical world of bacteria. *Cell* **2015,** *161* (5), 988-997.

4. Battin, T. J.; Besemer, K.; Bengtsson, M. M., et al., The ecology and biogeochemistry of stream biofilms. *Nature Reviews Microbiology* **2016,** *14* (4), 251-263.

5. Lyon, D. R.; Ziegler, S. E., Carbon cycling within epilithic biofilm communities across a nutrient gradient of headwater streams. *Limnology and Oceanography* **2009,** *54* (2), 439-449.

6. Flemming, H.-C.; Wingender, J.; Szewzyk, U., et al., Biofilms: an emergent form of bacterial life. *Nature Reviews Microbiology* **2016,** *14* (9), 563-575.

7. De la Fuente-Núñez, C.; Reffuveille, F.; Fernández, L., et al., Bacterial biofilm development as a multicellular adaptation: antibiotic resistance and new therapeutic strategies. *Current opinion in microbiology* **2013,** *16* (5), 580-589.

8. Hall-Stoodley, L.; Costerton, J. W.; Stoodley, P., Bacterial biofilms: from the natural environment to infectious diseases. *Nature reviews microbiology* **2004,** *2* (2), 95-108.

9. Dewhirst, F. E.; Chen, T.; Izard, J., et al., The human oral microbiome. *Journal of bacteriology* **2010,** *192* (19), 5002-5017.

10. García-Bayona, L.; Comstock, L. E., Bacterial antagonism in host-associated microbial communities. *Science* **2018,** *361* (6408).

11. Miquel, S.; Lagrafeuille, R.; Souweine, B., et al., Anti-biofilm activity as a health issue. *Frontiers in microbiology* **2016,** *7*, 592.

12. Bryers, J. D., Medical biofilms. *Biotechnology and bioengineering* **2008,** *100* (1), 1-18.

13. Donlan, R. M., Biofilms: microbial life on surfaces. *Emerging infectious diseases* **2002,** *8* (9), 881.

14. Stewart, P. S.; Franklin, M. J., Physiological heterogeneity in biofilms. *Nature Reviews Microbiology* **2008,** *6* (3), 199-210.

15. Drescher, K.; Nadell, C. D.; Stone, H. A., et al., Solutions to the public goods dilemma in bacterial biofilms. *Current Biology* **2014,** *24* (1), 50-55.

16. Nadell, C. D.; Xavier, J. B.; Foster, K. R., The sociobiology of biofilms. *FEMS microbiology reviews* **2008,** *33* (1), 206-224.

17. Matz, C.; McDougald, D.; Moreno, A. M., et al., Biofilm formation and phenotypic variation enhance predation-driven persistence of Vibrio cholerae. *Proceedings of the National Academy of Sciences* **2005,** *102* (46), 16819-16824.

18. Meibom, K. L.; Li, X. B.; Nielsen, A. T., et al., The Vibrio cholerae chitin utilization program. *Proceedings of the National Academy of Sciences* **2004,** *101* (8), 2524-2529.

19. Bjarnsholt, T.; Alhede, M.; Alhede, M., et al., The in vivo biofilm. *Trends in microbiology* **2013,** *21* (9), 466-474.

20. Fredrickson, J. K., Ecological communities by design. *Science* **2015,** *348* (6242), 1425-1427.

21. Liu, J.; Prindle, A.; Humphries, J., et al., Metabolic co-dependence gives rise to collective oscillations within biofilms. *Nature* **2015,** *523* (7562), 550-554.

22. Flemming, H.-C.; Wingender, J., The biofilm matrix. *Nature reviews microbiology* **2010,** *8* (9), 623-633.

23. Flemming, H.-C.; Neu, T. R.; Wozniak, D. J., The EPS matrix: the "house of biofilm cells". *J. Bacteriol.* **2007,** *189* (22), 7945-7947.

24. Wingender, J.; Neu, T. R.; Flemming, H.-C., What are bacterial extracellular polymeric substances? In *Microbial extracellular polymeric substances*, Springer: 1999; pp 1-19.

25. Karatan, E.; Watnick, P., Signals, regulatory networks, and materials that build and break bacterial biofilms. *Microbiology and molecular biology reviews* **2009,** *73* (2), 310-347.

26. Wingender, J.; Strathmann, M.; Rode, A., et al., [25] Isolation and biochemical characterization of extracellular polymeric substances from Pseudomonas aeruginosa. *Methods in enzymology* **2001,** *336*, 302-314.

27. Danese, P. N.; Pratt, L. A.; Kolter, R., Exopolysaccharide production is required for development of Escherichia coli K-12 biofilm architecture. *J. Bacteriol.* **2000,** *182* (12), 3593-3596.

28. Izano, E. A.; Amarante, M. A.; Kher, W. B., et al., Differential roles of poly-N-acetylglucosamine surface polysaccharide and extracellular DNA in Staphylococcus aureus and Staphylococcus epidermidis biofilms. *Applied and environmental microbiology* **2008,** *74* (2), 470-476.

29. Whitchurch, C. B.; Tolker-Nielsen, T.; Ragas, P. C., et al., Extracellular DNA required for bacterial biofilm formation. *Science* **2002,** *295* (5559), 1487-1487.

30. Zhang, M.; Zhang, J.; Wang, Y., et al., Non-invasive single-cell morphometry in living bacterial biofilms. *Nature communications* **2020,** *11* (1), 1-13.

31. Jeckel, H.; Drescher, K., Advances and opportunities in image analysis of bacterial cells and communities. *FEMS Microbiology Reviews* **2020**.

32. Power, R. M.; Huisken, J., A guide to light-sheet fluorescence microscopy for multiscale imaging. *Nature methods* **2017,** *14* (4), 360-373.

33. Specht, E. A.; Braselmann, E.; Palmer, A. E., A critical and comparative review of fluorescent tools for live-cell imaging. *Annual review of physiology* **2017,** *79*, 93-117.

34. Humphries, J.; Xiong, L.; Liu, J., et al., Species-independent attraction to biofilms through electrical signaling. *Cell* **2017,** *168* (1-2), 200-209. e12.

35. Neil, M. A.; Juškaitis, R.; Wilson, T., Method of obtaining optical sectioning by using structured light in a conventional microscope. *Optics letters* **1997,** *22* (24), 1905-1907.

36. Jonkman, J.; Brown, C. M.; Wright, G. D., et al., Tutorial: guidance for quantitative confocal microscopy. *Nature protocols* **2020,** *15* (5), 1585-1611.

37. Keller, P. J.; Schmidt, A. D.; Wittbrodt, J., et al., Reconstruction of zebrafish early embryonic development by scanned light sheet microscopy. *science* **2008,** *322* (5904), 1065-1069.

38. Stelzer, E. H., Light-sheet fluorescence microscopy for quantitative biology. *Nature methods* **2015,** *12* (1), 23-26.

39. Oreopoulos, J.; Berman, R.; Browne, M., Spinning-disk confocal microscopy: present technology and future trends. *Methods in cell biology* **2014,** *123*, 153-175.

40. Gräf, R.; Rietdorf, J.; Zimmermann, T., Live cell spinning disk microscopy. *Microscopy techniques* **2005**, 57-75.

41. Laissue, P. P.; Alghamdi, R. A.; Tomancak, P., et al., Assessing phototoxicity in live fluorescence imaging. *Nature methods* **2017,** *14* (7), 657-661.

42. Jemielita, M.; Taormina, M. J.; DeLaurier, A., et al., Comparing phototoxicity during the development of a zebrafish craniofacial bone using confocal and light sheet fluorescence microscopy techniques. *Journal of biophotonics* **2013,** *6* (11-12), 920-928.

43. Olarte, O. E.; Andilla, J.; Gualda, E. J., et al., Light-sheet microscopy: a tutorial. *Advances in Optics and Photonics* **2018,** *10* (1), 111-179.

44. Gao, L.; Shao, L.; Higgins, C. D., et al., Noninvasive imaging beyond the diffraction limit of 3D dynamics in thickly fluorescent specimens. *Cell* **2012,** *151* (6), 1370-1385.

45. Chen, B.-C.; Legant, W. R.; Wang, K., et al., Lattice light-sheet microscopy: imaging molecules to embryos at high spatiotemporal resolution. *Science* **2014,** *346* (6208).

46. Parthasarathy, R., Monitoring microbial communities using light sheet fluorescence microscopy. *Current opinion in microbiology* **2018,** *43*, 31-37.

47. Qin, B.; Fei, C.; Bridges, A. A., et al., Cell position fates and collective fountain flow in bacterial biofilms revealed by light-sheet microscopy. *Science* **2020,** *369* (6499), 71-77.

48. Thormann, K. M.; Saville, R. M.; Shukla, S., et al., Induction of rapid detachment in Shewanella oneidensis MR-1 biofilms. *Journal of bacteriology* **2005,** *187* (3), 1014-1021.

49. Crusz, S. A.; Popat, R.; Rybtke, M. T., et al., Bursting the bubble on bacterial biofilms: a flow cell methodology. *Biofouling* **2012,** *28* (8), 835-842.

50. Goeres, D. M.; Hamilton, M. A.; Beck, N. A., et al., A method for growing a biofilm under low shear at the air–liquid interface using the drip flow biofilm reactor. *Nature protocols* **2009,** *4* (5), 783-788.

51. Azeredo, J.; Azevedo, N. F.; Briandet, R., et al., Critical review on biofilm methods. *Critical reviews in microbiology* **2017,** *43* (3), 313-351.

52. Barner, L. A.; Glaser, A. K.; Huang, H., et al., Multi-resolution open-top light-sheet microscopy to enable efficient 3D pathology workflows. *Biomedical Optics Express* **2020,** *11* (11), 6605-6619.

53. Voleti, V.; Patel, K. B.; Li, W., et al., Real-time volumetric microscopy of in vivo dynamics and large-scale samples with SCAPE 2.0. *Nature methods* **2019,** *16* (10), 1054-1062.

54. Kim, J.; Hegde, M.; Kim, S. H., et al., A microfluidic device for high throughput bacterial biofilm studies. *Lab on a Chip* **2012,** *12* (6), 1157-1163.

55. Hartmann, R.; Singh, P. K.; Pearce, P., et al., Emergence of three-dimensional order and structure in growing biofilms. *Nature physics* **2019,** *15* (3), 251-256.

56. Janakiraman, V.; Englert, D.; Jayaraman, A., et al., Modeling growth and quorum sensing in biofilms grown in microfluidic chambers. *Annals of biomedical engineering* **2009,** *37* (6), 1206-1216.

57. Thomen, P.; Robert, J.; Monmeyran, A., et al., Bacterial biofilm under flow: first a physical struggle to stay, then a matter of breathing. *PloS one* **2017,** *12* (4), e0175197.

58. Nadell, C. D.; Ricaurte, D.; Yan, J., et al., Flow environment and matrix structure interact to determine spatial competition in Pseudomonas aeruginosa biofilms. *Elife* **2017,** *6*, e21855.

59. Singh, P. K.; Bartalomej, S.; Hartmann, R., et al., Vibrio cholerae combines individual and collective sensing to trigger biofilm dispersal. *Current Biology* **2017,** *27* (21), 3359-3366. e7.

60. Fan, Y.-J.; Hsieh, H.-Y.; Tsai, S.-F., et al., Microfluidic channel integrated with a lattice lightsheet microscopic system for continuous cell imaging. *Lab on a Chip* **2021,** *21* (2), 344-354.

61. Caicedo, J. C.; Cooper, S.; Heigwer, F., et al., Data-analysis strategies for image-based cell profiling. *Nature methods* **2017,** *14* (9), 849-863.

62. Drescher, K.; Dunkel, J.; Nadell, C. D., et al., Architectural transitions in Vibrio cholerae biofilms at single-cell resolution. *Proceedings of the National Academy of Sciences* **2016,** *113* (14), E2066-E2072.

63. Yan, J.; Sharo, A. G.; Stone, H. A., et al., Vibrio cholerae biofilm growth program and architecture revealed by single-cell live imaging. *Proceedings of the National Academy of Sciences* **2016,** *113* (36), E5337-E5343.

64. Caicedo, J. C.; Goodman, A.; Karhohs, K. W., et al., Nucleus segmentation across imaging experiments: the 2018 Data Science Bowl. *Nature methods* **2019,** *16* (12), 1247-1253.

65. Dima, A. A.; Elliott, J. T.; Filliben, J. J., et al., Comparison of segmentation algorithms for fluorescence microscopy images of cells. *Cytometry Part A* **2011,** *79* (7), 545-559.

66. Moen, E.; Bannon, D.; Kudo, T., et al., Deep learning for cellular image analysis. *Nat Methods* **2019**.

67. Falk, T.; Mai, D.; Bensch, R., et al., U-Net: deep learning for cell counting, detection, and morphometry. *Nat Methods* **2019,** *16* (1), 67-70.

68. Stringer, C.; Wang, T.; Michaelos, M., et al., Cellpose: a generalist algorithm for cellular segmentation. *Nature Methods* **2021,** *18* (1), 100-106.

69. Weigert, M.; Schmidt, U.; Haase, R., et al. In *Star-convex polyhedra for 3d object detection and segmentation in microscopy*, Proceedings of the IEEE/CVF Winter Conference on Applications of Computer Vision, 2020; pp 3666-3673.

70. Hollandi, R.; Diósdi, Á.; Hollandi, G., et al., AnnotatorJ: an ImageJ plugin to ease hand annotation of cellular compartments. *Molecular biology of the cell* **2020,** *31* (20), 2179-2186.

71. Shorten, C.; Khoshgoftaar, T. M., A survey on image data augmentation for deep learning. *Journal of Big Data* **2019,** *6* (1), 1-48.

72. Helgadottir, S.; Argun, A.; Volpe, G., Digital video microscopy enhanced by deep learning. *Optica* **2019,** *6* (4), 506-513.

73. Fu, C.; Lee, S.; Joon Ho, D., et al. In *Three dimensional fluorescence microscopy image synthesis and segmentation*, Proceedings of the IEEE conference on computer vision and pattern recognition workshops, 2018; pp 2221-2229.

74. Ma, Z.; Wang, F.; Wang, W., et al., Deep learning for in vivo near-infrared imaging. *Proceedings of the National Academy of Sciences* **2021,** *118* (1).

75. Berg, S.; Kutra, D.; Kroeger, T., et al., Ilastik: interactive machine learning for (bio) image analysis. *Nature Methods* **2019,** *16* (12), 1226-1232.

76. Von Chamier, L.; Jukkala, J.; Spahn, C., et al., ZeroCostDL4Mic: an open platform to simplify access and use of Deep-Learning in Microscopy. *BioRxiv* **2020**.

77. Scherr, T.; Löffler, K.; Böhland, M., et al., Cell segmentation and tracking using CNN-based distance predictions and a graph-based matching strategy. *Plos One* **2020,** *15* (12), e0243219.

78. Jennison, A. V.; Verma, N. K., Shigella flexneri infection: pathogenesis and vaccine development. *FEMS microbiology reviews* **2004,** *28* (1), 43-58.

79. Pizarro-Cerdá, J.; Charbit, A.; Enninga, J., et al. In *Manipulation of host membranes by the bacterial pathogens Listeria, Francisella, Shigella and Yersinia*, Seminars in cell & developmental biology, Elsevier: 2016; pp 155-167.

80. Schroeder, G. N.; Hilbi, H., Molecular pathogenesis of Shigella spp.: controlling host cell signaling, invasion, and death by type III secretion. *Clinical microbiology reviews* **2008,** *21* (1), 134-156.

81. Zumsteg, A. B.; Goosmann, C.; Brinkmann, V., et al., IcsA is a Shigella flexneri adhesin regulated by the type III secretion system and required for pathogenesis. *Cell host & microbe* **2014,** *15* (4), 435-445.

82. Bernardini, M. L.; Mounier, J.; d'Hauteville, H., et al., Identification of icsA, a plasmid locus of Shigella flexneri that governs bacterial intra-and intercellular spread through interaction with F-actin. *Proceedings of the National Academy of Sciences* **1989,** *86* (10), 3867-3871.

83. Nickerson, K. P.; Chanin, R. B.; Sistrunk, J. R., et al., Analysis of Shigella flexneri resistance, biofilm formation, and transcriptional profile in response to bile salts. *Infection and immunity* **2017,** *85* (6), e01067-16.

84. Sistrunk, J. R.; Nickerson, K. P.; Chanin, R. B., et al., Survival of the fittest: how bacterial pathogens utilize bile to enhance infection. *Clinical microbiology reviews* **2016,** *29* (4), 819-836.

85. Begley, M.; Gahan, C. G.; Hill, C., The interaction between bacteria and bile. *FEMS microbiology reviews* **2005,** *29* (4), 625-651.

86. Köseoğlu, V. K.; Hall, C. P.; Rodríguez-López, E. M., et al., The autotransporter IcsA promotes Shigella flexneri biofilm formation in the presence of bile salts. *Infection and immunity* **2019,** *87* (7), e00861-18.

87. Chanin, R. B.; Nickerson, K. P.; Llanos-Chea, A., et al., Shigella flexneri adherence factor expression in in vivo-like conditions. *Msphere* **2019,** *4* (6), e00751-19.

Chapter 2 Lattice Light Sheet Microscopy (LLSM)

2.1 Introduction

Live cell compatible imaging provides a window into the spatially complex, rapidly evolving dynamics of biofilms that fixed-cell imaging cannot[1, 2]. However, observing these dynamics directly involves inevitable tradeoffs of spatial resolution, temporal resolution and phototoxicity[3, 4]. Confocal microscopy, the most commonly used imaging modality for biofilms, is able to provide 3D volumes of biofilms at single cell resolution, yet it is not able to monitor fast dynamics of individual cells within biofilms over extended periods of time[5, 6]. This is due to the fact that confocal microscopy illuminates the whole thickness of the specimen, though useful information is only obtained from a single focal point[7, 8] (**Figure 2.1a**). This fact not only results in wasting of photon budget but also leads to premature phototoxicity and photobleaching, limiting imaging duration and altering the physiological state of the specimen[9, 10].

To overcome the drawbacks of confocal microscopy, light sheet-based fluorescence excitation and imaging approaches have been developed in recent years[11-13]. Unlike confocal microscopy, which uses the same objective for illumination and detection, light sheet microscopy generally uses a separate excitation lens perpendicular to the wide-field detection lens to confine the illumination to the vicinity of the focal plane[14, 15] (**Figure 2.1b**). The thinness of the light sheet leads to high axial resolution and negligible phototoxicity, photobleaching and background outside of the focal plane[16, 17]. Furthermore, as it simultaneously illuminates the entire field of view (FOV), fast 3D volume acquisition is able to be achieved with low peak excitation intensities through plane by plane scanning, which not only achieves high temporal resolution but also minimizes

phototoxicity and photobleaching within the focal plane[7, 9]. However, conventional light sheets created from Gaussian beams are limited by the fact that uniform thickness area is limited by the Rayleigh range and further related with the beam waist. Thus, there is always a tradeoff between the thickness of light sheets and the FOV of images[14].

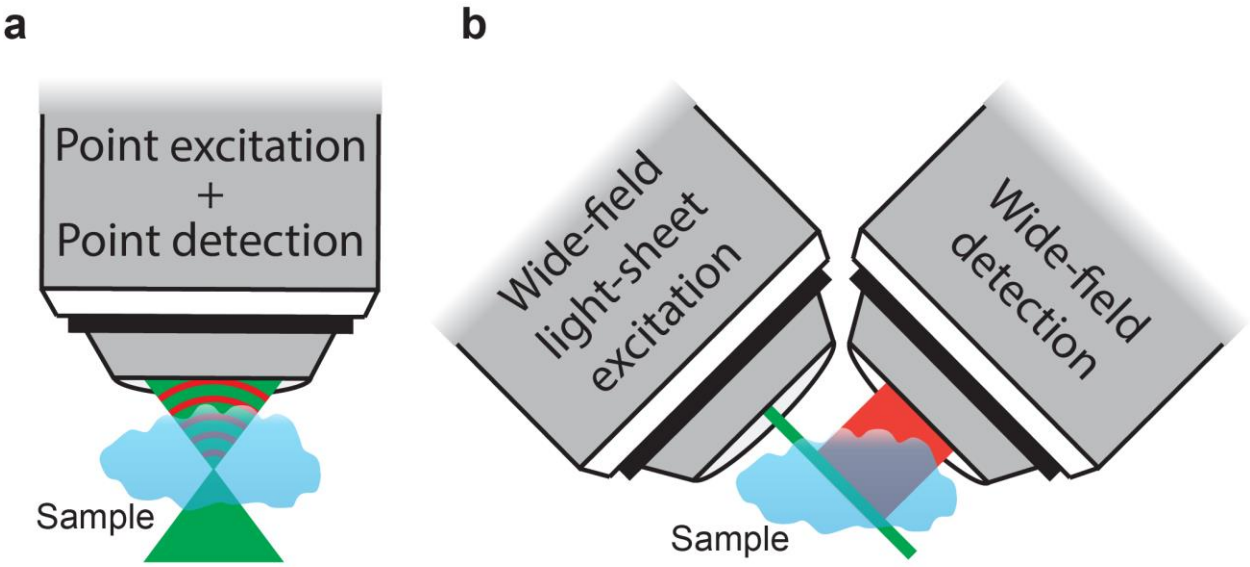

Figure 2.1 Comparison of confocal and light sheet microscopy. (a) In confocal microscopy, fluorescence excitation (green) is confined to cones of light that repeatedly illuminate the sample (blue) during laser scanning, though useful fluorescence signal (red) only comes from the focal point. (b) In light sheet microscopy fluorescence excitation and detection is confined to a single plane that section through the sample.

To further improve the performance of light sheet microscopy, 'nondiffracting' light has been introduced[18, 19]. Compared to Gaussian beams, the cross section profile of a nondiffracting beam will not change along its propagation direction, which removes the tradeoff between the thickness of light sheets and the FOV of images in theory[20, 21]. In 2012, Planchon et al. introduced 'nondiffracting' Bessel beams into a light sheet microscope and showed that such beams can create

a light sheet of submicrometer thickness well suited to noninvasive, high-speed, 4D live cell imaging[22]. In 2014, Chen et al. further introduced 'nondiffracting' 2D optical lattices involving linear arrays of coherent Bessel beams for fluorescence excitation[1]. Compared to a single Bessel beam, the linear array of multi-Bessel beams spread the excitation across many foci, greatly reducing the peak intensity at any single focus and in turn reducing the effect of photodamage, making it become the preferred choice for noninvasive imaging.

2.2 Bessel beams and linear arrays of Bessel beams

If the transverse intensity distribution is independent of the propagation distance, this beam will be defined as a nondiffracting beam[21, 23]. Bessel beams are nondiffracting beams whose transverse amplitude is described by the circularly symmetric zero-order Bessel function of the first kind[19, 20]. As shown in **Figure 2.2a**, the transverse profile of an ideal Bessel beam consists of a narrow central peak surrounded by an infinite series of concentric side lobes. The narrow central peak and the propagation-independent transverse profile make an ideal Bessel beam an attractive candidate for light sheet microscopy.

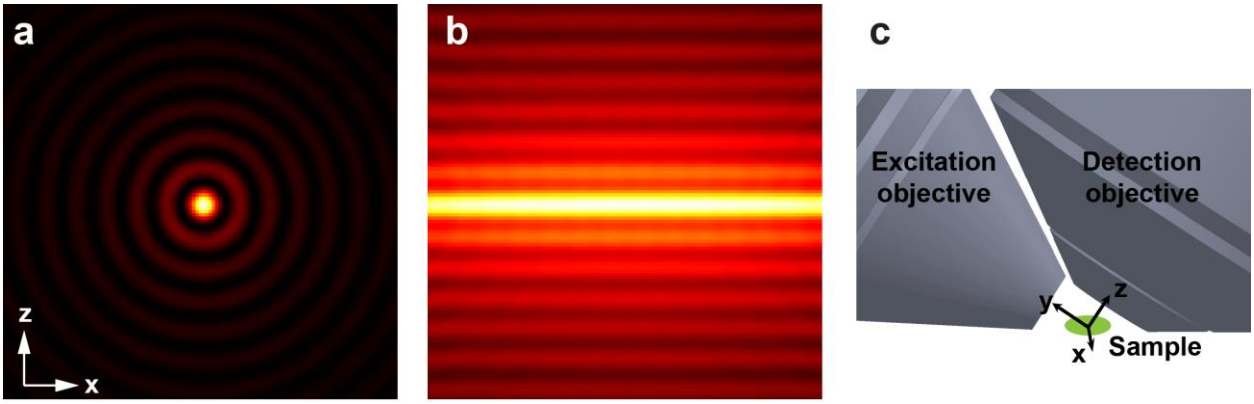

Figure 2.2 Simulated Bessel beam. (a) The xz cross-section of a simulated Bessel beam propagating in y direction. (b) The xz cross-section of a swept Bessel beam. (c) The coordinate system of our home-built LLSM.

However, an ideal Bessel beam is not directly useful for creating thin light sheets. Each ring (including the central peak) in the ideal Bessel beam contains the exact same amount of energy. Thus, sweeping such a beam across the detection focal plane produces unwanted fluorescence outside of the focal plane and in turn weakens optical sectioning ability of light sheet microscopy (**Figure 2.2b**). Furthermore, producing an ideal Bessel beam requires illuminating the rear pupil with an infinitesimally thin ring of light, which is impractical.

In practice, an annulus of finite width is used to produce a finite thin ring of illumination at the rear pupil. The resulting beam is no longer strictly nondiffracting, but will still keep a nearly constant cross section profile over the needed field of view in y, defined by the annulus width. This nonideal Bessel beam is named Bessel-Gauss beam. As its name suggest, a Bessel-Gauss beam has characteristics of each: a suppression of higher order Bessel side lobes due to the Gaussian envelope, and a much longer waist than a conventional Gaussian beam owning to the propagation-independent cross section profile of the Bessel beam.

A previous study[18] has shown the effectiveness of reducing phototoxicity by using an array of seven Bessel-Gauss beams. Motivated by this, Chen et al. have introduced linear arrays of closely spaced Bessel-Gauss beams to spread the excitation across the entire field of view[1]. They have further demonstrated that Bessel-Gauss beam arrays are bounded 2D optical lattices. An ideal 2D optical lattice is a nondiffracting beam which has the cross-sectional symmetry of a 2D Bravias lattice. Like ideal Bessel beams, an ideal 2D optical lattice is also not directly useful for light sheet microscopy because of its unconfined extension in all 3D space. To use 2D optical lattice,

confinement must be applied to its z direction extension limiting the excitation outside of the focal plane, also known as a bounded 2D optical lattice. Owing to its low peak intensity and submicron thickness, this Bessel-Gauss beam array generated light sheet becomes a superior choice for noninvasive imaging.

2.3 Generate desired thin light sheets

In LLSM, the lattice light sheet is generated by a binary ferroelectric spatial light modulator (SLM) that is conjugate to the front focal plane of the excitation objective. An annual mask located in a conjugate plane to the rear pupil of the excitation objective is used to filter the light diffracted by the SLM. This annual mask filters out unwanted zeroth and higher order diffracted light and ensures desired illumination profiles at the specimen. To generate a lattice light sheet with desired properties (e.g., excitation confinement in z, overall axial resolution), we need to find a proper binary pattern for the SLM and theoretically confirm that beams diffracted by this pattern and further filtered by the designed annulus do produce the desired lattice light sheets at the specimens. This theoretical confirmation is done by a Fourier optics based simulation in MATLAB (code was adapted from Chen et al.) [1], and details of the procedures are shown in **Figure 2.3**. Although the periodical intensity profiles of lattice light sheets enable the LLSM to achieve super resolution by structure illumination, multiple images need to be recorded at each z plane, which limits imaging speed. To reduce the motion blur due to bacterial motility, all of our biofilm images are recorded in the dithered mode. In the dithered mode, a galvanometer is used to oscillate the lattice pattern along the x axis at a speed fast enough to compared to the camera exposure time and an amplitude larger than the lattice period, creating a time-averaged uniform light sheet across the xy plane. Thus, only one 2D image needs to be recorded at each z plane.

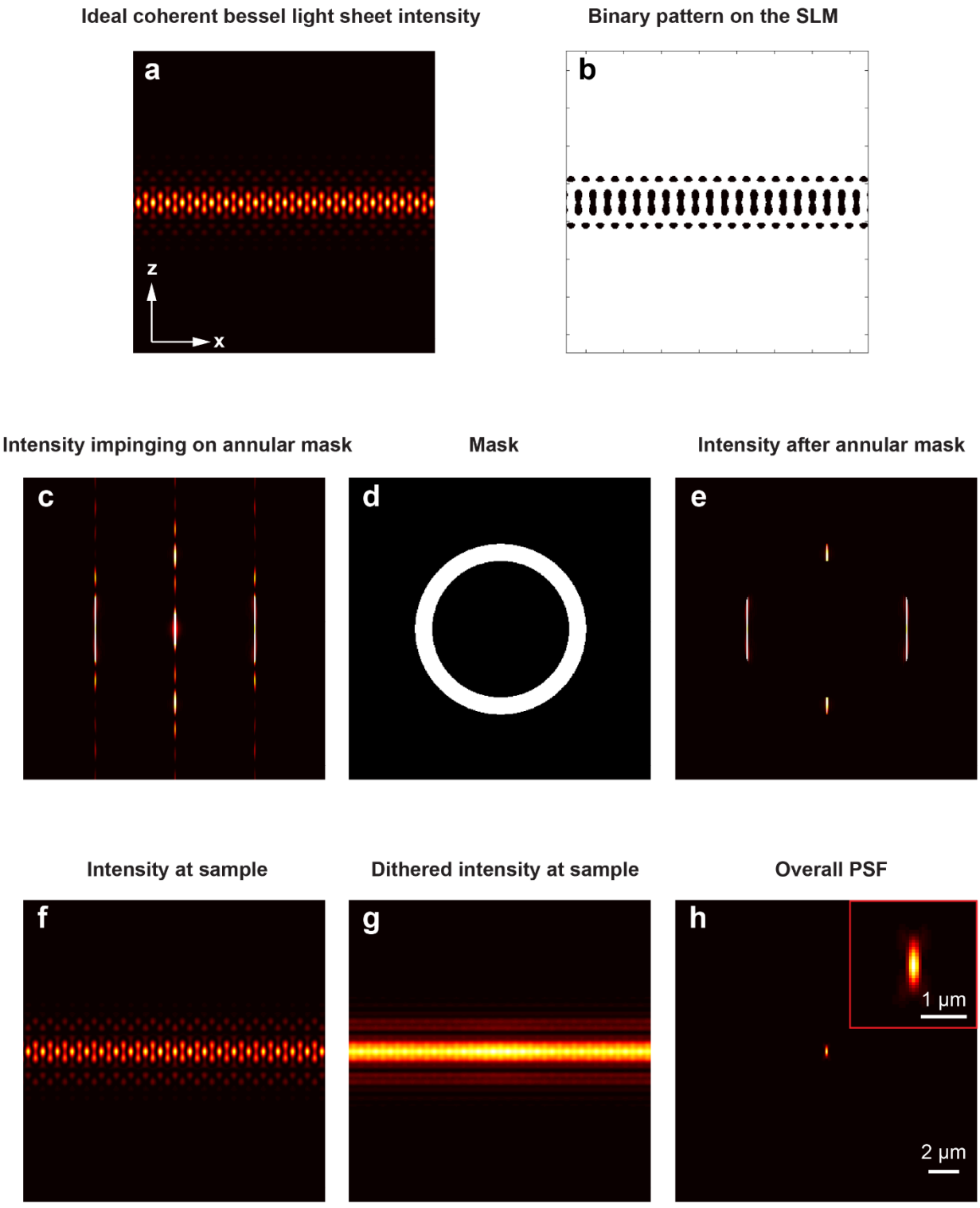

Figure 2.3 Steps in the simulation for the generation of the SLM pattern for a desired lattice light sheet. (a) An ideal coherent Bessel light sheet intensity. (b) SLM pattern obtained by cropping

and binarizing the ideal coherent Bessel light sheet shown in (a). (c) Predicted diffraction pattern on the annular mask, produced by the light that is phase modulated by the SLM. (d) Simulated annulus mask. The inner and outer Numerical Aperture (NA) of the annulus is 0.44 and 0.55 respectively, which matches our experimental set-up. (e) Predicted illumination intensity after the annulus mask. (f) Predicted xz cross-section of the lattice light sheet at the sample. (g) Predicted xz cross-section of the dithered lattice light sheet. (h) Predicted overall PSF of LLSM in the dithered mode. Inset is a higher magnification view.

2.4 Detailed optical path of LLSM

Our home-built lattice light sheet microscope generally follows the original design from the Betzig lab[1] with a key modification in the detection path. The original path only has a 500mm focal length tube lens to provide an overall magnification of 62.5X. Our new design instead consists of a tube lens (250 mm FL/50.8 mm dia, Edmund), providing a 31.25X magnification, and a pair of achromatic relay lenses (80 mm FL/25.4 mm dia Thorlabs AC254-080-A, 160 mm FL/25 mm dia, Edmund 67-331-INK) in a 4f arrangement to obtain a total magnification of 62.5X. Thus, our new emission path provides the same overall magnification as the original one, but adding the 4f system provides more function extension space for the microscope (**Figure 2.4ab**).

2.4.1 Main optical path

The microscope contains four lasers in the excitation pathway: a 405 nm laser (250mW, Coherent OBIS, OBIS 405nm LX), a 488 nm laser (1000 mW, Genesis, MX488-1000 STM), a 560 nm laser (1000 mW, MPB Communications, 2RU-VFL-P-1000-560-B1R), and a 641 nm laser (1000 mW, MPB Communications, 2RU-VFL-P-1000-647-B1R). Lasers are expanded to a $1/e^2$ diameter of 4 mm by two lenses (50 mm FL/25.4 mm dia, Thorlabs, 200 mm FL/25.4 mm dia,

Thorlabs) before passing through an acousto-optic tunable filter (AA Quanta Tech, Optoelectronic AOTF AOTFnC-400.650-TN). The AOTF is used to select the beam wavelengths, control illumination intensities and synchronize with the spatial light modulator (SLM). A flip mirror is placed behind the AOTF, allowing the beam to switch between the main optical path (mirror down) and the epi-illumination path (mirror up). Following the flip mirror in the main optical path, a pair of cylindrical lenses (25 mm FL/12.5 mm dia, Edmund NT68-160 and 200 mm FL/25.4 mm dia, Thorlabs, ACY254-200-A) are positioned to expand the beam in the x direction. The expanded beam uniformly illuminates a strip of the SLM on which the lattice light sheet pattern is displayed. The SLM is composed of 2048 x 1536 ferroelectric-liquid-crystal pixels (Forth Dimension, QXGA-3DM). Each pixel of the SLM can be digitally set to on or off, which together with a polarizing cube beamsplitter (Newport, 10FC16PB.3) and a half-wave plate (Bolder Vision Optik, BVO AHWP3) provide a 0 or π phase shift to the diffracted beam[24]. The diffracted light from the SLM is then focused though a 500 mm focal length achromatic lens (500 mm FL/40 mm dia, Edmund 49-283) onto an annular mask (Photo Sciences Inc). The unwanted zeroth and higher order diffracted light caused by the finite-sized (8.2 μm) pixels of the SLM is physically filtered out by the annular mask. After passing through the mask, the desired beam is demagnified 0.75X through two relay lenses (80 mm FL/12.5 mm dia, Edmund NT47-670, 60 mm FL/12.5 mm dia, Edmund NT47-668) and conjugated to a scanning system composed of two 3 mm galvos (Cambridge Technology, 6215H) and a pair of equal focal length achromatic relay lenses (25 mm FL/12.5 mm dia, Edmund NT47-662) in a 4f arrangement. As each galvo is positioned conjugate to the back pupil of the excitation objective, this system provides scanning along the x and z axis at the sample. After passing through the scanning system, the annular mask filtered beam pattern is re-magnified 3.2X through relay lenses (125 mm FL/25 mm dia, Edmund NT49-361, 400 mm

FL/25 mm dia, Edmund 47-650) and conjugated to the back pupil of a custom water immersion excitation objective (Special Optics, 0.65 NA, 3.74 mm WD). Overall, the SLM and the front focal plane of the detection objective form one set of conjugate planes in the illumination path, and the annular mask, scanning galvos, and the back pupil form another set.

After the lattice light sheet is projected onto the front focal plane of the excitation objective, the excited fluorescence of the sample is collected by an orthogonally mounted detection objective (Nikon, CFI Apo LWD 25XW, 1.1 NA, 2 mm WD). The detection objective is positioned on a piezo stage (Physik Instrumente, P-621.1CD), which keeps the focal plane of the detection objective coincident with the lattice light sheet illumination and provides z-scan ability to the detection objective. The fluorescence signal is then imaged through an emission filter onto a sCMOS camera (Hamamatsu, Orca Flash 4.0 v2 sCMOS) by our custom emission path. Two inspection cameras (Imaging Source, DMK 33UP1300), located in planes conjugate to either the back pupil of the excitation objective or the front focal plane of the excitation objective, aid in aligning and verifying the lattice pattern.

2.4.2 Epi-illumination path

As the flip mirror behind the AOTF is flipped up, the beam will pass through the epi illumination path. The beam is expanded 3.75X with two achromatic lenses (20 mm FL/12.5 mm diameter, Edmund 47-661, 75 mm FL/12.5 mm diameter Edmund 47-669). It then passes through a 200 mm focal length achromatic lens (200 mm FL/25 mm, Edmund 49-364). Following this lens, a 90:10 (Reflection : Transmission) non-polarizing beamsplitter cube (Thorlabs, BS028) is positioned. The beamsplitter transmits 10% of incoming light, which is then projected onto the sample by a water immersion objective (Olympus LUMPLFLN 40XW, 0.8 NA, 4.5 mm WD). This objective shares the same focal point with the excitation objective and the detection objective

in the main optical path, thus providing epi-illumination for the sample. Besides, an emission path composed of a 100mm tube lens (100mm FL/25mm diameter, Edmund NT47-641), an emission filter, and a CMOS camera (Imaging Source, DMK 33UP1300) is set at the reflection path of the 90:10 (R:T) beamsplitter, which provides extra wide field imaging ability.

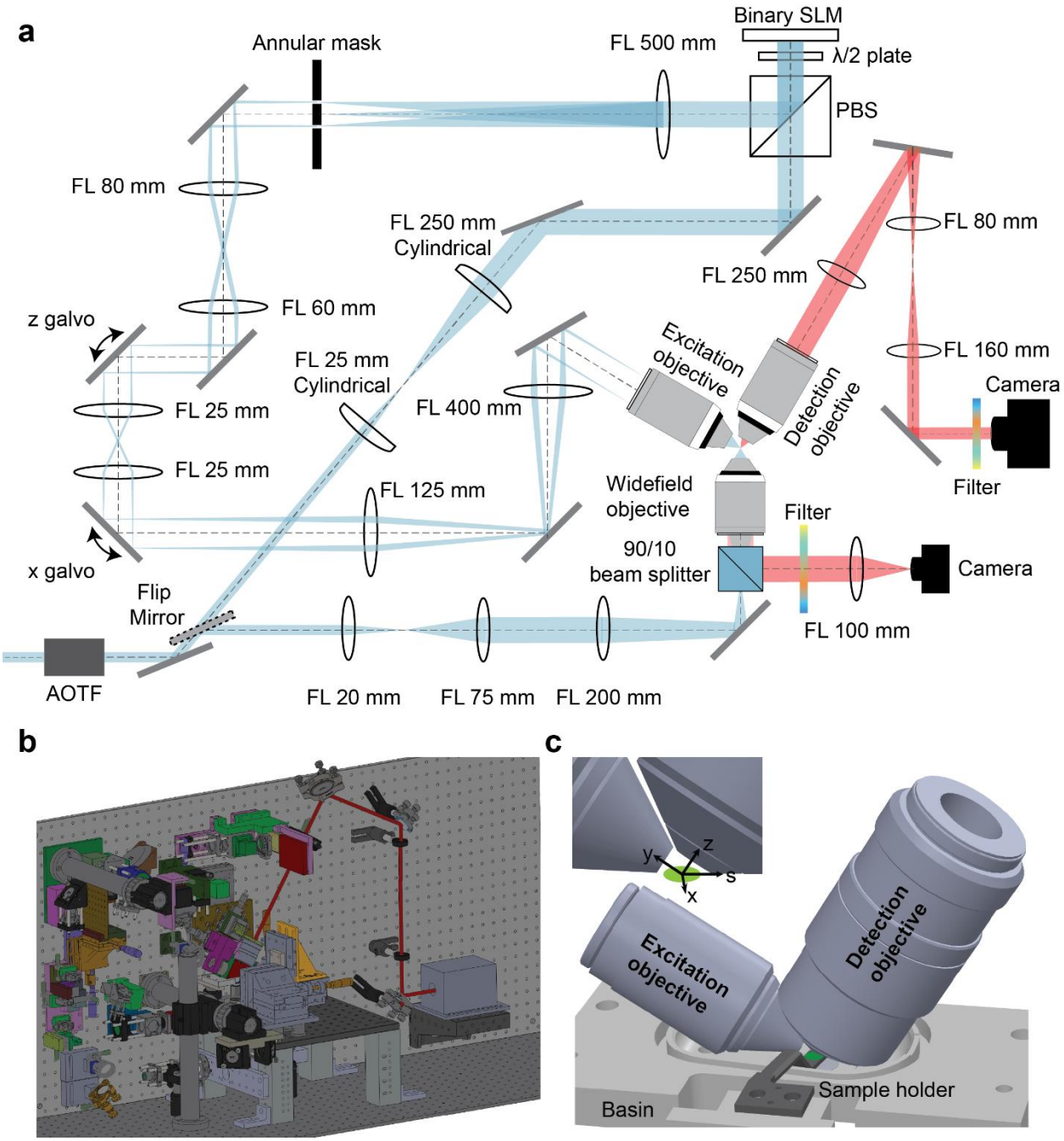

Figure 2.4 Schematic of our home-built lattice light sheet microscope. (a) Optical path of the LLSM, Focal length was simplified as FL, PBS represents polarization beam splitter. (b) 3D model (SolidWorks 2020, Dassault Systèmes) of the LLSM, the red line indicates the emission path. (c) The core of our microscope, with orthogonal excitation and detection objectives dipped in a media-filled bath. Inset is a higher magnification view, showing the excitation and detection objectives, which share a same focal point within a specimen that is mounted onto a cover glass within the media. The x, y, and z directions are indicated. The s-axis defines the direction the specimen moves from image plane to image plane.

2.5 Recording 3D stacks and raw data processing

For 3D stacks recording, a specimen mounted onto a coverslip was moved through the dithered light sheet using a piezo nano-positioning stage (Mad City Labs, NanoOP100HS), shown in **Figure 2.4c**. The fluorescence signal thereby generated was recorded as a series of 2D slices and then combined into a 3D stack. However, unlike conventional microscopy, these LLSM obtained 2D slices cannot be directly rebuilt into 3D stacks. As shown in **Figure 2.5a,** the fact that the detection objective lens of the LLSM is tilted at an angle with respect to the axis of stage movement results in an unconventional geometry for the acquired image stack, i.e., an offset between each slice. Thus, a conventional 3D stack rendering will result in a skewed result, as shown in **Figure 2.5b**. To remove this artifact, a deskewing process is employed, i.e., computationally adding offset back, as shown in **Figure 2.5c**. If preferred, background subtraction and Richardson-Lucy based deconvolution can be further applied to improve resolution and contrast of the images[1, 10, 25].

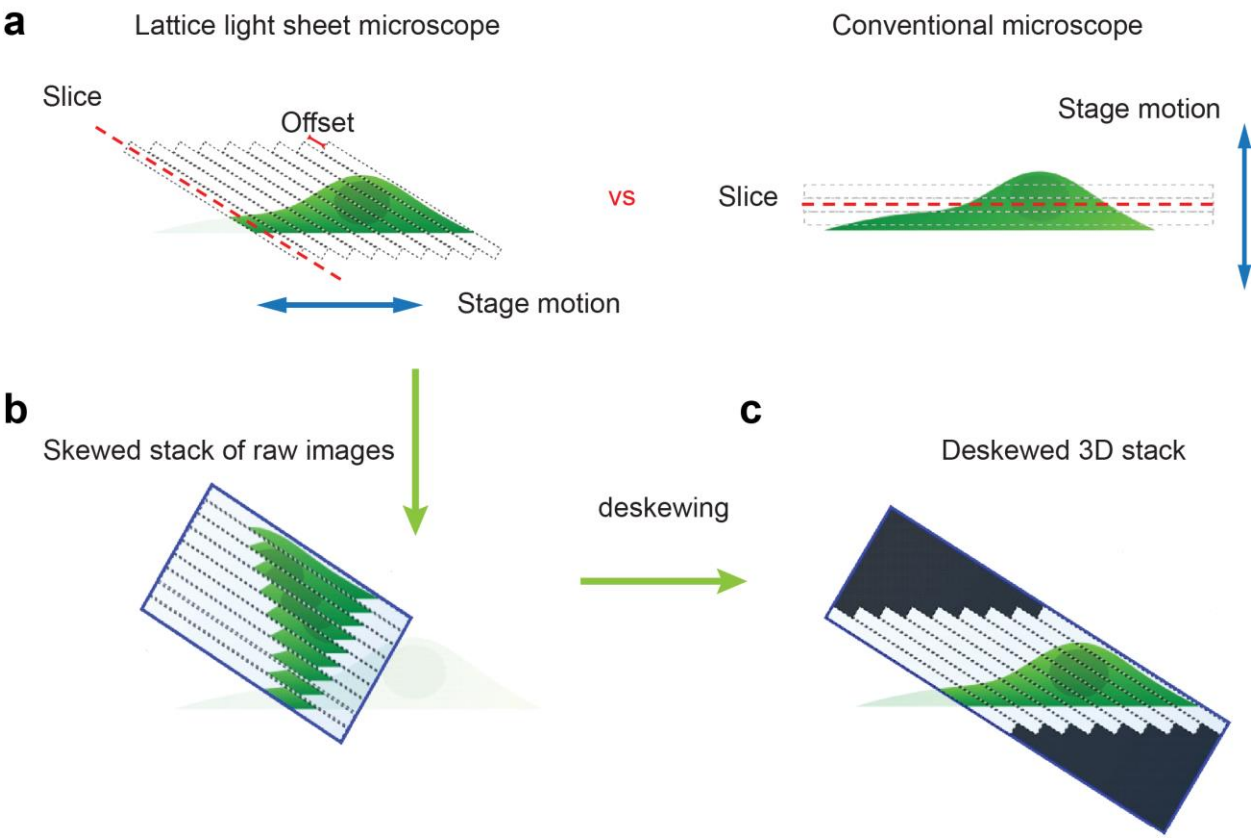

Figure 2.5 Schematic of raw data processing for the LLSM. (a) Geometry of the acquired image stacks, LLSM vs conventional microscope. (d) A skewed stack of the LLSM raw data. (c) A deskewing-processed LLSM stack.

References

1. Chen, B.-C.; Legant, W. R.; Wang, K., et al., Lattice light-sheet microscopy: imaging molecules to embryos at high spatiotemporal resolution. *Science* **2014,** *346* (6208).

2. Qin, B.; Fei, C.; Bridges, A. A., et al., Cell position fates and collective fountain flow in bacterial biofilms revealed by light-sheet microscopy. *Science* **2020,** *369* (6499), 71-77.

3. Buchholz, T.-O.; Krull, A.; Shahidi, R., et al., Content-aware image restoration for electron microscopy. *Methods in cell biology* **2019,** *152*, 277-289.

4. Laissue, P. P.; Alghamdi, R. A.; Tomancak, P., et al., Assessing phototoxicity in live fluorescence imaging. *Nature methods* **2017,** *14* (7), 657-661.

5. Parthasarathy, R., Monitoring microbial communities using light sheet fluorescence microscopy. *Current opinion in microbiology* **2018,** *43*, 31-37.

6. Pamp, S. J.; Sternberg, C.; Tolker‐Nielsen, T., Insight into the microbial multicellular lifestyle via flow‐cell technology and confocal microscopy. *Cytometry Part A: The Journal of the International Society for Analytical Cytology* **2009,** *75* (2), 90-103.

7. Stelzer, E. H., Light-sheet fluorescence microscopy for quantitative biology. *Nature methods* **2015,** *12* (1), 23-26.

8. Jonkman, J.; Brown, C. M.; Wright, G. D., et al., Tutorial: guidance for quantitative confocal microscopy. *Nature protocols* **2020,** *15* (5), 1585-1611.

9. Jemielita, M.; Taormina, M. J.; DeLaurier, A., et al., Comparing phototoxicity during the development of a zebrafish craniofacial bone using confocal and light sheet fluorescence microscopy techniques. *Journal of biophotonics* **2013,** *6* (11‐12), 920-928.

10. Gao, R.; Asano, S. M.; Upadhyayula, S., et al., Cortical column and whole-brain imaging with molecular contrast and nanoscale resolution. *Science* **2019,** *363* (6424).

11. Barner, L. A.; Glaser, A. K.; Huang, H., et al., Multi-resolution open-top light-sheet microscopy to enable efficient 3D pathology workflows. *Biomedical Optics Express* **2020,** *11* (11), 6605-6619.

12. Keller, P. J.; Schmidt, A. D.; Wittbrodt, J., et al., Reconstruction of zebrafish early embryonic development by scanned light sheet microscopy. *science* **2008,** *322* (5904), 1065-1069.

13. Voleti, V.; Patel, K. B.; Li, W., et al., Real-time volumetric microscopy of in vivo dynamics and large-scale samples with SCAPE 2.0. *Nature methods* **2019,** *16* (10), 1054-1062.

14. Olarte, O. E.; Andilla, J.; Gualda, E. J., et al., Light-sheet microscopy: a tutorial. *Advances in Optics and Photonics* **2018,** *10* (1), 111-179.

15. Power, R. M.; Huisken, J., A guide to light-sheet fluorescence microscopy for multiscale imaging. *Nature methods* **2017,** *14* (4), 360-373.

16. Remacha, E.; Friedrich, L.; Vermot, J., et al., How to define and optimize axial resolution in light-sheet microscopy: a simulation-based approach. *Biomedical optics express* **2020,** *11* (1), 8-26.

17. Yang, B.; Chen, X.; Wang, Y., et al., Epi-illumination SPIM for volumetric imaging with high spatial-temporal resolution. *Nature methods* **2019,** *16* (6), 501-504.

18. Gao, L.; Shao, L.; Higgins, C. D., et al., Noninvasive imaging beyond the diffraction limit of 3D dynamics in thickly fluorescent specimens. *Cell* **2012,** *151* (6), 1370-1385.

19. Liu, T.-L.; Upadhyayula, S.; Milkie, D. E., et al., Observing the cell in its native state: Imaging subcellular dynamics in multicellular organisms. *Science* **2018,** *360* (6386).

20. Lin, Y.; Seka, W.; Eberly, J., et al., Experimental investigation of Bessel beam characteristics. *Applied optics* **1992,** *31* (15), 2708-2713.

21. Bouchal, Z., Nondiffracting optical beams: physical properties, experiments, and applications. *Czechoslovak journal of physics* **2003,** *53* (7), 537-578.

22. Planchon, T. A.; Gao, L.; Milkie, D. E., et al., Rapid three-dimensional isotropic imaging of living cells using Bessel beam plane illumination. *Nature methods* **2011,** *8* (5), 417-423.

23. Durnin, J.; Miceli, J.; Eberly, J. H., Comparison of Bessel and Gaussian beams. *Optics letters* **1988,** *13* (2), 79-80.

24. Kner, P.; Chhun, B. B.; Griffis, E. R., et al., Super-resolution video microscopy of live cells by structured illumination. *Nature methods* **2009,** *6* (5), 339-342.

25. Laasmaa, M.; Vendelin, M.; Peterson, P., Application of regularized Richardson–Lucy algorithm for deconvolution of confocal microscopy images. *Journal of microscopy* **2011,** *243* (2), 124-140.

Chapter 3 Optically Accessible Microfluidic Flow Channels for Non-Invasive High-Resolution Biofilm Imaging using Lattice Light Sheet Microscopy

This chapter is adapted from Zhang, J., Zhang, M., et al. *J. Phys. Chem. B.* **2021,** 125 (44), 12187-12196[1].

3.1 Introduction

Bacterial biofilms are microbial communities that grow on various surfaces and encase themselves in a self-produced extracellular matrix (ECM) containing proteins, DNA, and polysaccharides[2-4]. Owing to their communal and cooperative behaviors, biofilm-dwelling cells have shown emergent capabilities beyond those of the planktonic phase cells[4-6]. Consequently, biofilms are orders of magnitude more tolerant towards external threats, including antibiotic treatments and immune system clearance[5, 7-9]. Because biofilms are a major component of microbial life, it is vitally important to understand how population-level capabilities emerge from the coordination of individual cell behaviors[10]. To gain this understanding, non-invasive imaging techniques that are capable of resolving and tracking individual cells in 3D biofilms are required.

Fluorescence microscopy is one of the best tools to reveal both the spatial and temporal contexts that affect cellular behaviors in a biofilm[11-13]. However, conventional widefield and confocal techniques illuminate the entire thickness of the specimen, even though useful information is only obtained from a single slice in the specimen that is coincident with the microscope's focal plane[14, 15]. Repeated illumination of the entire specimen results in increased

phototoxicity and photodamage, which results in a disadvantageous tradeoff between temporal resolution and total imaging time[16]. In contrast, light sheet fluorescence microscopy approaches, while achieving similar resolution to confocal microscopy, are more photon efficient, because they utilize coincident excitation and detection planes, so that out-of-focus specimen regions are not illumilated[17-19]. Among light sheet-based fluorescence microscopies, lattice light sheet microscopy (LLSM) has proven especially powerful for noninvasive 3D live imaging of embryos and organelles at high spatial and temporal resolution[20-23]. Dual inverted selective plane illumination microscopy (diSPIM)[24] is another high-resolution light sheet-based fluorescence microscopy modality that has recently been applied to biofilm imaging[13]. With the ability to acquire images from two orthogonal views (dual view), diSPIM can provide isotropic resolution. However, it is important to note that isotropic resolution comes at the cost of twice the number of image exposures. If the goal is to reduce the amount of photobleaching and phototoxicity, the number of image frames should be kept to a minimum, if at all possible.

Bacterial biofilms pose an additional challenge for high numerical aperture LLSM, diSPIM, and similar dual-objective light sheet implementations. The high numerical aperture water immersion objective lenses require the sample to be in close proximity to the objective lenses. In the original LLSM implementation[23], the sample is therefore not physically separated from the objective lenses, but is simply mounted on a spoon-like sample holder and then immersed into an aqueous growth medium for imaging. This is in contrast to conventional inverted fluorescence microscopy setups, where a glass coverslip provides a physical barrier between the microscope and the specimen[23, 25]. The open-on-top sample mounting approach allows for direct optical access, but it is not suitable for long-term biofilm imaging. First, biofilms eventually grow on the objective lenses themselves and thereby attenuate the excitation and emission light intensities leading to a

loss of signal. Second, colonized microscope components could expose microscope users to potentially harmful bacterial pathogens[26, 27]. Third, an open sample basin makes any biological sample vulnerable to airborne biological and chemical contaminants, which could affect a living specimens in unpredictable ways[28]. Containing living biological specimen in an enclosed environment, separate from the microscope components, is necessary to ensure well-controlled experimental conditions and the safety of laboratory personnel who work with pathogenic specimens.

Microfluidic channels, made from biocompatible polydimethylsiloxane (PDMS) adhered to a glass coverslip, have been widely used for live-cell biofilm imaging on conventional inverted microscopes[29, 30]. These studies have demonstrated that shear forces due to fluid flow is a critical factor influencing the growth of biofilms; in some cases, fluid flow is arguably a necessary factor to image biofilms in physiologically relevant environments. Hartmann *et al.* have recorded the growth dynamics of *Vibrio cholerae* using a spinning disk confocal microscope using PDMS-based microfluidic flow systems[12]. Thomen *et al.* studied the effects of hydrodynamics on growing biofilms by utilizing PDMS flow channels of various sizes with bright-field and epifluorescent microscopes[31]. Coyte *et al.* studied the hydrodynamic interactions between competing biofilms through a Y-shaped microfluidic system with bright-field and epifluorescent microscopes[32]. Due to the widespread use of single-objective inverted microscope implementations, recent developments have also enabled high-numerical aperture light sheet imaging using only a single objective lens[33-35]. These implementations share many of the critical benefits of LLSM (low phototoxicity/photodamage and high spatial and temporal resolution) while also enabling high resolution bottom-to-top imaging of cells in a biofilm. However, the necessity of the biofilm

growth substrate to be optically transparent is an inherent drawback of such inverted microscope imaging geometries.

Integrating microfluidic technology with LLSM is challenging for two reasons. First, the space between the two LLSM objective lenses is very small, which necessitates a small microfluidic device footprint. Typical PDMS-based microfluidic devices are tens of milimeters in size[29, 36, 37] and therefore too large for LLSM. Second, the refractive index of PDMS does not match the refractive index of the aqueous growth media[38], which would result in unacceptable optical aberrations[25, 39]. Due to these challenges, LLSM-integrated microfluidic channels are rare. Only very recently, Fan *et.al* reported an LLSM-integrated channel sealed with Sarstedt Lumox® film, a biocompatible material that has a refractive index similar to water[40]. However, repeated high-resolution imaging of living cells over time was not possible, because the numerical aperture (NA) of that imaging system was 0.8 (the imaging system used here has an NA of 1.1) and the channel was not mounted on a motorized sample stage which would enable imaging of large specimen volumes by stage scanning. Instead, 3D imaging was achieved by flowing unattached cells through the light sheet. To imagesessile cell populations repeatedly over time at high resolution, a more versatile imaging system and flow channel integration is needed.

Here, we report a flow channel design that is fully compatible with high-resolution LLSM and demonstrate its application in extended time live-cell biofilm imaging. A 3D-printed folded channel architecture ensures full compatibility with the original and most widely adapted LLSM implementation. A refractive index matched polymer film was used to seal the observation window on the top channel. We found that precise refractive index matching (1.333) substantially reduces optical aberrations thus enabling close to optimal imaging conditions. Using this channel, we obtained high quality time-lapse images of growing biofilms over several days with the possibility

to extend the imaging duration even further. Single-cell resolution was maintained at all time points. A completely enclosed flow channel, as describe here, can benefit any water-dipping dual-objective light sheet implementation, including diSPIM. Although diSPIM imaging of *Vibro cholera* biofilms could be performed for 16 hours with an open top chamber containg growth medium[13], an enclosed channel could further enhance the versatility of diSPIM for biofilm research, specifically, by providing better control over physical and chemical growth conditions and by preventing airborne contaminants from reaching the biofilm. We anticiapte that the integration of microfluidic technologies with non-invasive, high-resolution imaging technologies and computational image analysis[41, 42] will enable studies on how individual cells' behavioral phenotypes, as well as chemical and mechanical driving forces shape bacterial communities and determine their emergent functional capabilities.

3.2 Materials and Methods

3.2.1 Flow channel design and fabrication

The flow channel was designed using SolidWorks 2020 (Dassault Systèmes SOLIDWORKS Corp) (**Figure 3.1**). The main chamber is 12.10 mm long and 4.40 mm wide. To physically isolate the inner chamber space from the outside environment, a detection window with a length of 5.00 mm is draped over the top of the channel to allow light transmission into the entire collection solid angle of the detection objective. A platform holding an arbitrary substrate for biofilm growth is positioned in the middle of the main chamber. A folded channel architecture was chosen to minimize channel/sample drift and to ensure easy routing of plastic tubing away from optical and optomechanical components of the LLSM. These measures also made it easier to mount and then translate the channel on automated micro- and nano-positioning stages. To reduce

the impact of the refractive index boundaries in the excitation and emission light paths, a 50 μm thick film of MY133-V2000 polymer (My Polymers, Israel) was used to seal the detection window. The refractive index of MY133-V2000 (n = 1.333), which is very close to the refractive index of the media used in our experiments.

Channels were fabricated using Clear Resin V4 in a low force stereolithography Form 3B - 3D printer (Form Labs). After printing, the channels were washed with isopropyl alcohol using the Form Wash instrument (Form Labs) for 10 minutes to remove uncured resin. Then, the channels were removed from the supports and rinsed again in isopropyl alcohol for another 10 minutes. After washing, the channels were dried for 1 hour at room temperature to allow the isopropyl alcohol to evaporate. Finally, the channels were cured by UV light using the Form Cure instrument (Form Labs) for 15 minutes at 35 °C.

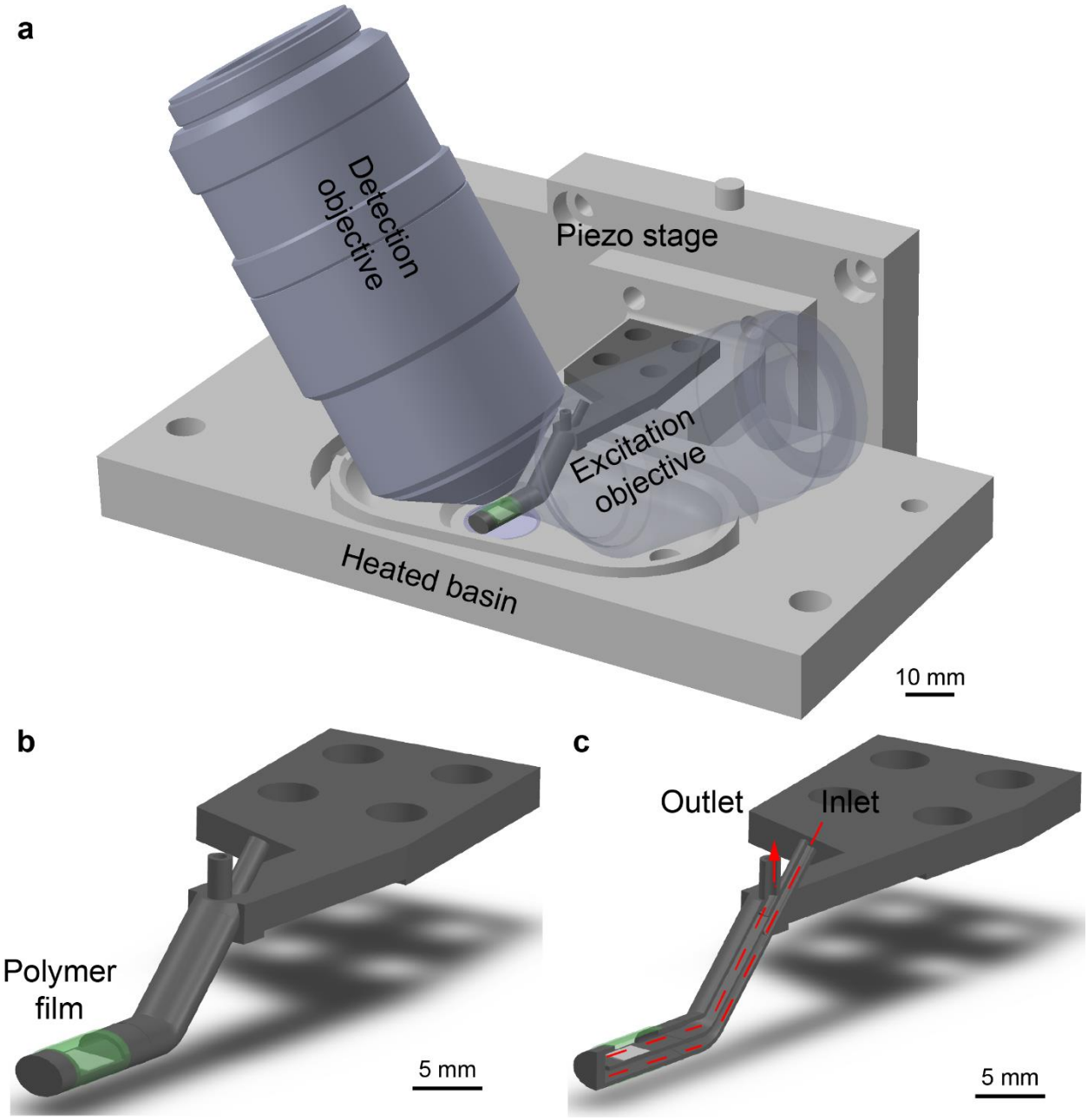

Figure 3.1 Schematic of the experimental setup. (a) Sample area of the custom-built lattice light-sheet microscope. (b) 3D model of 3D printed microfluidic channel. (c) Cross-section of the microfluidic channel, red arrows indicate the flow direction.

3.2.2 Refractive index-matched polymer film fabrication

To create a ~50 µm thick film of MY133-V2000 polymer, we cut a 6 x 6 cm^2 square opening into a 50 µm Teflon film (FEP Teflon, DuPont). The Teflon film was then put onto a flat glass plate (McMaster-Carr, 8476K62) and ~200 µL MY133-V2000 polymer was deposited into the opening. A second flat glass plate was then put on the top of the Teflon film opening and ~5 kg pressure was applied to spread the polymer within (**Figure 3.2a**). The two glass plates were then clamped together using binder clips and the liquid polymer was cured under ultraviolet (UV) illumination (~28 mw/cm2) for two hours using a UV/ozone cleaning instrument (Novascan) (**Figure 3.2b**). The UV curing process resulted in a MY133-V2000 film of ~ 50 µm thickness.

3.2.3 Flow channel assembly

For channel assembly, a piece of film, slightly larger than the detection window, was cut using a razor blade (**Figure 3.2c**). The film piece was sterilized by immersing it into 70% ethanol and allowed to dry out at room temperature. The film piece was then glued onto the channel using LOCA-133 adhesive (My Polymers, Israel) to make an optical transparent, hermetically sealed window (**Figure 3.2d**).

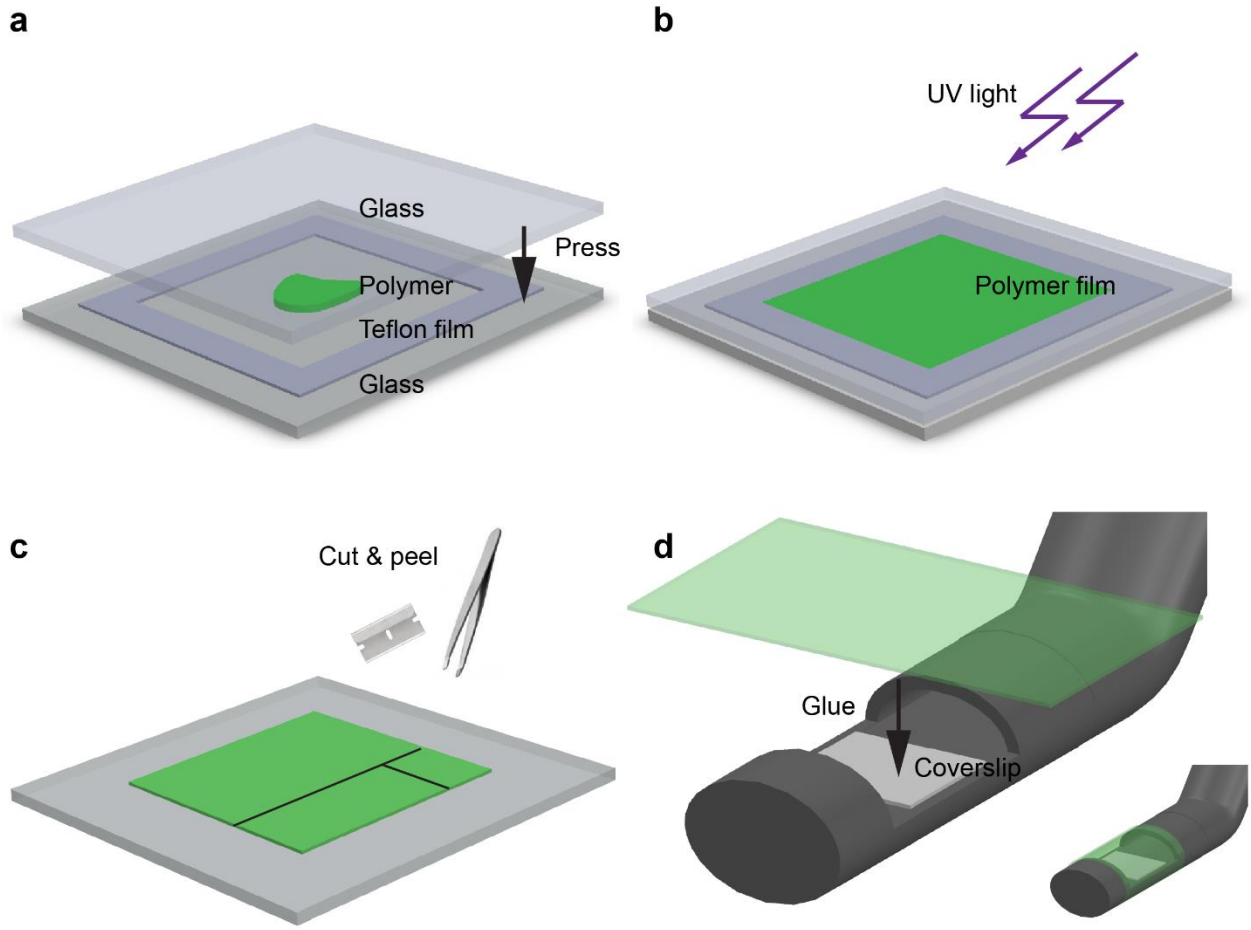

Figure 3.2 Fabrication of the MY133-V2000 polymer film. (a and b) suitable uniform film thickness is achieved by using a Teflon film as a spacer between two glass plates that are pressed together. The liquid polymer is then cured using UV light. (c and d) The cured polymer film is cut into proper sizes using a razor blade and glued onto the 3D-printed channel. The fully assembled channel is hermetically sealed and supports biofilms growth within fluid flow.

3.2.4 Flow channel operation

Kanamycin resistant *S. oneidensis* MR-1, constitutively expressing the green fluorescence protein (GFP), were cultured at 30 °C overnight in LB medium with 50 μg/ml Kanamycin. Overnight cultures were diluted 100 times into the same culture medium, grown to an optical

density at 600 nm (OD_{600}) of 0.4 – 1.0, and then diluted to OD_{600} = 0.05 by M9 medium with 0.05% (W/V) casamino acids before channel inoculation. For the results reported in this paper, a 3 mm square coverslip coated by poly-l-lysine was set on the bottom of the upper channel. The channel was then sterilized using 70% ethanol and rinsed with ddH2O (double distilled water). The channel was then inoculated with live bacterial cell cultures using a syringe. After inoculation, the channel was mounted on a piezo nanopositioning stage (Mad City Labs, NanoOP100HS) and immersed in the basin medium (water or sucrose solution to match the refractive index of the growth media). The channel inlet port was connected to a syringe pump (Harvard Apparatus, Model 22) and the channel outlet port was connected to a waste container using PVC tubing. Before the medium flowing through the channel was initiated, cells were given an hour to attach to the poly-l-lysine coated coverslip. Then, the flow rate was ramped up to 0.5 ml/h for 20 minutes to flush away non-adherent cells. Next, the flow rate was reduced to 0.03 ml/h for the duration of imaging.

GFP fluorescence was excited using 488 nm light sheet excitation. Biofilms were imaged every 30 minutes. At each time point, a 3D image stack containing 301 2D slices was recorded using a 235 nm step size between slices. Each slice was acquired with a short 10 ms exposure time to reduce motion blur from loosely attached and therefore wiggling cells.

3.2.5 Lattice light sheet evaluation

The polymer film that confines the live cell specimens in the flow channel introduces refractive index boundaries in both the optical excitation and emission paths (**Figure 3.3**). To reduce the optical aberrations that may result because of these refractive index boundaries, the objective lenses are immersed in a sucrose solution that has the same refractive index as the medium in the channel (RI = 1.3350, M9 medium in this experiment). The refractive index of the

polymer film itself is 1.3333. Differences between the refractive index of the immersion medium, the polymer film, and the growth medium will lead to refraction of the excitation and emission light according to Snell's law. A previous study has computationally shown that precise refractive index matching is crucial for producing a high quality lattice light sheet[40]. We therefore evaluated the importance of refractive index matching experimentally using 488 nm laser excitable fluorescent beads (200 nm FluoSpheres®, Thermo Fisher) as calibration samples. Beads were coated on a 3 by 3 mm coverslip (Deckglaser). The coverslip was positioned into the channel below the observation window (see **Figure 3.2d**). A hexagonal lattice light sheet and a square lattice light sheet were used for illumination separately. By visualizing the intensity change of a bead during a scan, a cross section of the lattice pattern at the focal plane is generated, as shown previously[23]. An open window (i.e. no polymer foil) was used as a positive control for perfect refractive index matching. As test cases we used two different polymer foils: a 50 µm thick fluorinated ethylene propylene Teflon (FEP Teflon, DuPont) film and MY133-V2000 (My Polymers, Israel). FEP Teflon is a commonly used material in light sheet microscopy application, because its refractive index is close to that of water (1.3440 vs. 1.3327).

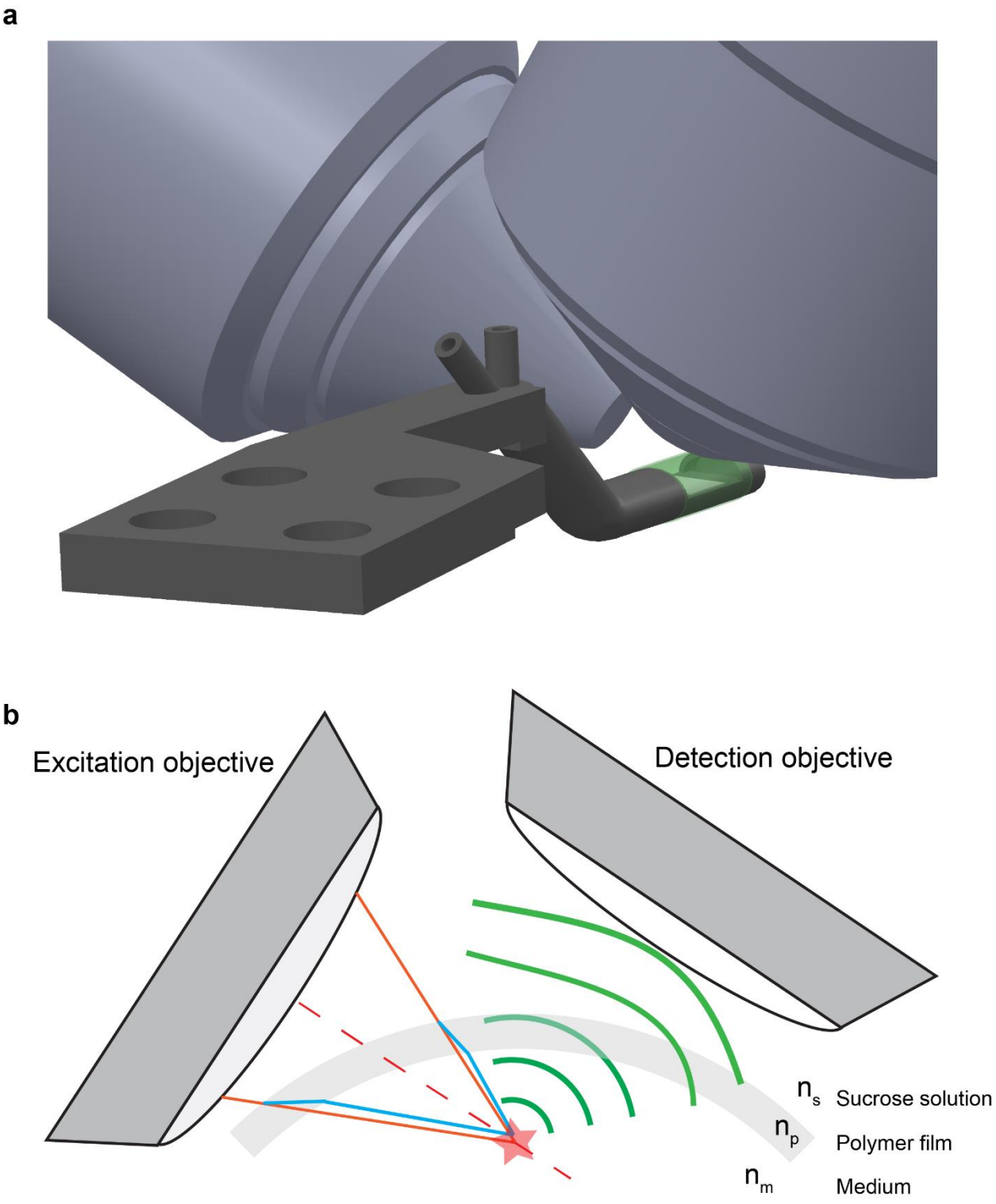

Figure 3.3 Schematic for lattice light sheet imaging. (a) Arrangement of two objectives and the microfluidic channel. (b) Schematic for excitation and emission light paths for the lattice light

sheet imaging. Notice the refractive index difference between the polymer film and medium lead to light distortion.

3.2.6 Resolution evaluation

In a second set of measurements, we evaluated the size of the microscope's point-spread function (PSF) for different polymer foils. We evaluated the full width at half maximum (FWHM) of the PSFs of 200 nm fluorescence beads (FluoSpheres®, Thermo Fisher). We first scanned the lattice light sheet and the detection objective simultaneously along the z axis to obtain a 3D volume of a fluorescence bead. Then, an XZ image of the PSF was generated by the maximum intensity projection. This XZ projection image was then fitted by a 2D gaussian function, $f(x,z) = Aexp(-(\frac{(x-x_0)^2}{2\sigma_X^2} + \frac{(z-z)^2}{2\sigma_z^2}))$, where σ_x is the standard deviation along the x axis and σ_z is the standard deviation along the z axis. The FWHM was then calculated using $FWHM_{z/x} = 2\sqrt{2\,ln\,2}\,\sigma_{z/x}$.

3.2.7 Biofilm images evaluation

The quality of experimental biofilm images were evaluated by estimating the resolution and signal-to-background ratio. For resolution estimation, we used a previously reported decorrelation analysis[43]. To estimate the signal-to-background ratios (SBRs), we manually determined the intensities of five “signal” and five “background” regions in the images. The SBRs were computed as the mean signal intensity divided by the mean background intensity.

3.2.8 Volumetric image stitching and display

To image 3D biofilms that are larger than the field-of-view of the LLSM, a tiled scan was applied. Volumetric tiles were aligned through pairwise phase correlation and global optimization using BigSticher[44]. To minimize boundary artifacts, less weight (a cosine-shaped fade-out) was placed on border voxels of the input stacks. Final 3D views were rendered in ChimeraX[45].

3.3 Results and discussion

3.3.1 Microscope performance when imaging through polymer films

The change from an open sample platform to an enclosed channel introduces four additional refractive index boundaries; two in the excitation path and two in the emission path (**Figure 3.3**). To determine the influence of these additional refractive boundaries, we recorded the xz cross section of the lattice light sheet pattern. The light sheet cross sections show minimal distortions from an ideal lattice pattern when the channel window is not covered by a polymer foil (**Figure 3.4a**). When the window is covered with a MY133-V2000 polymer film, slight distortions begin to manifest, and when the window is covered by FEP Teflon, more severe blurring is evident (**Figure 3.4bc**). The refractive index difference between FEP Teflon and water is only 0.0113, indicating that better refractive index matching is required. The refractive index difference between MY133-V2000 and water is 0.0006. Indeed, this polymer material provides a lattice pattern that more closely resembles that obtained without a polymer window. These results show that refractive index matching is a crucial parameter for optimizing imaging performance in LLSM.

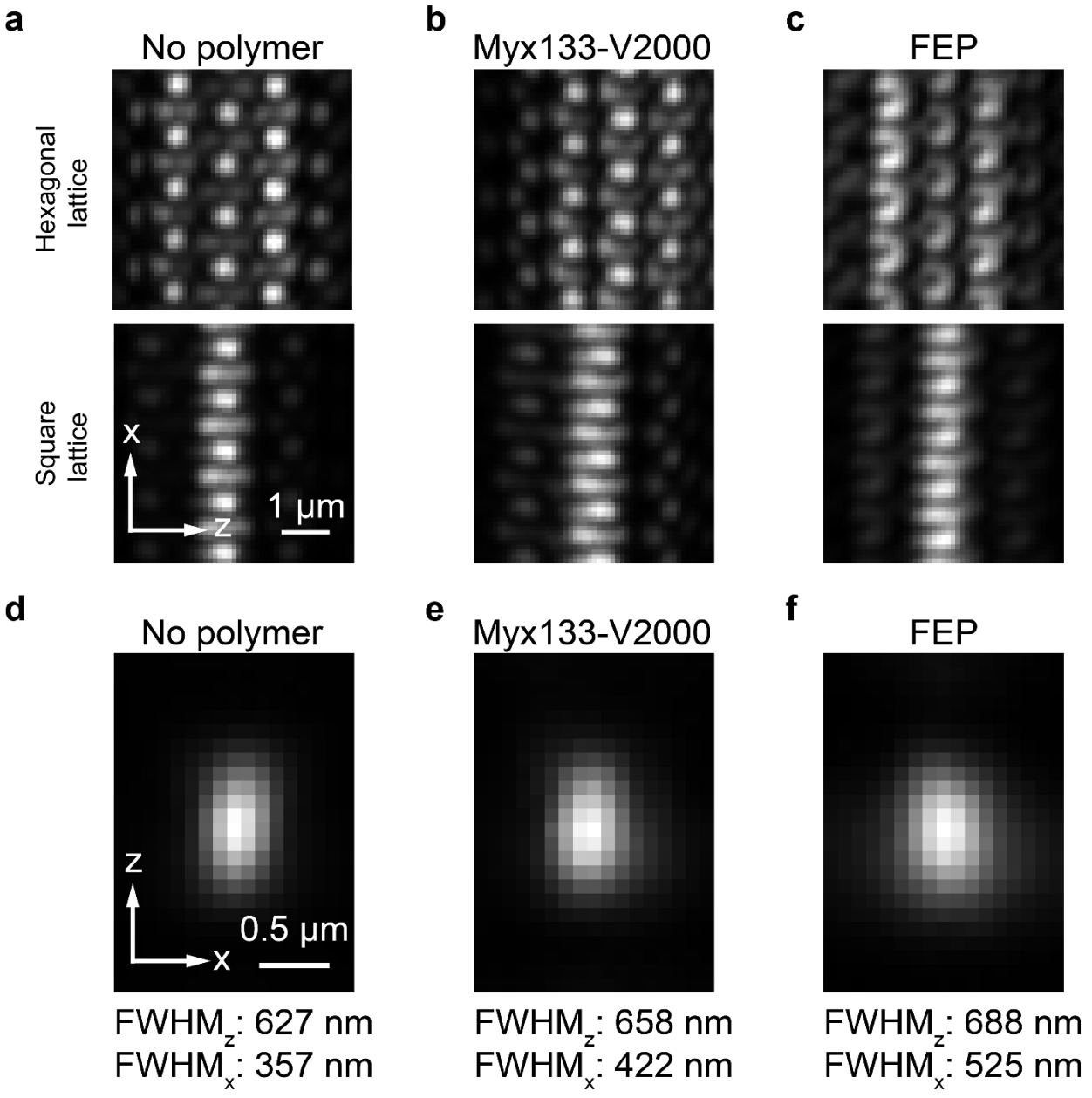

Figure 3.4 Evaluation effect of refractive index mismatch. Cross-sectional profiles of the lattice light sheet at the focal plane when imaged through different window materials: (a) no polymer, (b) MY133-V2000 polymer, (c) FEP. Cross-sectional profiles of 200 nm fluorescent beads when imaged through different window materials: (d) no polymer, (e) MY133-V2000 polymer, (f) FEP.

The superiority of the MY133-V2000 polymer was further confirmed by measuring the lateral and longitudinal FWHM of 200 nm fluorescence bead images. These images represent the size of the microscopes' point spread function (PSF) convolved with the size of the 200 nm diameter fluorescence beads. As expected, the smallest FWHM values were obtained when no polymer is present in the light path (**Figure 3.4d**). When the channel window is covered with MY133-V2000 polymer, the FWHM increases slightly (**Figure 3.4e**) and when the channel window is covered with FEP Teflon, the largest FWHM is obtained for the conditions tested here (**Figure 3.4f**). Since the same type of beads were imaged under all conditions, the increase in the FWHM of the bead images can be attributed to an increase in the microscope's PSF. These results show again that better refractive index matching results in less severe optical aberrations and thus in smaller PSF sizes, which will ultimately result in crisper, higher resolution images. For the materials tested here, MY133-V2000 polymer films produced a smaller PSF than FEP films. Therefore, we used the MY133-V2000 polymer for channel construction in all subsequent experiments.

3.3.2 Live-cell LLSM imaging of bacterial biofilms in flow channels

To test the performance of the flow channels with a live specimen, we acquired time-lapse 3D stacks of *S. oneidensis* MR-1 biofilms every thirty minutes for 20 hours at 30 ℃. A small number of surface-attached cells developed into a multi-layer biofilm that eventually covered the whole field of view at the 20 hour time point (**Figure 3.5a**). These results indicate that bacteria continue to proliferate within the flow channel and build biofilm structures in the presence of fluid flow, consistent with previous reports[46-48]. Leaching of uncrosslinked chemical compounds from the 3D-printed channel body is therefore not a phototoxicity concern, at least for *S. oneidensis* MR-1. Visual inspection of the obtained images show densely packed cells bodies, indicating that

cellular resolution is obtained at every time point without any noticeable degradation in image quality. To quantify these observations, we evaluated the resolution and signal-to-backgrond ratio of the images over time (**Figure 3.5b**). Although the SBR decreases as biofilms grow larger and denser, SBRs of >2 were maintained at every time point. The decreased SBRs can be attributed to an increased background due to greater light scattering off of the bacterial cells. Estimation of the image resolution showed that a spatial resolution ~500 nm was maintained over 20 hours. These results demonstrate that long-term single-cell biofilm imaging can be performed using LLSM and the flow channels reported here.

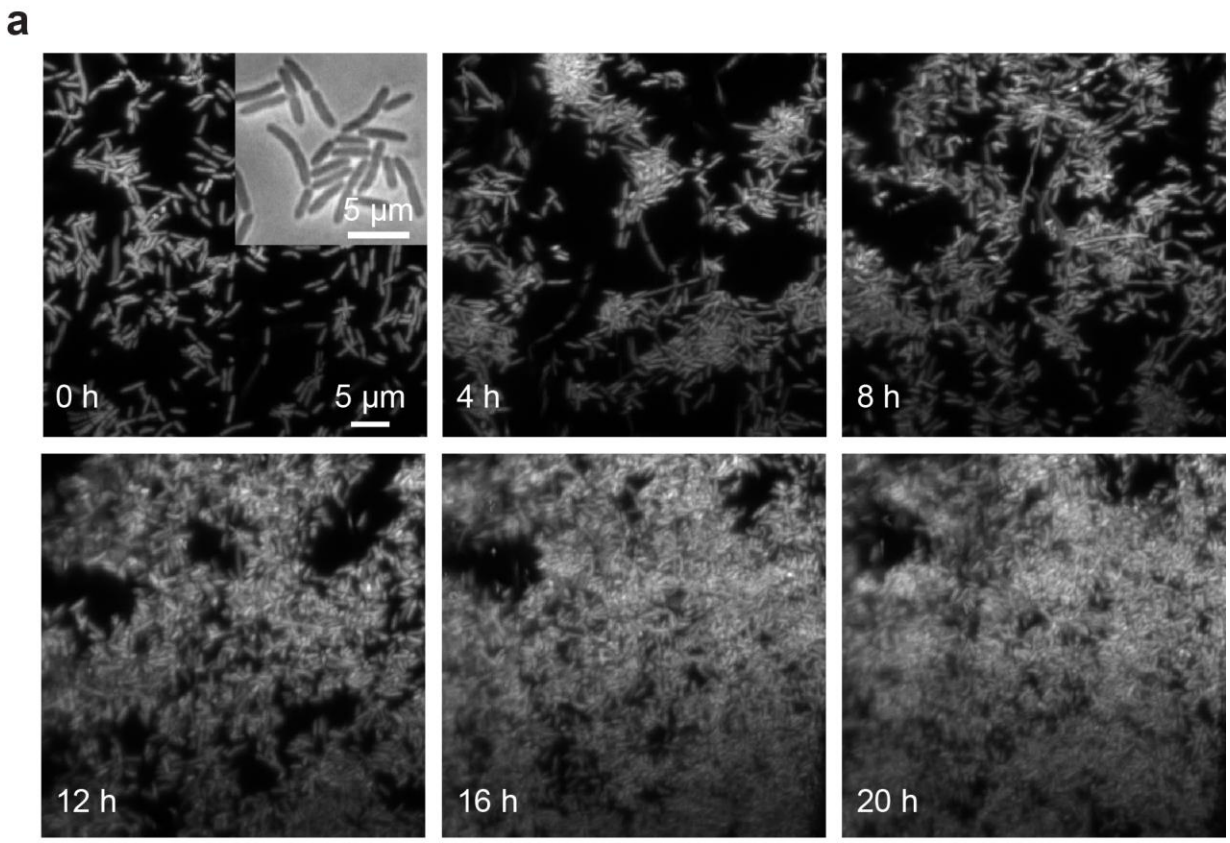
a
5 µm
0 h
5 µm
4 h
8 h
12 h
16 h
20 h

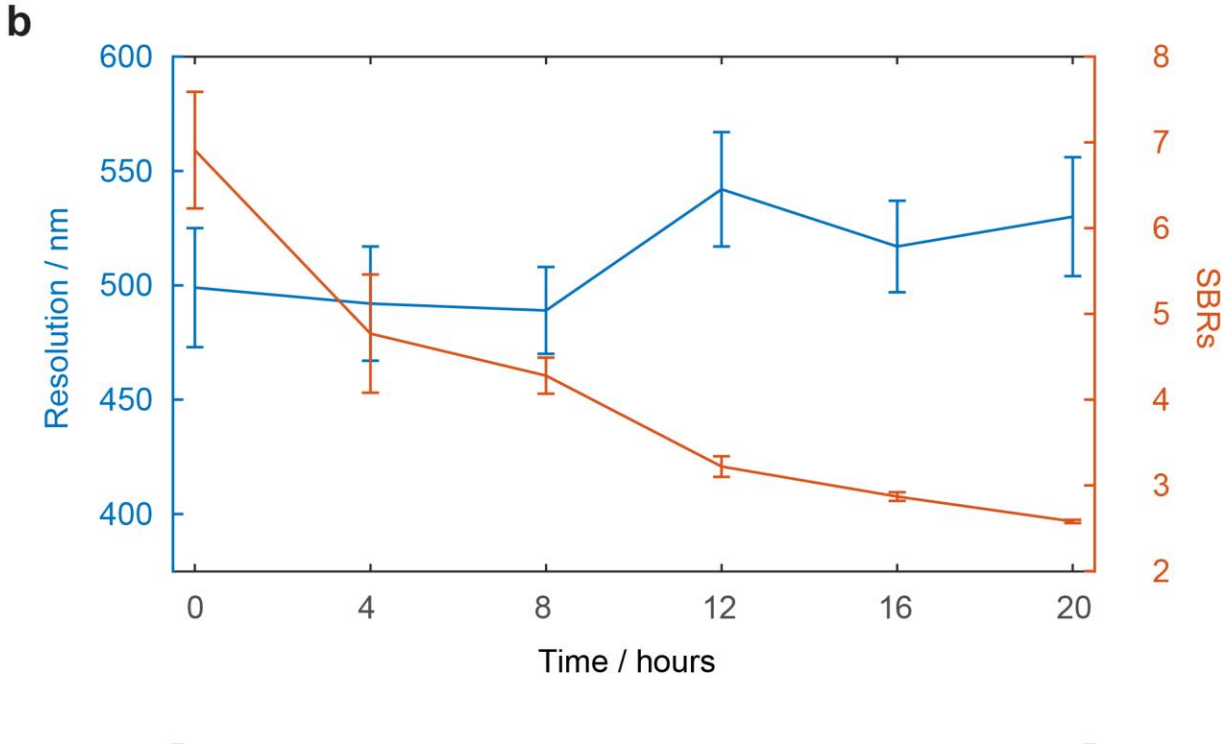
b
600
550
500
450
400
Resolution / nm
8
7
6
5
4
3
2
SBRs
0
4
8
12
16
20
Time / hours

Figure 3.5 Live-cell imaging of GFP expressing *S. oneidensis* MR-1 cells. (a) Maximum intensity projections show the initial 20 hours of *S. oneidensis* MR-1 biofilm development under fluid flow. The inset in the first image shows a phase contrast image of isolated *S. oneidensis* MR-1 cells on a glass coverslip. (b) Image resolution and SBR over 20 hours of imaging.

To demonstrate the advantage of using LLSM for long duration imaging, we have compared photobleaching between the LLSM and a spinning disk confocal microscope (Nikon Ti2 inverted microscope with a Yokogawa CSU-W1 SoRa spinning disk) (**Figure 3.6**). Comparisons were made by recording image volumes with similar voxel resolution (~100 nm) and similar initial SBRs using GFP expressing *Shewanella oneidensis* MR-1 biofilms. Consistent with previous reports comparing light sheet- to confocal-based approaches, our results show about an order of magnitude slower photobleaching when using LLSM. The decreased photobleaching rate of LLSM thus enables either long term time lapse image without substantial degradation of fluorescence intensity or increased frame rates (i.e. better time resolution) at comparable photobleaching rates. For the last image volume in **Figure 3.6**, the SBR obtained by the LLSM is ~56% higher than the SBR obtained by the spinning disk confocal microscope (2.57 vs 1.65). As systematically assessed in a recent study[41], an SBR of 2.57 vs 1.65 can make a huge difference for obtaining (or not obtaining) accurate cell segmentation results.

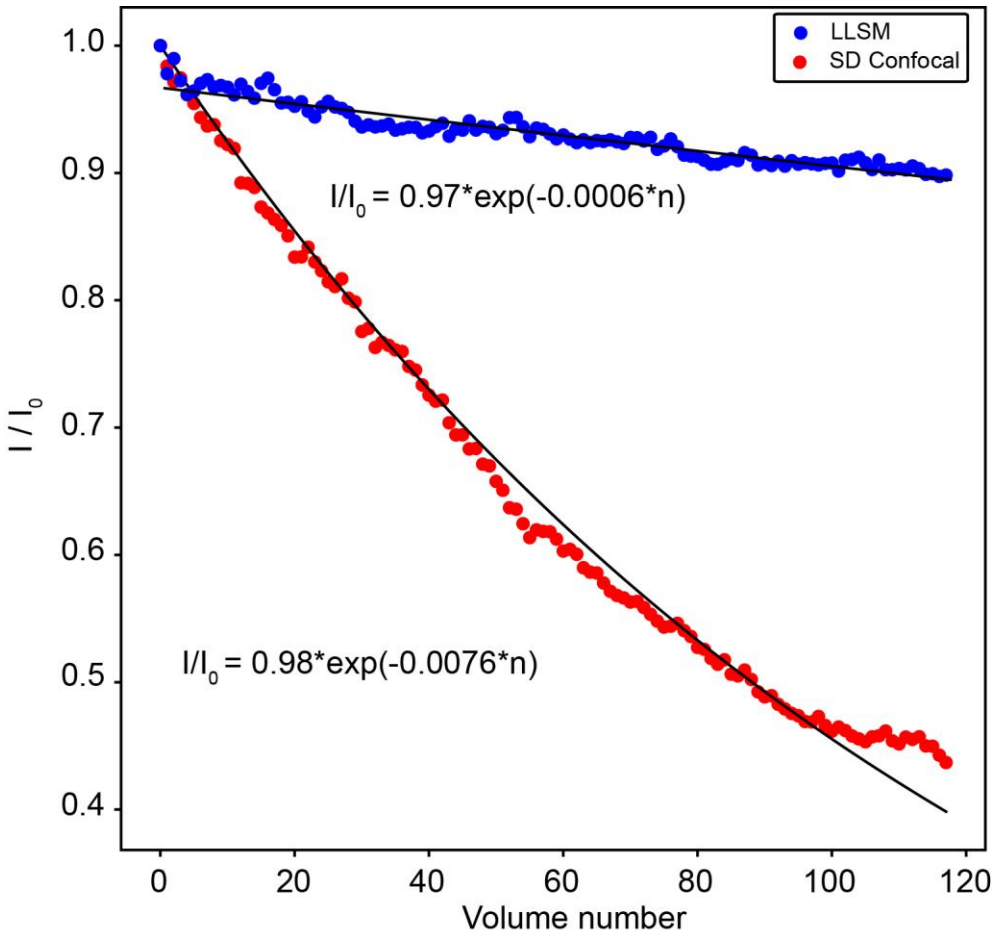

Figure 3.6 Quantitative comparison of photobleaching for LLSM and spinning disk confocal microscopy. Image volumes with similar voxel resolution (~100 nm) and initial signal-to-background ratios were recorded using GFP expressing Shewanella oneidensis MR-1 biofilms. Fluorescence intensity (normalized to the intensity of the first image volume I0) decreases as a function of acquired image volume. Data fitting using single-exponential decay functions show an order of magnitude decrease in the photobleaching rate for LLSM compared to confocal microscopy.

Previous studies have shown that *S. oneidensis* MR-1 biofilms form mushroom-like 3D structures after several days of development under fluid flow conditions[46, 47]. To test whether such

structures also manifest in our flow channels, we repeated the above experiment but continued to image until the 72-hour mark. *S. oneidensis* MR-1 biofilms indeed formed large mushroom-like structures that extended to about 20 μm above the growth substrate surface. The size of these structures is larger than the field of view of the LLSM. Therefore, a tiled image acquisition had to be used to capture these structures in their entirety. These volumetric image tiles were then computationally stitched together[44] into a 40 x 32 x 22 μm^3 image volume (**Figure 3.7a**). As is the case for every optical microscopy modality, image quality decreases when imaging deeper into a biological specimen that itself contains numerous refractive index boundaries. To quantify this effect in our images, we estimated the image resolution and SBR as a function of biofilm depth using the tallest mushroom-like structure in the imaged volume. SBR and spatial resolution in the selected image continually decreased as imaging depth increased (**Figure 3.7b**). However, even at the deepest part of the *S. oneidensis* MR-1 biofilm, cell bodies remain clearly visible at an estimated resolution better than 600 nm and an SBR >1.5. Preliminary segmentation results using BCM3D[41] indeed show physiologically reasonable cell shapes for a vast majority of cells (**Figure 3.7c**). We note however that cells located at the deepest parts of thick biofilms are still challenging for segmentation, due to the lower contrast and resolution. Future work will therefore focus on increasing the contrast and resolution in bacterial biofilm images. While the structure illumination mode of the LLSM can provide higher spatial resolution and better contrast, such improvements come at a cost of higher photobleaching/phototoxicity[23]. Software solutions that can process images with limited resolution and low SBRs will therefore play a tremendously important role. In light of these challenges, we are developing a segmentation pipeline that is more robust to low SBR images[49]. Furthermore, CNN-based image processing modules, such as CARE[11], Noise2Void[50], have shown great promise for contrast and resolution enhancement, and denoising.

Incorporating these tools into the segmentation workflow should help to further improve segmentation accuracies.

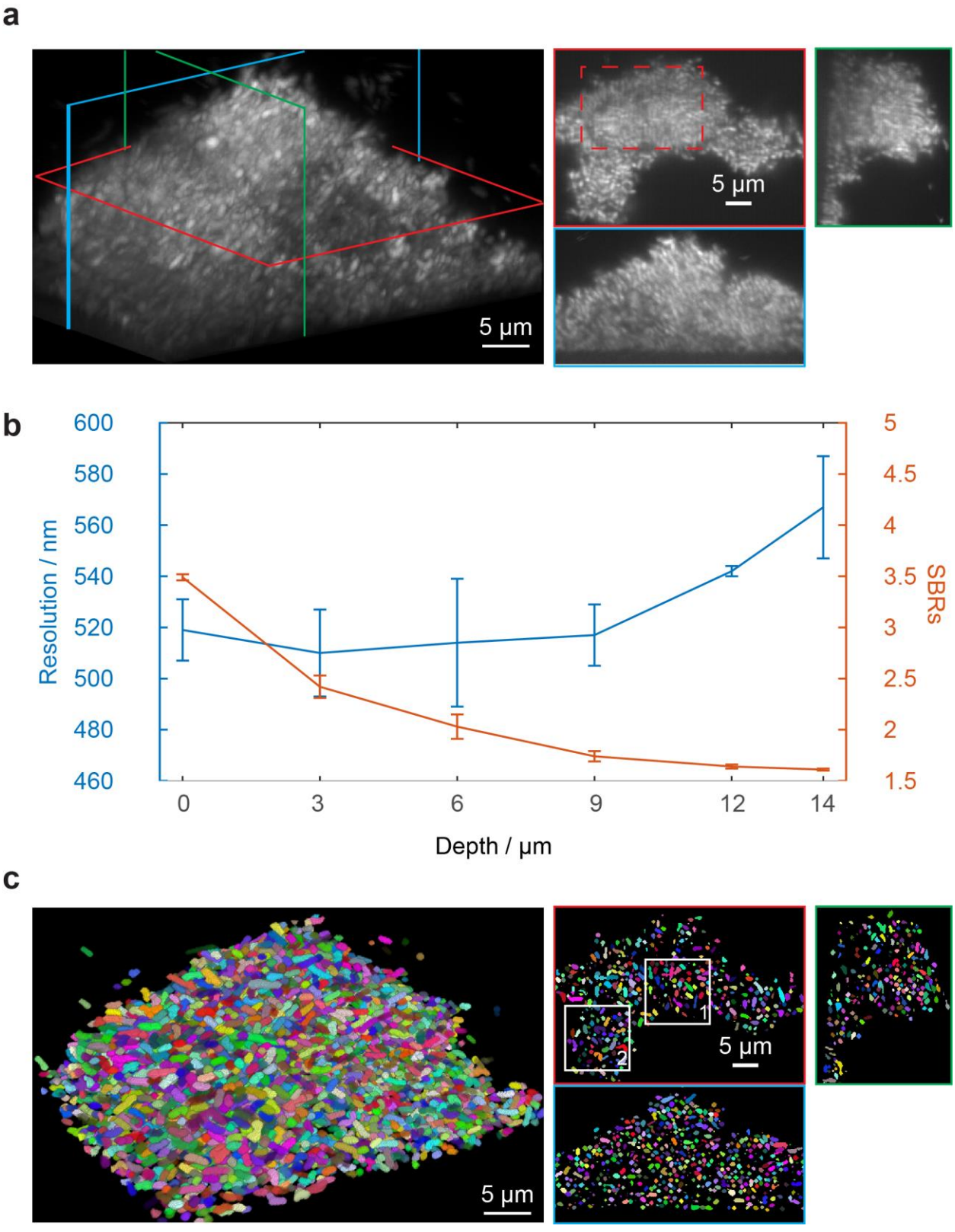
a
5 μm
5 μm
b
Resolution / nm
SBRs
Depth / μm
600
580
560
540
520
500
480
460
5
4.5
4
3.5
3
2.5
2
1.5
0
3
6
9
12
14
c
5 μm
5 μm
1
2

Figure 3.7 Live-cell imaging for GFP expressing *S. oneidensis* MR-1 biofilms. (a) 3D rendering and selected 2D slices of a mushroom-like structure with an *S. oneidensis* MR-1 biofilm after 72 hours of growth under fluid flow conditions. Colored rectangles in the 3D rendering indicate the position for the 2D slices shown to the right. The red dashed rectangle indicates the region used for evaluation in panel b. (b) Resolution and signal-to-background ratio (SBRs) as a function of imaging depth. (c) Preliminary segmentation results for the image shown in panel a. Different colors indicate different cells. White rectangles indicate two regions whose architectural properties are further analyzed in **Figure 3.8**. Image slices are the same as in panel a, as indicated by the colored outlines.

Two regions (indicated in **Figure 3.7c**) were further selected for a quantitative analysis of architectural parameters, including distance to the nearest neighbor, distance to the substrate surface, elevation angle, and azimuthal angle (**Figure 3.8**). The similar distribution of nearest neighbor distances indicates these two biofilm regions have similar cell density. In region 1, 41% of cells are more than 10 μm above the substrate surface, compared to only 8% of cells in region 2, which indicates region 1 is a taller biofilm structure. The generally low elevation indicates the number of vertically oriented cells is low in both regions in contrast to what is observed for submerged *Vibrio cholerae* biofilms[13, 51, 52]. Further, the two peaks at 0°/360° and 180° of the azimuthal angle distribution suggests bacterial cells in these two regions tend to align with the flow direction, which is consistent with *Vibrio cholerae* biofilms exposed to high shear stresses due to fluid flow[12]. Together these results demonstrate that our LLSM-compatible flow channels enable long-term time-lapse imaging of the complex 3D cellular architecture within bacterial biofilms.

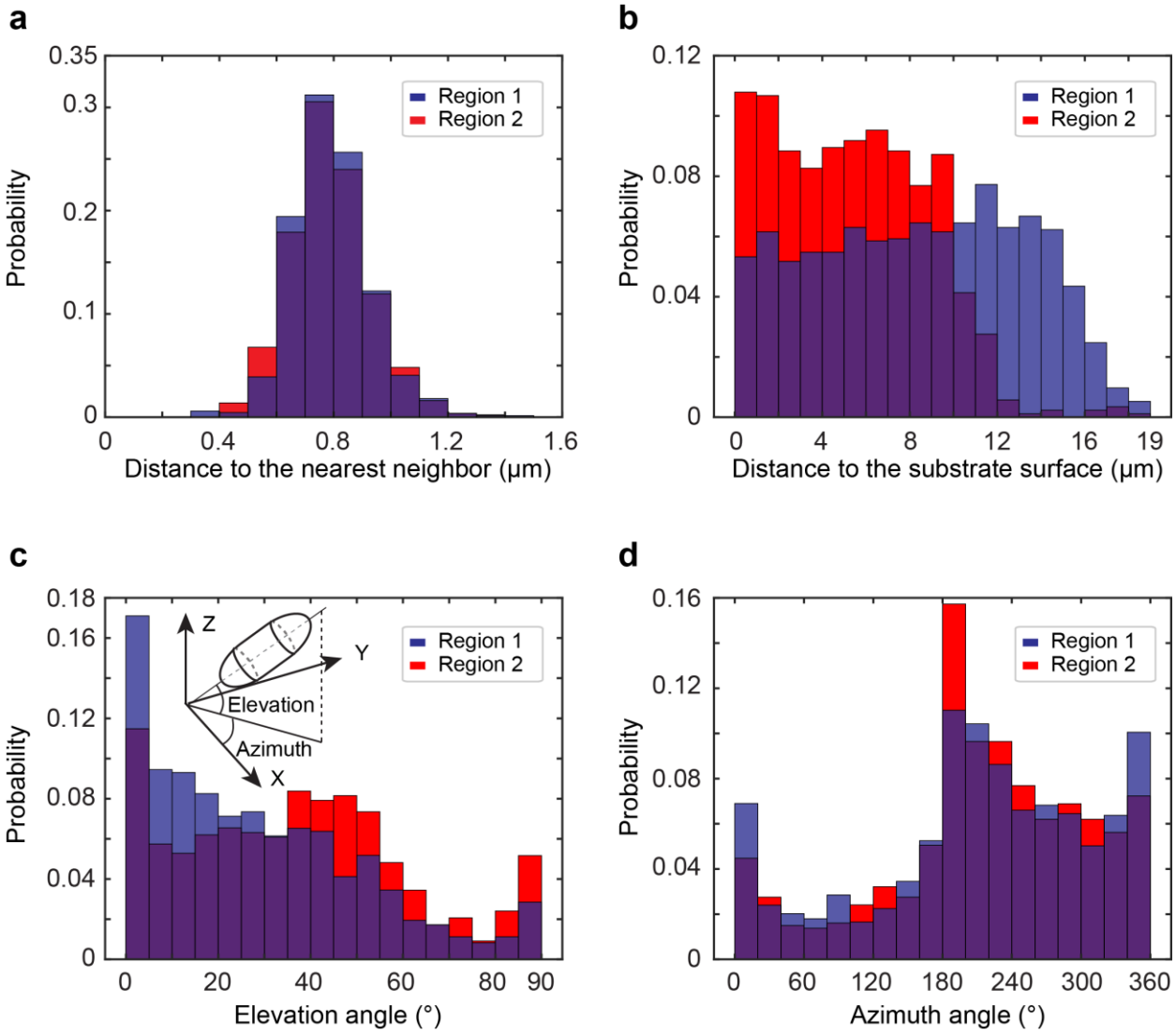

Figure 3.8 Comparison between cell-resolved biofilm architectural properties from two different biofilm regions (indicated in **Figure 3.7c**). Region 1 contains 1333 cells and Region 2 contains 871 cells. (a) Distance to the nearest neighbor cell. (b) Distance to the substrate surface. (c) Elevation angle of segmented cells. (d) Azimuthal angle of segmented cells.

3.4 Conclusions

Owing to its high spatiotemporal resolution, low photobleaching, and minimal phototoxicity, LLSM and high-NA light sheet-based fluorescence microscopy modalities in

general have emerged as the method of choice for live-cell imaging. Depending on the implementation, specimens are imaged from top to bottom or from bottom to top. Due to the open-on-top imaging geometry of the initial LLSM implementation, this microscope modality has not been applicable for microbiological research for which sample containment is paramount. Here, we have addressed this limitation by integrating LLSM with 3D-printed microfluidic flow channels. These channels enable top-to-bottom imaging of bacterial biofilms at unprecedented spatiotemporal resolution on arbitrary, and even non-transparent surfaces. Imaging is performed through an ultrathin polymer film that closely matches the refractive index of the aqueous bacterial growth medium and does not itself get colonized by bacterial biofilms. Precise refractive index matching ($\Delta n < 10^{-3}$) was found to be necessary to minimize optical aberrations and thereby enable high resolution imaging. Using MY133-V2000 polymer films, it was possible to record 3D time-lapse images of bacterial biofilms at cellular resolution over periods of several days without noticeable degradation in image quality.

The reported LLSM-integrated microfluidic system isolates biofilm samples from the outside environment, which prevents contamination of the microscope components and provides a precisely controllable physico-chemical environment for long duration time-lapse imaging. In this study, we recorded the colonization of glass surfaces by *S. oneidensis* MR-1 biofilms under fluid flow over a time period of three days, visualizing the evolution of single surface-attached cells into a large 3D biofilm. Longer imaging experiments are possible. While the present channel enables imaging of bacterial populations growing on abiotic substrates, we envision that, with minor modifications, the current design can be adapted to image bacterial population interacting with human organoid-derived epithelia, which have recently been stably reconstituted in dual-channel microphysiological devices[53, 54]. Visualizing how single bacterial cells cooperate or

antagonize each other in heterogeneous biofilm environments holds the key to rational design of microbial ecosystems with desirable functional capabilities in physiologically relevant environments[55-58].

References

1. Zhang, J.; Zhang, M.; Wang, Y., et al., Optically Accessible Microfluidic Flow Channels for Noninvasive High-Resolution Biofilm Imaging Using Lattice Light Sheet Microscopy. *The Journal of Physical Chemistry B* **2021,** *125* (44), 12187-12196.

2. Flemming, H.-C.; Wingender, J., The biofilm matrix. *Nature reviews microbiology* **2010,** *8* (9), 623-633.

3. Jayathilake, P. G.; Gupta, P.; Li, B., et al., A mechanistic Individual-based Model of microbial communities. *PLoS One* **2017,** *12* (8), e0181965.

4. Nadell, C. D.; Drescher, K.; Foster, K. R., Spatial structure, cooperation and competition in biofilms. *Nature Reviews Microbiology* **2016,** *14* (9), 589.

5. Flemming, H. C.; Wingender, J.; Szewzyk, U., et al., Biofilms: an emergent form of bacterial life. *Nat Rev Microbiol* **2016,** *14* (9), 563-75.

6. Nadell, C. D.; Xavier, J. B.; Foster, K. R., The sociobiology of biofilms. *FEMS microbiology reviews* **2008,** *33* (1), 206-224.

7. Yan, J.; Bassler, B. L., Surviving as a community: antibiotic tolerance and persistence in bacterial biofilms. *Cell host & microbe* **2019,** *26* (1), 15-21.

8. Frost, I.; Smith, W. P.; Mitri, S., et al., Cooperation, competition and antibiotic resistance in bacterial colonies. *The ISME journal* **2018,** *12* (6), 1582-1593.

9. De la Fuente-Núñez, C.; Reffuveille, F.; Fernández, L., et al., Bacterial biofilm development as a multicellular adaptation: antibiotic resistance and new therapeutic strategies. *Current opinion in microbiology* **2013,** *16* (5), 580-589.

10. Hall-Stoodley, L.; Costerton, J. W.; Stoodley, P., Bacterial biofilms: from the natural environment to infectious diseases. *Nature reviews microbiology* **2004,** *2* (2), 95-108.

11. Weigert, M.; Schmidt, U.; Boothe, T., et al., Content-aware image restoration: pushing the limits of fluorescence microscopy. *Nature methods* **2018,** *15* (12), 1090-1097.

12. Hartmann, R.; Singh, P. K.; Pearce, P., et al., Emergence of three-dimensional order and structure in growing biofilms. *Nature Physics* **2019,** *15* (3), 251-256.

13. Qin, B.; Fei, C.; Bridges, A. A., et al., Cell position fates and collective fountain flow in bacterial biofilms revealed by light-sheet microscopy. *Science* **2020,** *369* (6499), 71-77.

14. Stelzer, E. H., Light-sheet fluorescence microscopy for quantitative biology. *Nature methods* **2015,** *12* (1), 23-26.

15. Power, R. M.; Huisken, J., A guide to light-sheet fluorescence microscopy for multiscale imaging. *Nature methods* **2017,** *14* (4), 360-373.

16. Jemielita, M.; Taormina, M. J.; DeLaurier, A., et al., Comparing phototoxicity during the development of a zebrafish craniofacial bone using confocal and light sheet fluorescence microscopy techniques. *Journal of biophotonics* **2013,** *6* (11‐12), 920-928.

17. Voleti, V.; Patel, K. B.; Li, W., et al., Real-time volumetric microscopy of in vivo dynamics and large-scale samples with SCAPE 2.0. *Nature methods* **2019,** *16* (10), 1054-1062.

18. Parthasarathy, R., Monitoring microbial communities using light sheet fluorescence microscopy. *Current opinion in microbiology* **2018,** *43*, 31-37.

19. Olarte, O. E.; Andilla, J.; Gualda, E. J., et al., Light-sheet microscopy: a tutorial. *Advances in Optics and Photonics* **2018,** *10* (1), 111-179.

20. Rosenberg, J.; Cao, G.; Borja-Prieto, F., et al., Lattice light-sheet microscopy multi-dimensional analyses (LaMDA) of T-cell receptor dynamics predict T-cell signaling states. *Cell systems* **2020,** *10* (5), 433-444. e5.

21. Mimori-Kiyosue, Y., Imaging mitotic processes in three dimensions with lattice light-sheet microscopy. *Chromosome Research* **2021**, 1-14.

22. Manley, H. R.; Potter, D. L.; Heddleston, J. M., et al., Frontline Science: Dynamic cellular and subcellular features of migrating leukocytes revealed by in vivo lattice lightsheet microscopy. *Journal of leukocyte biology* **2020,** *108* (2), 455-468.

23. Chen, B.-C.; Legant, W. R.; Wang, K., et al., Lattice light-sheet microscopy: imaging molecules to embryos at high spatiotemporal resolution. *Science* **2014,** *346* (6208).

24. Wu, Y.; Wawrzusin, P.; Senseney, J., et al., Spatially isotropic four-dimensional imaging with dual-view plane illumination microscopy. *Nature biotechnology* **2013,** *31* (11), 1032-1038.

25. Gao, R.; Asano, S. M.; Upadhyayula, S., et al., Cortical column and whole-brain imaging with molecular contrast and nanoscale resolution. *Science* **2019,** *363* (6424), eaau8302.

26. Høiby, N.; Ciofu, O.; Bjarnsholt, T., Pseudomonas aeruginosa biofilms in cystic fibrosis. *Future microbiology* **2010,** *5* (11), 1663-1674.

27. Nickerson, K. P.; Chanin, R. B.; Sistrunk, J. R., et al., Analysis of Shigella flexneri Resistance, Biofilm Formation, and Transcriptional Profile in Response to Bile Salts. *Infect Immun* **2017,** *85* (6).

28. Langdon, S. P., Cell culture contamination. *Cancer Cell Culture* **2004**, 309-317.

29. Kim, J.; Park, H.-D.; Chung, S., Microfluidic approaches to bacterial biofilm formation. *Molecules* **2012,** *17* (8), 9818-9834.

30. Azeredo, J.; Azevedo, N. F.; Briandet, R., et al., Critical review on biofilm methods. *Critical reviews in microbiology* **2017,** *43* (3), 313-351.

31. Thomen, P.; Robert, J.; Monmeyran, A., et al., Bacterial biofilm under flow: first a physical struggle to stay, then a matter of breathing. *PloS one* **2017,** *12* (4), e0175197.

32. Coyte, K. Z.; Tabuteau, H.; Gaffney, E. A., et al., Microbial competition in porous environments can select against rapid biofilm growth. *Proceedings of the National Academy of Sciences* **2017,** *114* (2), E161-E170.

33. Yordanov, S.; Neuhaus, K.; Hartmann, R., et al., Single-objective high-resolution confocal light sheet fluorescence microscopy for standard biological sample geometries. *Biomedical optics express* **2021,** *12* (6), 3372-3391.

34. Yang, B.; Chen, X.; Wang, Y., et al., Epi-illumination SPIM for volumetric imaging with high spatial-temporal resolution. *Nature methods* **2019,** *16* (6), 501-504.

35. Millett-Sikking, A.; Dean, K. M.; Fiolka, R., et al., High NA single-objective light-sheet. **2019**, doi:10.5281/zenodo.3244420.

36. Yawata, Y.; Nguyen, J.; Stocker, R., et al., Microfluidic studies of biofilm formation in dynamic environments. *Journal of bacteriology* **2016,** *198* (19), 2589-2595.

37. Straub, H.; Eberl, L.; Zinn, M., et al., A microfluidic platform for in situ investigation of biofilm formation and its treatment under controlled conditions. *Journal of nanobiotechnology* **2020,** *18* (1), 1-12.

38. Raman, K.; Murthy, T. S.; Hegde, G., Fabrication of refractive index tunable polydimethylsiloxane photonic crystal for biosensor application. *Physics Procedia* **2011,** *19*, 146-151.

39. Liu, T.-L.; Upadhyayula, S.; Milkie, D. E., et al., Observing the cell in its native state: Imaging subcellular dynamics in multicellular organisms. *Science* **2018,** *360* (6386).

40. Fan, Y.-J.; Hsieh, H.-Y.; Tsai, S.-F., et al., Microfluidic channel integrated with a lattice lightsheet microscopic system for continuous cell imaging. *Lab on a chip* **2021,** *21* (2), 344-354.

41. Zhang, M.; Zhang, J.; Wang, Y., et al., Non-invasive single-cell morphometry in living bacterial biofilms. *Nature communications* **2020,** *11* (1), 1-13.

42. Jeckel, H.; Drescher, K., Advances and opportunities in image analysis of bacterial cells and communities. *FEMS Microbiology Reviews* **2020**.

43. Descloux, A.; Grußmayer, K. S.; Radenovic, A., Parameter-free image resolution estimation based on decorrelation analysis. *Nature Methods* **2019,** *16* (9), 918-924.

44. Hörl, D.; Rusak, F. R.; Preusser, F., et al., BigStitcher: reconstructing high-resolution image datasets of cleared and expanded samples. *Nature Methods* **2019,** *16* (9), 870-874.

45. Pettersen, E. F.; Goddard, T. D.; Huang, C. C., et al., UCSF ChimeraX: Structure visualization for researchers, educators, and developers. *Protein Science* **2021,** *30* (1), 70-82.

46. Thormann, K. M.; Saville, R. M.; Shukla, S., et al., Initial phases of biofilm formation in Shewanella oneidensis MR-1. *Journal of bacteriology* **2004,** *186* (23), 8096-8104.

47. Teal, T. K.; Lies, D. P.; Wold, B. J., et al., Spatiometabolic stratification of Shewanella oneidensis biofilms. *Applied and Environmental Microbiology* **2006,** *72* (11), 7324-7330.

48. Thormann, K. M.; Saville, R. M.; Shukla, S., et al., Induction of rapid detachment in Shewanella oneidensis MR-1 biofilms. *Journal of bacteriology* **2005,** *187* (3), 1014-1021.

49. Ji Zhang, Y. W., Eric Donarski, Andreas Gahlmann, BCM3D 2.0: Generation of intermediate image representations for accurate detection of single cells in bacterial biofilms. *In preparation*.

50. Krull, A.; Buchholz, T.-O.; Jug, F. In *Noise2void-learning denoising from single noisy images*, Proceedings of the IEEE/CVF Conference on Computer Vision and Pattern Recognition, 2019; pp 2129-2137.

51. Yan, J.; Sharo, A. G.; Stone, H. A., et al., Vibrio cholerae biofilm growth program and architecture revealed by single-cell live imaging. *Proceedings of the National Academy of Sciences* **2016,** *113* (36), E5337-E5343.

52. Drescher, K.; Dunkel, J.; Nadell, C. D., et al., Architectural transitions in Vibrio cholerae biofilms at single-cell resolution. *Proceedings of the National Academy of Sciences* **2016,** *113* (14), E2066-E2072.

53. Tovaglieri, A.; Sontheimer-Phelps, A.; Geirnaert, A., et al., Species-specific enhancement of enterohemorrhagic E. coli pathogenesis mediated by microbiome metabolites. *Microbiome* **2019,** *7* (1).

54. Steinway, S. N.; Saleh, J.; Koo, B.-K., et al., Human Microphysiological Models of Intestinal Tissue and Gut Microbiome. *Frontiers in Bioengineering and Biotechnology* **2020,** *8* (725).

55. Fredrickson, J. K., Ecological communities by design. *Science* **2015,** *348* (6242), 1425-1427.

56. Grosskopf, T.; Soyer, O. S., Synthetic microbial communities. *Curr Opin Microbiol* **2014,** *18*, 72-7.

57. Jagmann, N.; Philipp, B., Design of synthetic microbial communities for biotechnological production processes. *J Biotechnol* **2014,** *184,* 209-18.

58. Kouzuma, A.; Kato, S.; Watanabe, K., Microbial interspecies interactions: recent findings in syntrophic consortia. *Front Microbiol* **2015,** *6,* 477.

Chapter 4 Non-Invasive Single-Cell Morphometry in Living Bacterial Biofilms

This chapter is adapted from Zhang, M., Zhang, J. (contributed equally), et al. *Nat Commun.* **2020,** *11* (1), 1-13[1].

4.1 Introduction

Biofilms are multicellular communities of microorganisms that grow on biotic or abiotic surfaces[2-5]. In addition to cellular biomass, biofilms also contain an extracellular matrix (ECM) which is composed of polysaccharides, DNA, and proteins. Individual cells in biofilms interact with other cells, the ECM, or with the substrate surface, and the sum total of these interactions provide bacterial biofilms with emergent functional capabilities beyond those of individual cells. For example, biofilms are orders of magnitude more tolerant towards physical, chemical, and biological stressors, including antibiotic treatments and immune system clearance[2, 3, 6-9]. Understanding how such capabilities emerge from the coordination of individual cell behaviors requires imaging technologies capable of resolving and simultaneous tracking of individual bacterial cells in 3D biofilms.

Live cell-compatible imaging technologies, such as optical microscopy, can reveal the spatial and temporal context that affects cellular behaviors. However, conventional imaging modalities are not able to resolve individual cells within thick 3D biofilms over extended periods of time. For example, the diffraction-limited lateral resolution (~230 nm) of a confocal fluorescence microscope is barely sufficient to resolve bacterial cells positioned next to each other on flat glass coverslips. Even worse, the diffraction-limited axial resolution (570 nm) is

comparable to the size of a single bacterial cell, so that densely-packed cells become unresolvable in the axial *z*-dimension[10, 11]. Notable exceptions include loose biofilms (low cell density), spherical cell shapes[12, 13], and mutant *Vibrio cholera* biofilms, in which cell-cell spacing is increased through the overproduction of ECM materials[14-16]. While single-cell resolved images have been obtained in such special situations, conventional optical microscopy modalities are not generally capable to accurately resolve and quantitatively track individual cells in dense 3D biofilms.

While super-resolution derivatives of confocal microscopy, known as Image Scanning Microscopy[17], can improve spatial resolution, a perhaps more important limitation for long-term live-cell imaging is photodamage to the specimen (phototoxicity) and to the fluorophores used for labeling (photobleaching)[18-20]. In confocal microscopy-based approaches, undesired out-of-focus fluorescence emission is filtered out by confocal pinholes to yield optically-sectioned images with high contrast, i.e., high signal-to-background ratios (SBRs). However, repeated illumination of out-of-focus regions during laser scanning and high light intensities at the focal volume result in rapid photobleaching of fluorophores and unacceptable phototoxicity for light sensitive specimens [18-20]. In fact, confocal fluorescence microscopy (as well as its super-resolution derivatives) uses illumination light intensities that are two to three orders of magnitude higher than the light intensities under which life has evolved[19]. The high rates of phototoxicity and photobleaching make confocal-based microscopy unsuitable for high frame-rate time-lapse imaging of living specimens over many hours and days[15, 16, 18, 21, 22].

In recent years, light sheet-based fluorescence excitation and imaging approaches have been developed to overcome the drawbacks of confocal microscopy. Among these, lattice light sheet microscopy (LLSM)[19, 20] and field synthesis variants thereof[23], axially-swept light sheet

microscopy (ASLM)[24, 25], dual-view light sheet microscopy[26, 27], and single-objective oblique plane light sheet microscopy[28-32] now combine excellent 3D spatial resolution with fast temporal resolution and low phototoxicity at levels that cannot be matched by confocal microscopy. Specifically, light sheet-based microscopy approaches can operate at illumination intensities that are below the levels of cellular phototoxicity, even for notoriously light sensitive specimens, and reduce fluorophore photobleaching by 20-50 times compared to confocal microscopy, while maintaining comparable spatial resolution and contrast/SBR[19, 29].

An additional challenge in high-resolution biofilm imaging is data quantification. Even if sufficient resolution and high SBRs can be achieved to visually discern, i.e., qualitatively resolve individual cells, robust computational algorithms are still needed for automated cell segmentation and quantitative cell tracking. Towards this goal, image processing approaches based on the watershed technique and intensity thresholding have been developed over the years for single-cell segmentation in bacterial biofilms[14-16, 22]. The broad applicability of watershed- and threshold-based image processing algorithms is however limited, because these algorithms require manual optimization of many user-selected parameters. Even with optimal parameters, watershed- and threshold-based image processing methods often produce sub-optimal segmentation results, especially when cell densities are high, when SBRs are low, and when cellular fluorescence intensities are not uniform across the cytosol or the cell surface. To overcome the drawbacks of traditional mathematical image processing approaches, automated solutions based on supervised training of deep convolutional neural networks (CNNs) have been used in recent years with great success for a wide range of problems in biomedical image analysis[33].

Here, we present Bacterial Cell Morphometry 3D (*BCM3D*)[34], a generally applicable workflow for single-cell segmentation and shape determination in high-resolution 3D images of

bacterial biofilms. *BCM3D* uses CNNs, *in silico*-trained with computationally simulated biofilm images, in combination with mathematical image analysis to achieve accurate single cell segmentation in 3D. The CNNs employed in *BCM3D* are based on the 3D U-Net architecture and training strategy, which has achieved excellent performance in biomedical data analysis benchmark tests[33]. The mathematical image analysis modules of *BCM3D* enable post-processing of the CNN results to further improve the segmentation accuracy. We establish that experimental bacterial biofilms images, acquired by lattice light sheet microscopy, can be successfully segmented using CNNs trained with computationally simulated biofilm images, for which the ground-truth voxel-level annotation maps are known accurately and precisely. By systematically evaluating the performance of *BCM3D* for a range of SBRs, cell densities, and cell shapes, we find that voxel-level segmentation accuracies of >80%, as well as cell counting accuracies of >90%, can be robustly achieved. *BCM3D* consistently outperforms previously reported image segmentation approaches that rely exclusively on conventional image processing approaches. *BCM3D* also achieves higher segmentation accuracy on experimental 3D biofilm data than *Cellpose*[35], a state-of-the-art, CNN-based, generalist algorithm for cell segmentation and the algorithm used by Hartmann *et al.*[16], a specialized algorithm designed for bacterial cell segmentation based on traditional mathematical image processing. We expect that *BCM3D*, and CNN-based single-cell segmentation approaches in general, combined with non-invasive light sheet-based fluorescence microscopy will enable accurate cell tracking over time in dense 3D biofilms. This capability will launch a new era for bacterial biofilm research, in which the emergent properties of microbial populations can be studied in terms of the fully-resolved behavioral phenotypes of individual cells.

4.2 Methods

4.2.1 Imaging of bacterial biofilms with LLSM

Fluorescence images of bacterial biofilms were acquired on a home-built lattice light sheet microscope (LLSM). LLSM enables specimen illumination with a thin light sheet derived from 2D optical lattice[19, 36]. Here, a continuous illumination light sheet was produced by a time-averaged (dithered), square lattice pattern[19], and the illumination intensity at the sample was <1 W/cm^2. The submicrometer thickness of the excitation light sheet is maintained over long propagation distances (~30 μm), which enables optical sectioning, and thus high resolution, high contrast imaging of 3D specimens comparable to confocal microscopy. However, fluorophore excitation by a 2D light sheet reduces phototoxicity, because each excitation photon has multiple opportunities to be absorbed by fluorophores in the excitation plane and produce in-focus fluorescence. Widefield fluorescence images corresponding to each illuminated specimen plane are recorded on a sCMOS detector (Hamamatsu ORCA Flash v2). In this work, 3D biofilm images were acquired by translating the specimen through the light sheet in 200 nm steps using a piezo nanopositioning stage (Mad City Labs, NanoOP100HS). The data acquisition program is written in LabVIEW 2013 (National Instruments).

Ampicillin resistant *E.coli* K12, constitutively expressing GFP[37], were cultured at 37 °C overnight in LB medium with 100 μg/ml ampicillin. Overnight cultures were diluted 100 times into the same culture medium, grown to an optical density at 600 nm (OD600) of 0.6 – 1.0, and then diluted by an additional factor of 10. Round glass coverslips with the diameter of 5 mm were put into a 24-well plate (Falcon) and 400 μL of cell culture was added to the well. Cells were allowed to settle to the bottom of the well and adhere to the coverslip for 1 hour. The round

coverslips were then mounted onto a sample holder and placed into the LLSM sample-basin filled with M9 medium. GFP fluorescence was excited using 488 nm light sheet excitation. Biofilm growth was imaged at room temperature every 30 min for a total of 20 time points. At each time point, a single 3D image stack contained 400 images, each acquired with a 15 ms exposure time to avoid motion blur.

M.xanthus strain LS3908 expressing tdTomato under the control of the IPTG-inducible promoter [38] and DK1622 (WT) were cultured in the nutrient rich CYE media at 30 °C until it reached an OD600 of 0.6 - 1.0. Media was supplemented with 1 mM IPTG for tdTomato expressing cells. Chitosan (Thermo Fisher)-coated 5 mm round glass coverslips were prepared by incubating coverslips with 1% (w/v) chitosan (1.5 % glacial acetic acid (v/v)) at room temperature for 1 hour. Coverslips were then rinsed with water and placed into a 24-well plate (Falcon) with 350-400 μL of undiluted cell culture. WT cells were stained directly in the 24 well plate with 5 ng/ml FM4-64 (Thermo Fisher) dye. Cells were allowed to settle and adhere to the coverslip for 2 hours. After the settling period, the coverslip was gently rinsed with CYE media to flush away unattached cells. The rinsed coverslip was then mounted onto a sample holder and placed into the LLSM sample-basin filled with MC7 starvation buffer. tdTomato and FM 4-64 fluorescence was excited using 561 nm light sheet excitation. The 3D image stack contained 400 2D images. Each 2D slice was acquired with an exposure time of 30 ms.

For mixed population biofilm imaging, ampicillin resistant *E.coli* K12, constitutively expressing GFP[37], and ampicillin resistant *E.coli* K12, expressing mScarlet (pBAD vector, arabinose induce) were cultured separately at 37 °C overnight in LB medium with 100 μg/ml ampicillin. Overnight cultures were diluted 100 times into the same culture medium, grown to an optical density at 600 nm (OD600) of 0.6 – 1.0, and then diluted to an OD of 0.1. After dilution,

the two strains were mixed together. Round glass coverslips with the diameter of 5 mm were put into a 24-well plate (Falcon) and 500 μL of cell culture was added to the well. Cells were allowed to settle to the bottom of the well and adhere to the coverslip for 1 hour. The cell culture medium was then removed and replaced by 500 uL M9 medium containing 0.2% (w/v) arabinose. The co-culture was incubated at 30 °C overnight. 10 mins before imaging, the co-culture was stained with 5 ng/ml FM4-64 (Thermo Fisher) dye. 3D image stacks of 201 planes with 5 ms exposure time per frame were acquired using 488 nm excitation.

4.2.2 Raw data processing

Raw 3D images were background subtracted and then deskewed and deconvolved as described previously[19, 20]. The background was estimated by averaging intensity values of dark areas (devoid of cells) in the field of view. Deconvolution was performed using the Richardson-Lucy algorithm with 10 iterations using experimentally measured point spread functions (PSFs) as the deconvolution kernel. The experimentally measured PSFs were obtained separately for each color channel using fluorescent beads (200 nm FluoSpheres®, Thermo Fisher) coated on a coverslip[39]. 3D images were rendered using the 3D Viewer plugin in Fiji[40] or ChimeraX[41].

4.2.3 Generation of simulated biofilm images

To generate data for training of CNNs, we computationally simulated fluorescence images of 3D biofilms, for which spatial arrangements among individual cells are known precisely and accurately. Growth and division of individual rod-shaped cells in a population were simulated using CellModeller, an individual-based computational model of biofilm growth (**Figure 4.1a**)[42]. In individual-based biofilm growth models, cells are the basic modeling units. Each cell is characterized by a set of parameters, including its 3D position, volume, and spatial orientation. All

the cells in the simulated biofilm are then allowed to evolve in time according to predefined biological, chemical, and mechanical rules. For example, cells grow at a defined rate and then divide after reaching a certain volume threshold. Cellular collisions that are due to cell growth are alleviated by imposing a minimum distance criterion between cells at each time point. For our simulations, we chose cell diameter and cell length (d, l) parameters consistent with a given bacterial species, namely (1 μm, 3 μm) for *E. coli*[43], (0.7 μm, 6 μm) for *M. xanthus*[44], and (1 μm, 1 μm) for spherically symmetric *S.aureus*[45]. While the cell volume can be readily adjusted in CellModeller, the cellular volume density, which is determined by the intercellular spacing, is not directly adjustable. We therefore adjusted the cellular volume density after each simulation by scaling the cellular positions (cell centroids) and thus the intercellular distances by a constant factor, while leaving cell sizes, shapes, and orientations unchanged. This post-processing procedure enabled simulation of the exact same 3D cell arrangements at adjustable cell volume densities.

We fluorescently labeled simulated cell volumes and surfaces according to two commonly used labeling strategies in fluorescence microscopy. To simulate expression of intracellular fluorescent proteins, the fluorescence emitters were placed at random positions within the cell volume. To simulate membrane staining, the fluorescence emitters were placed at random positions on the cell surface. Each cell contained between 500 - 1000 fluorophores to simulate expression level variations between cells, which is often observed in experimental images. Once the fluorophore spatial distributions were determined, a 3D fluorescence image (**Figure 4.1b**) was computationally generated. Each fluorophore was treated as an isotropic point emitter, so that it would produce a diffraction-limited point-spread-function (PSF) on the detector. Experimentally measured 3D PSF shapes (see 4.2.2 Raw data processing) were used as the convolution kernel.

Next, the fluorescence signal intensity was scaled by multiplying the image by a constant factor and then a constant background intensity was added to the image at ~200 photons per pixel, as measured in experimental data. This procedure enabled independent adjustments of the fluorescence signal and background to obtain signal-to-background ratios (SBRs) consistent with experimental data. In a final step, we introduced Poisson-distributed counting noise, based on the summed background and signal intensities, as well as Gaussian-distributed camera read-out noise (experimentally calibrated for our detector at 3.04 photons per pixel on average)[46]. This resulting image data (**Figure 4.1c**) was then processed in the same manner as experimental data (see 4.2.2 Raw data processing). In contrast to experimental data, generation of the corresponding voxel-level annotation maps is fast and error free, because the underlying ground truth cell arrangements are known *a priori* (**Figure 4.1d**).

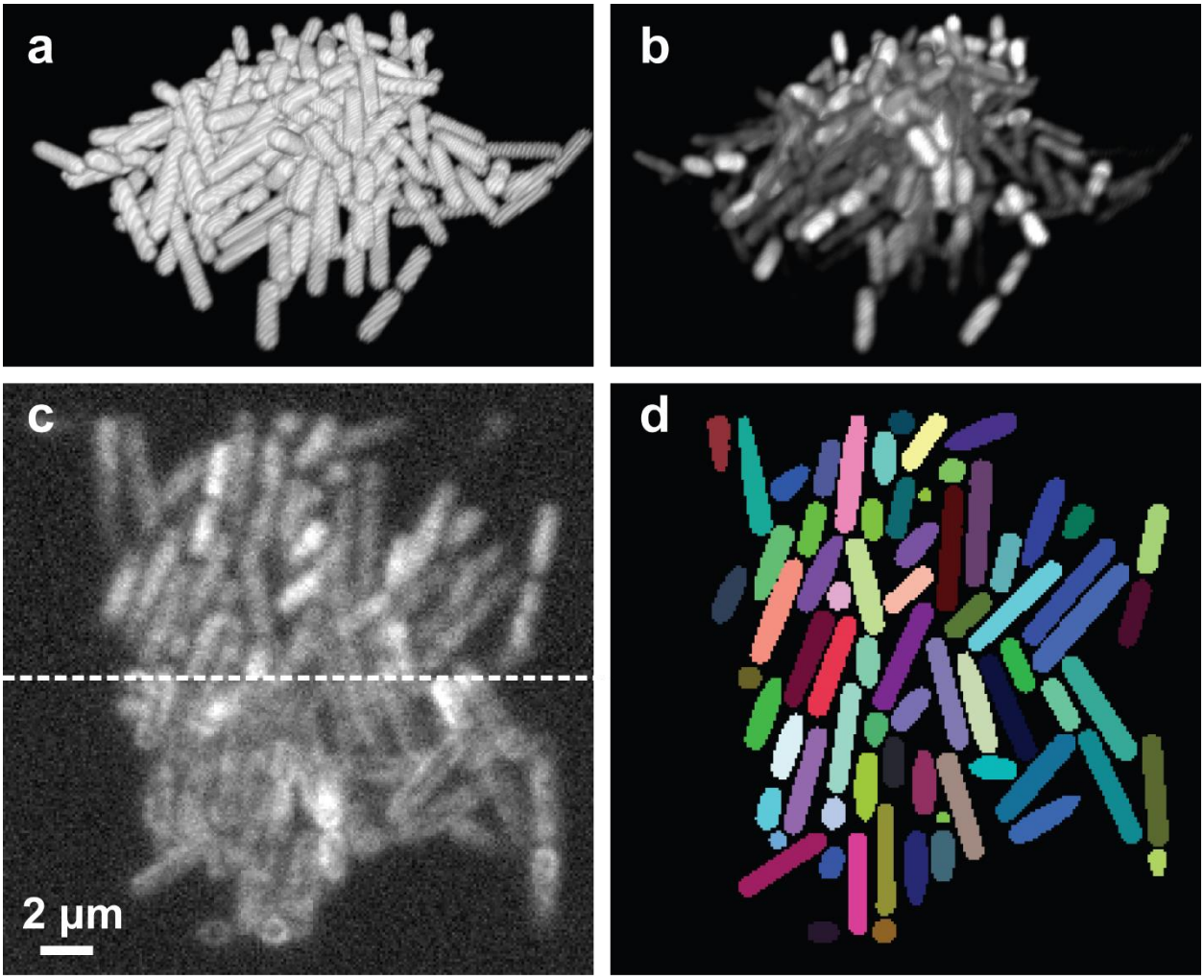

Figure 4.1. Simulation of fluorescent biofilms images and annotation maps used for CNN training. (a) Representative cell arrangements obtained by CellModeller. Due to the stochastic nature of biofilm growth, different cell arrangements are obtained in each new simulation. However, cell density is reproducible for each new simulated biofilm. (b) Simulated 3D fluorescence image based on the cell arrangements in (a). (c) XY slice through the 3D simulated fluorescence image in (b) (upper panel shows cells expressing cytosolic fluorescent proteins, lower panel shows cells stained with membrane-intercalating dyes). (d) Ground truth cell arrangements giving rise to the

image shown in c. Voxels are displayed as black (background), or in different colors (indicating different cells).

To mimic imaging of reporter gene expression in a subset of cells, we simulated biofilm images, in which all cells were stained at the cell surface (e.g., with a membrane intercalating fluorescent dye) and a subset of cells additionally contained intracellular fluorophores (e.g., through the expression of an intracellular fluorescent protein) (**Figure 4.2a** and **b**). The mixing ratios between membrane-labelled, and membrane and interior labelled cells were 10:90, 30:70, 50:50, 70:30 and 90:10. Ten different cell arrangements containing ~300 cells were simulated for each ratio. To train the CNNs (see next section), six datasets were used, all with a 50:50 mixing ratio.

To mimic imaging of cells with different morphologies, we simulated biofilms containing spherical and rod-shaped cells **(Figure 4.2c** and **d**). Cell arrangements were first simulated using rod shaped cells and then a fraction of rod-shaped cells is replaced with spherical cells. The size of the rod-shaped cells is that of *E. coli* (~3 × 1 μm, length by diameter). The size of the spherical cells is that of *S. aureus* (~1 μm in diameter) [47]. Both cell types were labelled by intracellular fluorophores, as described above. The mixing ratios between rod-shaped and spherical cells were 10:90, 30:70, 50:50, 70:30 and 90:10. Ten different cell arrangements containing ~300 cells were simulated for each ratio. To train the CNNs (see next section), we picked one image from each mixing ratio for a total of five images.

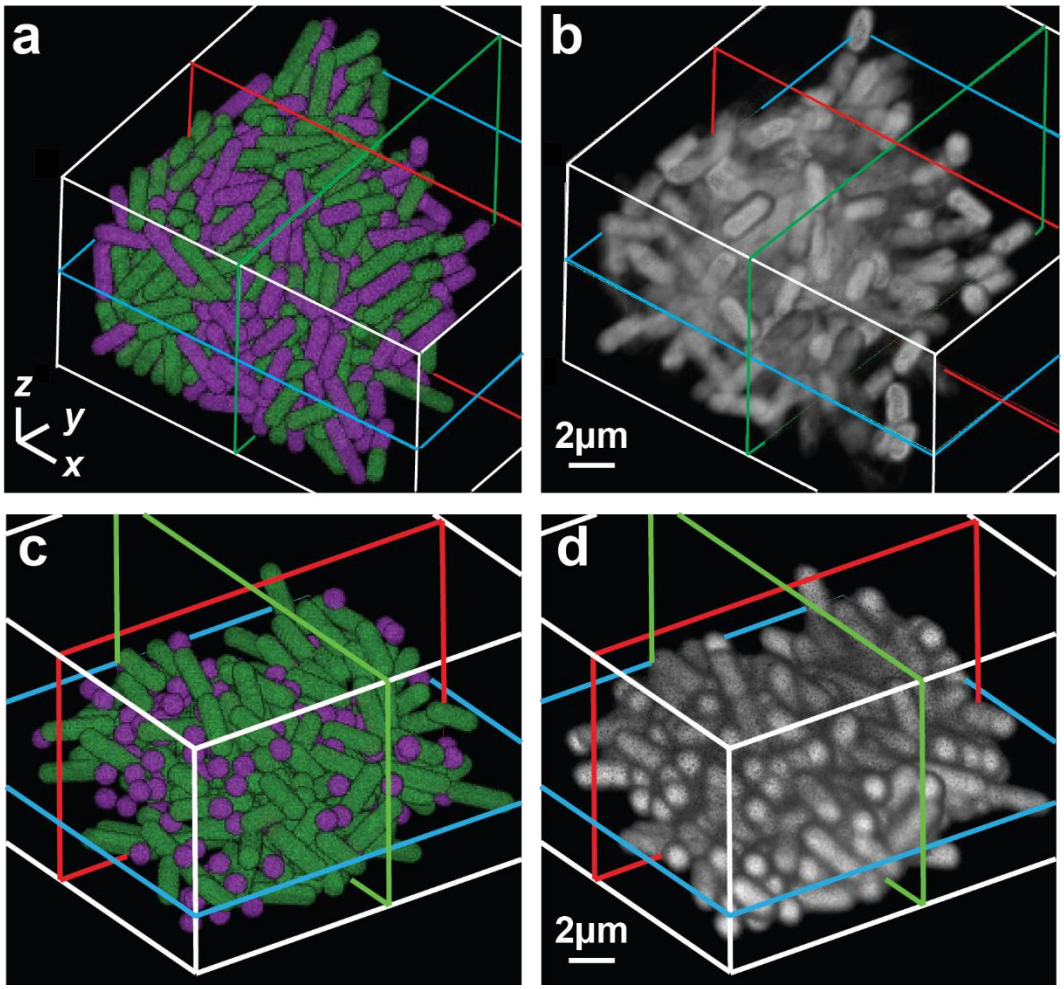

Figure 4.2 Simulation of mixed labeling and mixed cell shape biofilms. (a) Cell arrangements (green indicates membrane labeled cells, magenta indicates membrane labeled cells that simultaneously express interior fluorescence protein). (b) Simulated fluorescence image based on the cell arrangements in (a) as displayed by the volume viewer plugin of Fiji[40]. (c) Cell arrangements (green indicates rod-shaped cells, magenta indicates spherical shaped cells). (d) Simulated fluorescence image based on the cell arrangements in (c) as displayed by the volume viewer plugin of Fiji[40].

4.2.4 Training the convolutional neural networks

We trained 3D U-Net CNNs for voxel-level classification tasks[48] within the NiftyNet platform[49] (network architecture depth 4, convolution kernel size 3, ReLU activation function, 32 initial feature maps, and random dropout of 0.5 during training). To achieve robust performance, we trained these networks using five to ten simulated biofilm images with randomly selected cell densities and signal-to-background ratios (see 4.2.3 Generation of simulated biofilm images). The same raw data processing steps used for experimental data (see 4.2.2 Raw data processing) were also applied to simulated data. 3D deconvolved simulated data and their corresponding voxel-level annotations were used to train the CNNs. Each image used for training contained ~9 million voxels. We trained CNNs by classifying each voxel as 'background', 'cell interior' or as 'cell boundary' based on the underlying cell arrangements. For mixed-species biofilms, two additional classes, 'cell interior' and 'cell boundary' of the second species, were used. This type of annotation scheme has been shown to increase separation of bacterial cells in 2D[50]. For data augmentation, we applied NiftyNet's built-in scaling, rotation, and elastic deformation functions. Instead of the original cross-entropy loss function combined with uniform sampling, we used the Dice loss function and 'balanced sampler', so that every label has the same probability of occurrence in training. All networks were trained for 2000 to 3600 iterations with a learning rate of 0.0001. Using these parameters, it took approximately 24 hours to train the CNNs on a NVIDIA Tesla V100 GPU with 16 GB memory.

4.2.5 Thresholding of CNN-produced confidence maps

Voxel-level classification by CNNs generates different confidence maps (one confidence map for each annotation class). The confidence values range between 0 and 1 and represent the

confidence of assigning individual voxels to a given class. After thresholding the 'cell interior' confidence map to obtain a binary image (**Figure 4.3 a-c**), connected voxel clusters can be isolated and identified as single cell objects using 3D connected component labeling[51]. A conservative size-exclusion filter was applied: small objects with a volume ~10 times less than the expected cell size were considered background noise and filtered out using an area open operator[51]. Since the cell-interior volumes do not contain the cell boundaries, we dilated each object by 1-2 voxels to increase the cell volumes using standard morphological dilation[51]. The threshold value to segment individual cell objects based on the 'cell interior' confidence map was determined by plotting the overall voxel-level segmentation accuracy, quantified as the Intersection-over-Union value (IoU value, aka Jaccard index[52]) versus the confidence value thresholds (**Figure 4.3**). Optimal voxel-level segmentation accuracies were consistently obtained using confidence thresholds between 0.88 and 0.94. Throughout this work, we used 0.94 for cells labeled with intracellular fluorophores and 0.88 for cells labeled with membrane-localized fluorophores.

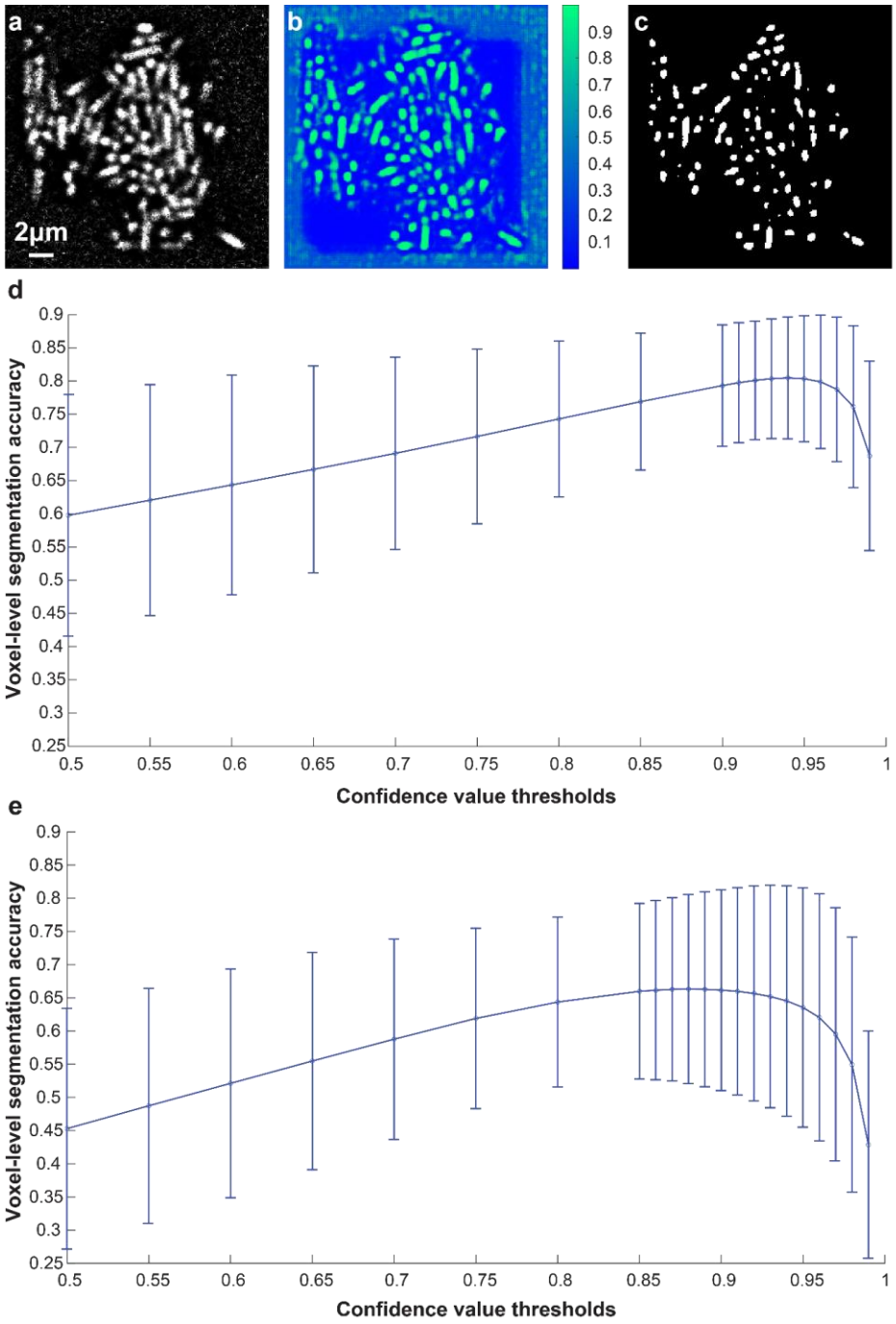

Figure 4.3 Binary segmentation result produced by thresholding the 'cell interior' confidence map at a high value (0.88-0.94). (a) Deconvolved fluorescence image. (b) 'Cell interior' confidence map. (c) Binary segmentation result (confidence threshold = 0.94). (d and e) Voxel-level segmentation accuracy (y axis) versus the confidence value thresholds (*x* axis) for cells labeled

with cytosolic fluorophores (d) and cells labeled with membrane-localized fluorophores (e). Each curve is plotted by averaging 500 different datasets. Error bars represent ± one standard deviation.

4.2.6 Post-processing of U-Net result using a refined LCuts algorithm

Thresholding of the 'cell interior' confidence map produces a binary segmentation result (background = 0, cell interior =1), where groups of connected, non-zero voxels identify individual cells in most cases (**Figure 4.3**). However, when cells are touching, they are often not segmented as individuals, but remain part of the same voxel cluster (undersegmentation). On the other hand, a single cell may be erroneously split into smaller subcellular objects (oversegmentation). Finally, in datasets with low SBR, connected voxel clusters may be detected that do not correspond to cells and thus produce false positive objects (**Figure 4.4a**). To address these errors and improve the segmentation accuracy further, we included additional mathematical image analysis steps to post-process the CNN results and reduce undersegmentation and oversegmentation errors.

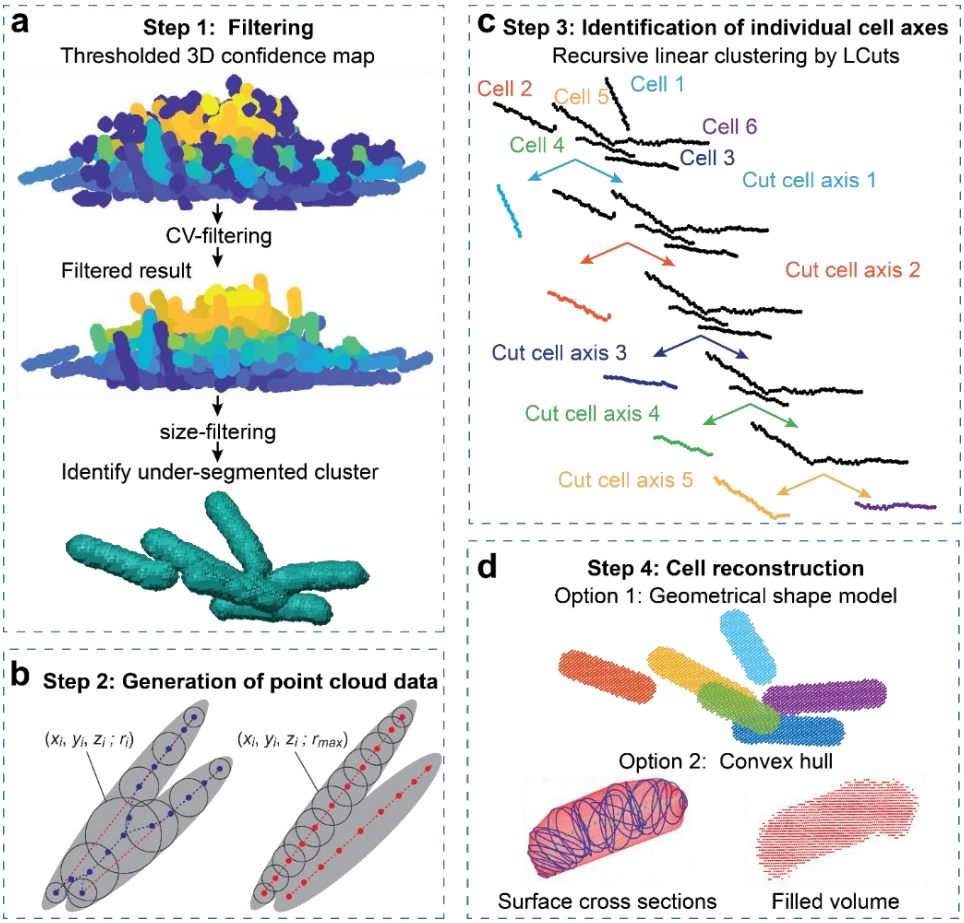

Figure 4.4 Post-processing of CNN-produced confidence maps using a refined *LCuts* processing pipeline. (a) False positive objects are detected and removed by CV- and size- filtering. Under-segmented clusters that are larger than single cells are selected for further splitting. (b) Illustration of modified medial axis (red dashed lines) extraction to generate point cloud data from fused clusters of rod-shaped cells using the method of inscribed spheres. When cells are touching, the traditional medial axis extraction process fails to align with the actual cell central axis (left). To overcome this drawback, we limited the size of the inscribed spheres based on prior knowledge of bacterial cell diameters (right). (c) The set of inscribed sphere centers are then treated as a fully-connected, undirected graph in 3D with two node features: location and direction (see text and **Figure 4.5** for details). The graph (blue nodes) is then iteratively cut into smaller graphs (red nodes) until the stopping criteria are reached (see text for details). (d) Post-processed graphs

represented in different color denoting different cells. The 3D surface of individual cells can be determined using a geometrical cell shape model (e.g., a spherocylinder for rod shaped bacteria) or by calculating the convex hull around the inscribed spheres found in step 2.

Step 1: False positive objects are identified by evaluating the coefficient of variation[53, 54] for each connected voxel cluster i:

$$CV_i = \frac{\sigma_i}{\mu_i}$$

where σ_i and μ_i denote the standard deviation and the mean of the intensity taken over all voxels contained in connected voxel cluster i. If the coefficient of variation is larger than ρ, then the current object will be classified as a false positive object and removed from the confidence map by setting all its voxels to zero. The removed objects will then no longer be counted when evaluating the cell counting accuracy. The value of ρ is selected based on the coefficient of variation of the background. For the datasets analyzed here, this sample coefficient of variation was determined to be ρ = 1.1. After CV-filtering, objects smaller than 25% of the expected bacterial cell size are also removed by setting its voxels to zero. The remaining connected voxel clusters are then considered for further processing (**Figure 4.4a**).

Step 2: To identify and delineate individual cells in the connected voxel clusters identified in the previous step, we implemented medial axis extraction using the method of inscribed spheres[55], with the constraint that the sphere radii do not exceed the expected diameter of a single bacterial cell (e.g. d = 0.8 μm) (**Figure 4.4b** left). The set of N inscribed spheres are tangent to the object's surface and parameterized by $(x_i, y_i, z_i; r_i<d/2)$ for i = 1, …, N. Determination of the $(x_i, y_i, z_i; r_i)$ coordinates is achieved using the Euclidean distance transform of the objects' boundary[56],

so that the points with coordinates (x_i, y_i, z_i) reliably trace out the central cell axes of individual bacterial cells (**Figure 4.4b** right).

Step 3: To separate different linear segments after cell axis extraction (**Figure 4.4c**), we used a refined version of the linear cuts (*LCuts*) algorithm[57, 58]. *LCuts* is a graph-based data clustering method designed to detect linearly oriented groups of points with certain properties. The fundamental elements of a weighted mathematical graph are nodes, edges, and edge weights. Here, the points with coordinates (x_i, y_i, z_i) represent the graph nodes. Edges are the connections among nodes. Edges are assigned weights, for example, to reflect the confidence that two nodes belong to the same group. *LCuts* achieves grouping by assigning weights to edges in the fully connected graph to reflect the similarity between two nodes. The features of each node include its location and direction, where the location of each node is simply its Cartesian coordinates. The direction of each node is found by first determining its 5-hop neighborhood, removing nodes at large relative angles, and evaluating the major direction of the outlier removed neighborhood (**Figure 4.5**).

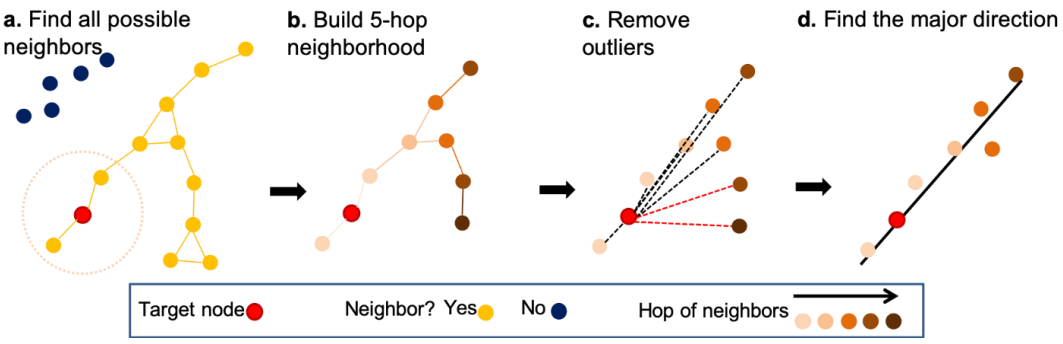

Figure 4.5 Determination of node direction in an outlier-removed neighborhood[57]. (a) A neighborhood of the target node (in red) is a sub-graph, where all adjacent nodes (in yellow) are connected via edges to the target node. Here, if the distance of two nodes is less than a chosen value (indicated by the dashed circle), these nodes are adjacent to each other. The blue dots are not part of the neighborhood. (b) A hop is defined as the number of edges that one has to traverse

from one node to the other node in the graph. Here, the 5-hop neighborhood of the target node is shown. (c) The directional vectors are found from the target node to all the other nodes within the 5-hop neighborhood (dashed lines). The nodes are classified as outliers if they have large relative angles compared to all the other directional vectors (red dashed lines). (d) Finally, the direction feature of the current node is evaluated as the major direction of the outlier removed neighborhood using principal component analysis.

The algorithm to separate the nodes into different groups is a recursive graph cutting method[57]. Graph cuts (*e.g.* nCut[59]) disconnect the edges between two groups of nodes when the combined weights of these edges are minimized. The weights, between node *i* and node *j*, are calculated as follows:

$$w_{ij} = w_D \cdot w_T \tag{4.1}$$

where

$$w_D = \begin{cases} e^{-D_{ij}^2/\sigma_D^2} & \text{if } D_{ij}^2 \le r \\ 0 & \text{if } D_{ij}^2 > r \end{cases} \tag{4.2}$$

$$w_T = e^{-\left(\cos(\theta_{ij})-1\right)^2/\sigma_T^2} \tag{4.3}$$

w_D weighs the distance between two nodes and w_T weighs difference between node directions. D_{ij} is the Euclidean distance between node *i* and node *j*, and r is set to eliminate edges between two far away nodes. θ_{ij} is the relative angle between the directions of nodes *i* and *j*. σ_D and σ_T are adjustable parameters that control the rate of exponential decay. *LCuts* continues to separate groups of nodes until each group satisfies a stopping criterion. The stopping criterion is

biologically inspired based on the expected length L of a single bacterial cell and a group's linearity after each recursion. *LCuts* yields linearly oriented groups of points that trace out the central axes of individual cells (**Figure 4.4c**). Importantly, cell separation is achieved without having to specify the number of cells in the biofilm in advance. Furthermore, to limit the need for optimization of postprocessing routines, the four adjustable parameters used in *LCuts*, namely cell diameter d, the cell length L, and the decay parameters σ_D and σ_T are chosen based on *a priori* knowledge about the bacterial cells under investigation. We found that the performance of *LCuts* is not sensitive to the particular values of d, L, σ_D and σ_T as long as they are consistent with the imaged bacterial cell sizes and shapes (**Figure 4.6**). Identification of single cells provided by *LCuts* alleviates under-segmentation errors of the CNN-based segmentation.

Step 4: The final output of linear clustering can provide length, location and orientation of each cell. Based on these linear clusters, the cellular architecture of the biofilms can be reconstructed by placing geometrical models of cells in space as shown in **Figure 4.4d**. For fast computation, spherocylinders are used as the geometrical model using a radius consistent with the known sizes of bacterial cells. To further refine the cell surfaces to better align with the CNN-segmented volumes, we enclosed the inscribed spheres found in Step 2 in a convex hull (**Figure 4.4d**).

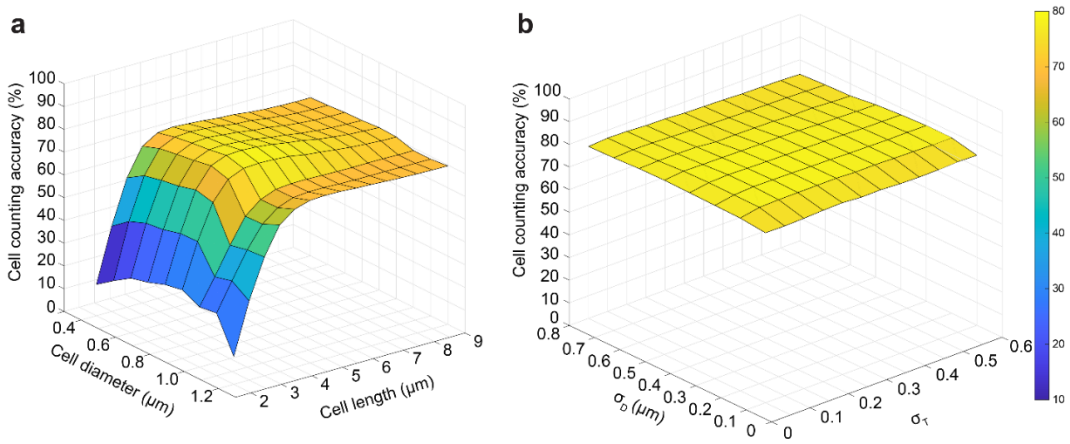

Figure 4.6 Validation of parameter selection for *LCuts* postprocessing by grid search. Shown is the cell counting accuracy averaged over 20 randomly chosen, simulated datasets of low SBR and/or high cell density, for which post-processing is required. (a) Average cell counting accuracy as a function of cell diameter $d \in [0.4, 1.2]$ μm and cell length $L \in [2, 9]$ μm at a fixed $\sigma_D = 0.5$ μm and $\sigma_T = 0.2$. (b) Average cell counting accuracy as a function of $\sigma_D \in [0.1, 0.8]$ μm, and $\sigma_T \in [0.05, 0.6]$ with fixed $(d, L) = (0.8, 4.5)$ μm. The cell counting accuracy is largely unaffected by variations in d, L, σ_D and σ_T and robustly remains above 70% for biologically reasonable parameter values, such as $d \sim 0.8$ μm, cell length $L \sim 6$ μm, for *E.coli*-like cell shapes. We also choose $\sigma_D = d/2$ and $\sigma_T = 0.2$, so that edges between nodes separated by more than a cells radius or with relative angles >30° are weighted down.

4.2.7 Performance Evaluation

We quantified segmentation accuracy both at the cell-level (object counting) and at the voxel-level (cell shape estimation). To quantify the cell-level segmentation accuracy, we designated segmented objects as true positive (*TP*) if their voxel overlap with the ground truth or the manual annotation resulted in an IoU value larger than a particular IoU matching threshold.

This criterion ensures one-to-one matching. A threshold of 0.5 is typically chosen when reporting single cell counting accuracy values[35, 60]. We follow this convention here. If the segmented cell object could not be matched to a ground truth/manually annotated cell volume, then it was counted as a false positive (*FP*) and the IoU value of that segmented object was set to zero. If a ground truth/manually annotated cell volume was not identified in the image, then it was counted as false negative (*FN*). The cell (object) counting accuracy was then defined as *TP*/(*TP*+*FP*+*FN*). The average IoU value over all segmented objects in the image quantifies the voxel-level segmentation accuracy, i.e. the accuracy of cell shape estimation.

To evaluate the accuracy of cell segmentation on experimental data, three researchers separately traced the cell contours on experimental 2D slices by using freehand selections in Fiji ROI Manger[40]. Because human annotation is very time consuming (about 50 hours for a complete 3D dataset containing ~300 cells in a 22 x 32 x 12 um^3 volume), one to three single 2D slices were selected for each dataset. One exception is the 3D *M. xanthus*, for which the cell outlines in all available x, y and z slices were traced manually (**Figure 4.7a**). For straight, rod-shaped cells, the centroids of the resulting 2D cell contours all fall within the cell interior volume. To group together the contours belonging to the same cells, the centroid of each contour was projected along the x, y and z dimension. If the projected centroid was enclosed by any other contour in a different slice, then the centroid of that contour was projected onto the plane of the initial contour. Two contours were labeled as related if they contained each other's projected centroids (**Figure 4.7b**). This process is repeated for all possible contour pairs and their relationship is recorded in an adjacency matrix. Next, related contours were assigned to individual cells (**Figure 4.7c**). To separate incorrectly grouped contours, we additionally identified clusters of centroids using the DBSCAN point clustering algorithm[61] (**Figure 4.7d**). In a final step, we manually removed incorrectly traced

contours (**Figure 4.7e**). Cells are reconstructed by creating convex hulls with the grouped contours (**Figure 4.7f** and **g**). This procedure determined the approximate positions, shapes, and orientations of individual cells in the 3D biofilm.

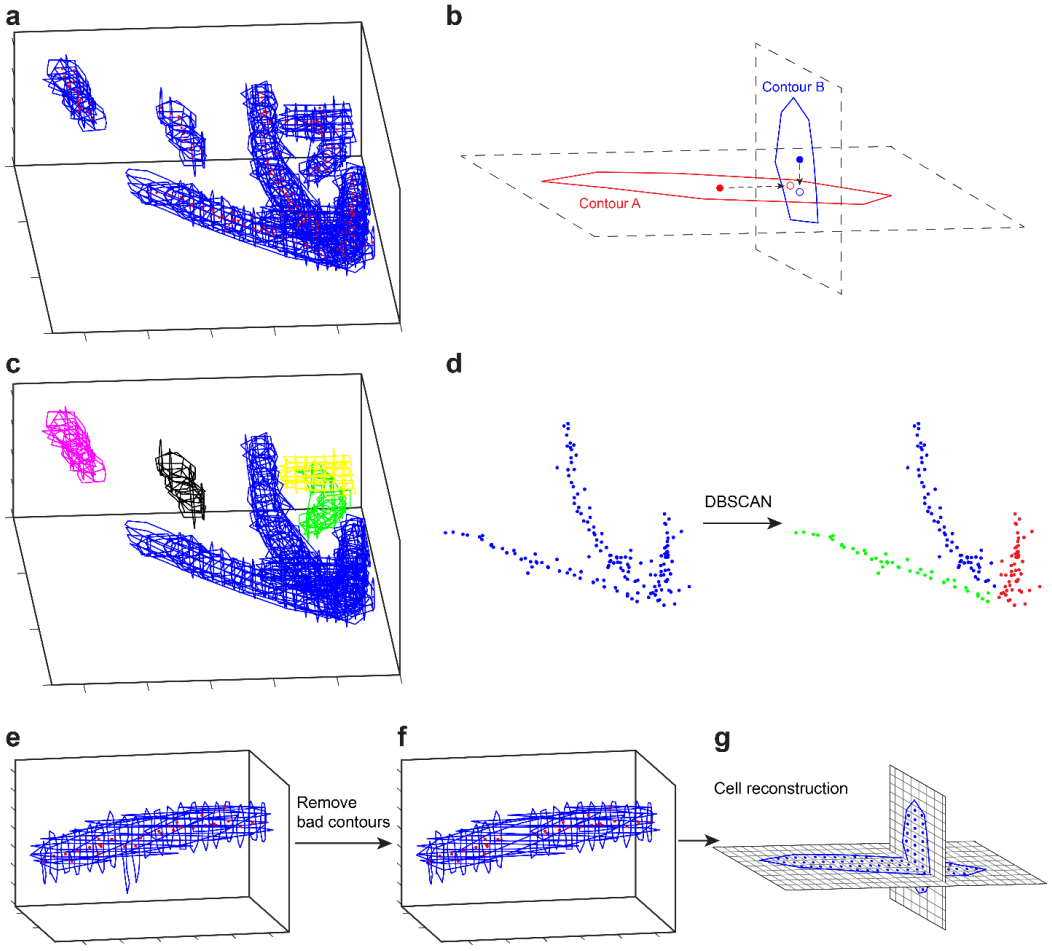

Figure 4.7 Manually trace cell outline. (a) Cell outlines in all available x, y and z slices were traced manually. (b) Find the contours belonging to the same cell. The centroid of each contour was projected along the x, y and z dimension. If the projected centroid was enclosed by any other contour in a different slice, then the centroid of that contour was projected onto the plane of the initial contour. Two contours were labeled as related if they contained each other's projected centroids. This process is repeated for all possible contour pairs and their relationship is recorded

in an adjacency matrix. (c) The related contours are grouped as cells. Different colors represent different cells. (d) Segment big clusters that contain more than one cell by grouping the centroids of the contours. This step will run manually and iteratively to segment all single cells from the big cluster. (e) Manually check all contours for each cell. (f) Remove the bad contours, such as unreasonably large ones. (g) A convex hull is built based on the contours for each cell. The convex hull is then used as the mask to extract cell volume from the raw data.

To estimate the SBRs of both simulated and experimental images, we manually selected and determined the intensities of approximately ten 'signal' and ten 'background' regions in the images. We computed the SBR as the mean signal intensity divided by the mean background intensity. To estimate the local density of a biofilm, we partitioned the image into several 3D tiles of size 64 by 64 by 8 voxels. We then estimated the local density as the total cell volume contained in each tile divided by the tile volume. We calculated the mean density of the 10 densest tiles to define the 'local density' metric reported for each dataset in the paper. To estimate the cell density in an experimentally acquired biofilm image, the same calculations were performed on either 3D manual annotations (if available) or binary masks obtained by CNN-processing.

4.3 Results and discussion

4.3.1 Cell segmentation by thresholding CNN confidence maps

CNNs have been shown to perform well on pixel-level classification tasks for both 2D and 3D data[62, 63]. Bacterial biofilms, however, present a unique challenge in this context. The cell shapes to be segmented are densely packed and barely resolvable even with the highest resolution optical microscopes. Additionally, living biofilms in fluorescence microscopes can only be imaged

with low laser intensities to ameliorate phototoxicity and photobleaching concerns. Unfortunately, low intensity fluorescence excitation also reduces the SBR in the acquired images. So far, it remains unclear to what extent single-cell segmentation approaches can accurately identify and delineate cell shapes in bacterial biofilm images obtained under low intensity illumination conditions. To address this question, we implemented an *in silico* CNN training strategy (4.2 Methods) and systematically evaluated its voxel-level classification (cell morphometry) and cell counting accuracies using simulated biofilm images with varying cell densities and SBRs similar to those encountered in experimental data.

We compared two commonly used cell labeling approaches, namely genetic labeling through the expression of cell-internal fluorescent proteins (**Figure 4.8a-c**) and staining of the cell membranes using fluorescent dyes (**Figure 4.8d-f**). For both labeling approaches, voxel-level segmentation and cell counting accuracies, obtained by thresholding CNN confidence maps, depend mostly on cell density, whereas the SBR plays a less important role. For cell-internal labeling, SBRs of >1.7 and cell densities of <60% consistently produce voxel-level classification accuracies of >80% and cell counting accuracies of >95%. On the other hand, SBRs of <1.7 and cell densities of >60% lead to lower segmentation accuracies. While lower segmentation accuracies are expected for higher cell densities and lower SBRs, the sharp drop-offs observed here may indicate a fundamental performance limitation of the CNNs employed. Still, the voxel-level classification and cell counting accuracies consistently surpass previous approaches for bacterial cell segmentation for commonly encountered cell densities and SBRs. Specifically, the cell counting accuracies obtained by Hartmann *et al.*[16], *Seg3D*[64], and Yan *et al.*[14] quickly drop to zero as a function of increasing IoU matching threshold, indicating that cell shapes are not accurately estimated by conventional image processing approaches (**Figure 4.8g-i**). We also

evaluated the segmentation accuracy of *Cellpose*, a recently developed, CNN-based cellular segmentation algorithm[35]. The segmentation accuracy of *Cellpose* is comparable or superior to the best-performing conventional image processing approaches – a considerable achievement given that *Cellpose* was trained primarily on images of eukaryotic cells. However, being a pre-trained generalist model, the segmentation accuracy of *Cellpose* is lower than the accuracy achieved by the specialist *in silico*-trained CNNs of *BCM3D*, which were trained specifically for 3D bacterial biofilm segmentation. Overall, the cell counting accuracies obtained by *BCM3D* are higher than other methods and remain higher even for IoU matching thresholds larger than 0.5, indicating that cell shapes are more accurately estimated by the *in silico*-trained CNNs.

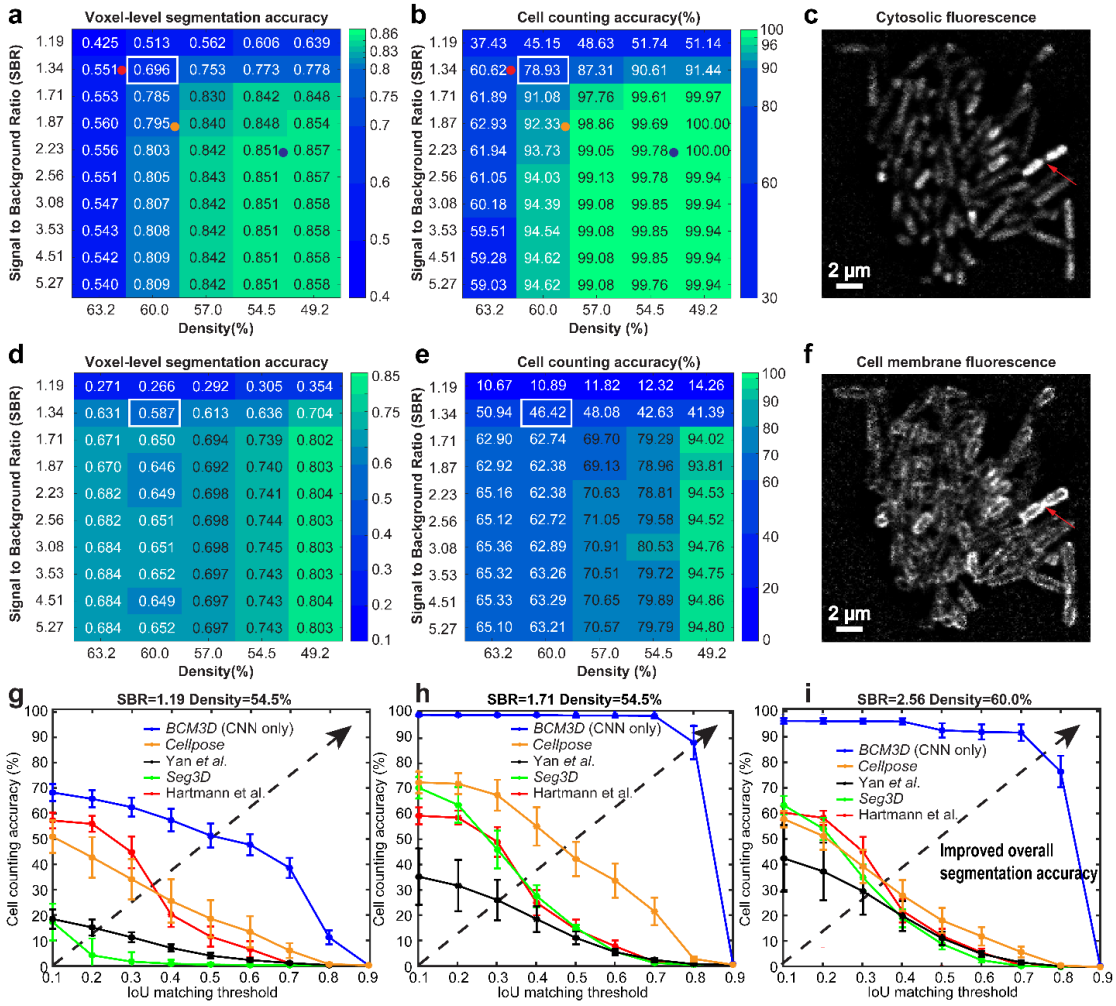

Figure 4.8 Performance of *BCM3D* using *in silico*-trained CNNs only on previously unseen simulated biofilm images. (a) The voxel-level segmentation accuracy quantifies whether each voxel has been assigned to the correct class ('cell interior', cell boundary', or 'background'). Solid circles represent the maximum local density and average SBRs encountered in experimental datasets (red, orange and blue: *E. coli* expressing GFP). (b) The cell counting accuracy (using an IoU matching threshold of 0.5 for each segmented object) averaged over n=10 replicate datasets for cells labeled with cytosolic fluorophores. (c) Example image of cells labeled with cytosolic fluorophores (Cell density = 60.0%, SBR = 1.34, indicated by white rectangle in panels a and b. Similar images were generated N = 10 times with different cell arrangements.) (d) Voxel-level

segmentation accuracy and (e) cell counting accuracy averaged over N=10 replicate datasets for cells labeled with membrane-localized fluorophores. (f) Example image of cells labeled with membrane-localized fluorophores (Cell density = 60.0%, SBR = 1.34, indicated by white rectangles in panels d and e. Similar images were generated N = 10 times with different cell arrangements.). The red arrows indicate a close cell-to-cell contact point. (g), (h) and (i) Comparison of segmentation accuracies achieved by conventional segmentation approaches (Hartmann *et al.*, *Seg3D*, Yan *et al.*), *Cellpose*, and *BCM3D* (only using *in silico*-trained CNNs). Three simulated datasets (cytosolic fluorophores) with different SBRs and cell densities are shown. Segmentation accuracy is parameterized in terms of cell counting accuracy (y axis) and IoU matching threshold (x axis, a measure of cell shape estimation accuracy). Each data point is the average of N = 10 independent biofilm images. Data are presented as mean values ± one standard deviation indicated by error bars. Curves approaching the upper right-hand corner indicate higher overall segmentation accuracy, as indicated by the dashed arrows.

The accuracies of single-cell shape estimation and cell counting are predominantly affected by cell density. The variation is more prominent for membrane-stained cells, because *inter*-cellular fluorescence intensity minima are less pronounced when cell membranes are labeled and cells physically contact each other (red arrow in **Figure 4.8c** and **f**). By contrast, intracellular fluorophores produce the highest intensities at the cell center, so that the gaps between cells are more readily resolvable. Also noteworthy is the sharp drop-off in segmentation accuracies for SBRs of <1.7 for all cases. In such low SBR regimes, fluorescence signals of the cells become too difficult to be distinguished from the background. As a result, the CNNs falsely identify random noisy patterns in the background as cells. Additionally, thresholding of the CNN confidence maps

often yields connected voxel clusters that contain multiple bacterial cells. False identification and incomplete delineation of cells cause the pronounced decrease in segmentation accuracy for SBRs of <1.7.

4.3.2 Post-processing of CNN confidence maps

To better identify individual cells in low SBR and high cell density datasets, we developed a graph-based post-processing module that takes advantage of the fact that bacterial cell shapes are highly conserved for a given species. Briefly, we transformed the CNN 'cell interior' confidence maps into 3D point cloud data that trace out the central axes of individual cells. This transformation was achieved by medial axis extraction using size-constrained inscribed spheres[55] (**Figure 4.4**). Single-cell axes are then identified as linearly clustered data points by *LCuts* – a graph-based data clustering method designed to detect linearly oriented groups of points[57]. The so-identified single-cell axes are then mapped back onto the original segmentation volumes to obtain estimates of the 3D positions, shapes, and orientations of the now separated cells.

Post-processing with *LCuts* takes advantage of *a priori* knowledge about expected bacterial cell sizes by removing erroneously segmented volumes that are significantly smaller than the expected value and by splitting incompletely segmented volumes representing fused cells. Improvements in cell counting accuracy of up to 15% and 36% are observed for cells labeled with cytosolic fluorophores (**Figure 4.9a-c**) and membrane-localized fluorophores (**Figure 4.9d-f**), respectively. The more substantial improvement for membrane-stained cells is due to fact that CNNs trained on membrane-stained cells are more prone to erroneously identifying speckled background noise as fluorescence signals in low SBR images. In addition, membrane-intercalating fluorophores of two adjacent cells are in close proximity, making it difficult to resolve fluorescence

signals from two separate cells due to spatial signal overlap (see the red arrow, **Figure 4.8c** and **f**). *LCuts* thus provides an important benefit in improving the cell counting accuracy to an extent not achieved by currently available thresholding- or watershed-based post-processing algorithms (**Figure 4.10**).

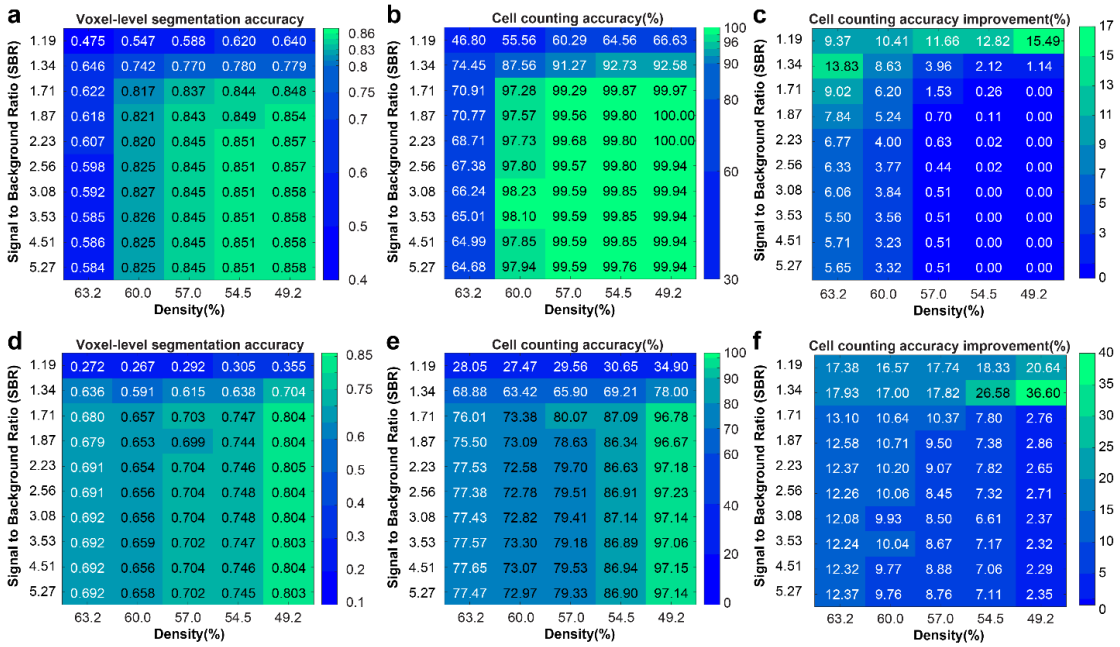

Figure 4.9 Performance of *BCM3D* (*in silico*-trained CNNs and additional post-processing by *LCuts*) on previously unseen simulated data. (a) Voxel-level segmentation accuracy and (b) cell counting accuracy (using an IoU matching threshold of 0.5 for each segmented object) averaged over N=10 replicate datasets for cells labeled with cytosolic fluorophores. (c) Improvement relative to *silico*-trained convolutional neural networks without post-processing. (d) Voxel-level segmentation accuracy and (e) cell counting accuracy averaged over N=10 replicate datasets for cells labeled with membrane-localized fluorophores. (f) Improvements relative to *silico*-trained convolutional neural networks without post-processing.

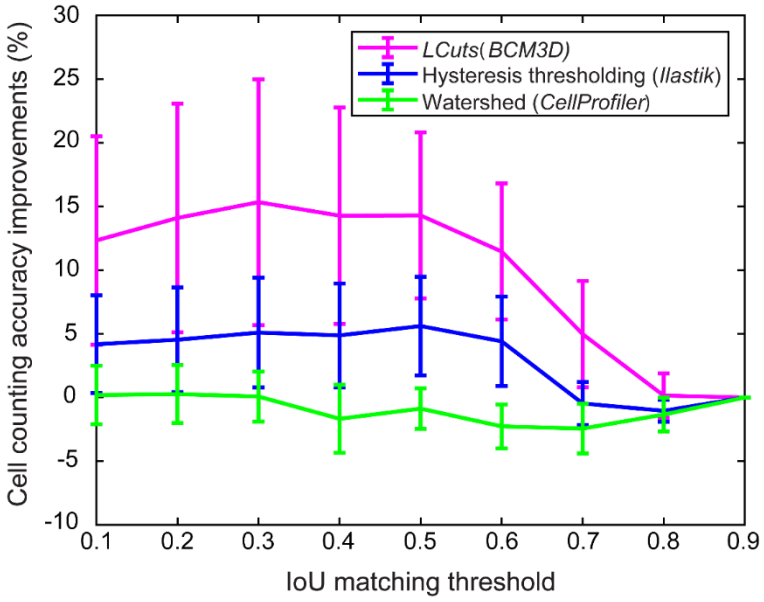

Figure 4.10 Comparison of *LCuts* to commonly used image post-processing methods. Shown is the cell counting accuracy averaged over 20 randomly chosen, simulated datasets of low SBR and/or high cell density, for which post-processing is required. The hysteresis thresholding-based algorithm of *Ilastik*[65] improves the cell counting accuracy by less than 6% on average for IoU matching thresholds less than 0.6. On the other hand, the watershed-based pipeline used by *CellProfiler*[66] provides negligible improvements and even decreases the average cell counting accuracy in many cases. This decrease is primarily due to oversegmentation. Among the three methods tested, *LCuts* provides the highest improvement in cell counting accuracy (>12% on average for IoU matching thresholds less than 0.6).

4.3.3 Segmentation of experimental biofilm images

To test the performance of *BCM3D* on experimentally acquired biofilm images, we acquired time-lapse images of GFP expressing *E. coli* biofilms every thirty minutes for ten hours. We then manually annotated one 2D slice in the 3D images at the t = 5, 6, and 10-hour time points. When referenced to these manual segmentation results, the *LCuts*-processed CNN outputs

consistently achieved better cell counting accuracies than conventional segmentation methods (**Figure 4.11, Figure 4.12**). Initially, *Cellpose* and the Hartmann *et al*. algorithm outperform the *in silico*-trained CNNs on two out of three of the test images (t = 360 and 600 min), for which our *in silico*-trained CNNs struggle with undersegmentation problems. However, mathematical post-processing of the CNN outputs by *LCuts* corrects some of these errors, so that the integrated *BCM3D* workflow achieves improved results compared to *Cellpose* and Hartmann *et al*. at each of the indicated time points. Visual inspection of the segmentation results is also informative. *Cellpose* accurately segments individual cells in low density regions, but suffers from oversegmentation errors in high density biofilm regions (**Figure 4.12e**). The Hartmann *et al*. algorithm provides reasonable estimates of cell positions in low and high density biofilm regions, but again struggles with cell shape estimation (**Figure 4.12d**). On the other hand, the integrated *BCM3D* workflow (CNN + *LCuts*) produces biologically reasonable cell shapes regardless of cell density (**Figure 4.11**).

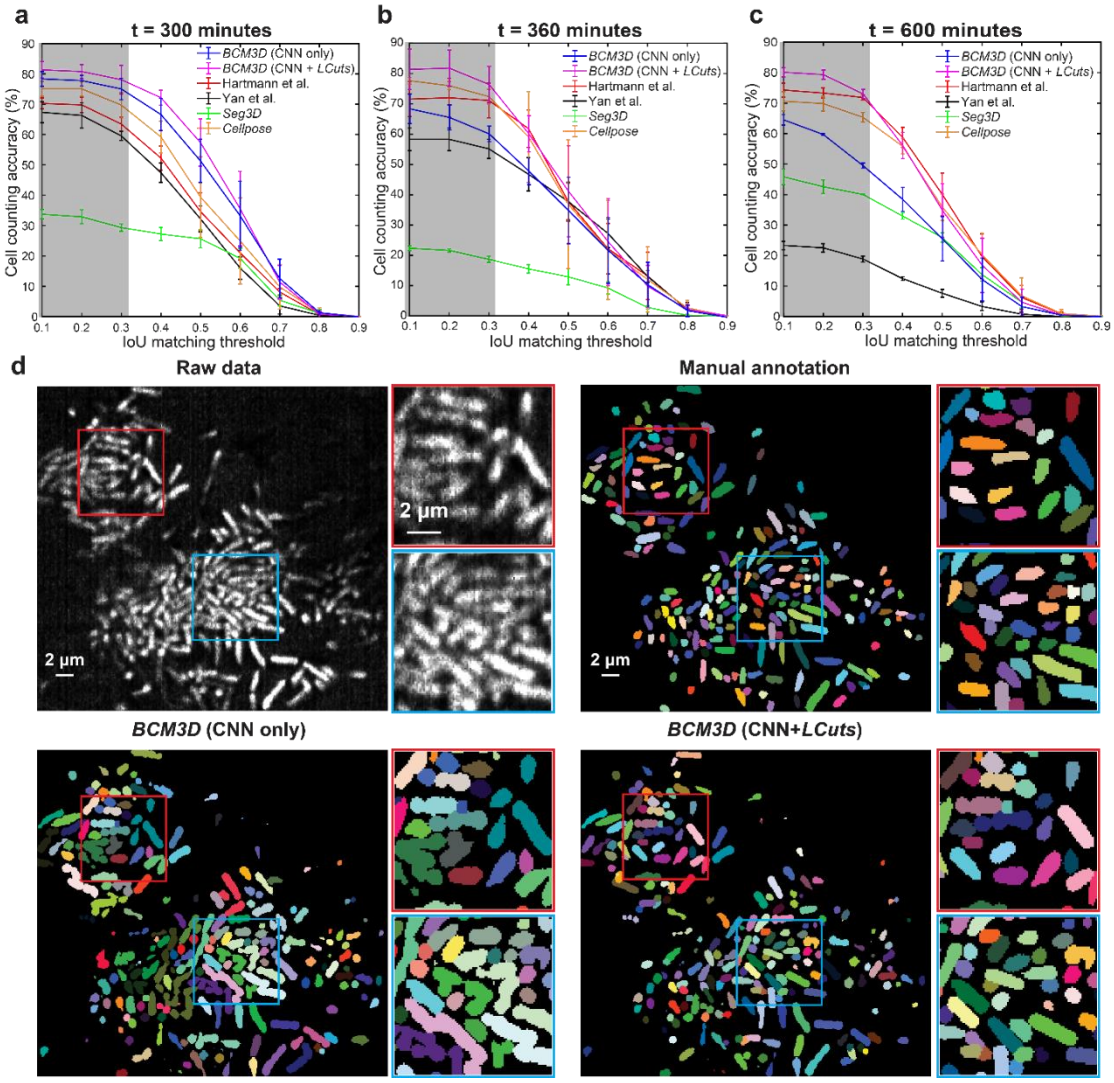

Figure 4.11 Comparison of segmentation accuracies achieved by conventional segmentation approaches (Hartmann *et al.*, *Seg3D*, Yan *et al.*), *Cellpose*, and *BCM3D*. The estimated SBRs are 2.2, 1.8, and 1.3, respectively. The estimated cell densities are 54.8%, 59.0%, and 64.6%, respectively. (a-c) Three experimental *E. coli* datasets (cytosolic expression of GFP) acquired at different time points after inoculation of cells. Segmentation accuracy is parameterized in terms of cell counting accuracy (*y* axis) and IoU matching threshold (*x* axis). Each data point is the average of the cell counting accuracies calculated using annotation maps traced by $N = 3$ different researchers. Data are presented as mean values ± one standard deviation indicated by error bars.

Curves approaching the upper right-hand corner indicate higher overall segmentation accuracy. (d) Comparison of segmentation results achieved at the t= 600 minutes time point by manual annotation (shown is one of $N = 3$ researchers' annotation result, the other two annotation results are shown in **Figure 4.12f** and **g**, and by BCM3D using *in silico*-trained CNNs only and after further refinement of CNN outputs using *LCuts*. Similar results were also obtained at the $t = 300$ and $t = 360$ minute time points. Segmentation results of the other methods are shown in **Figure 4.12**.

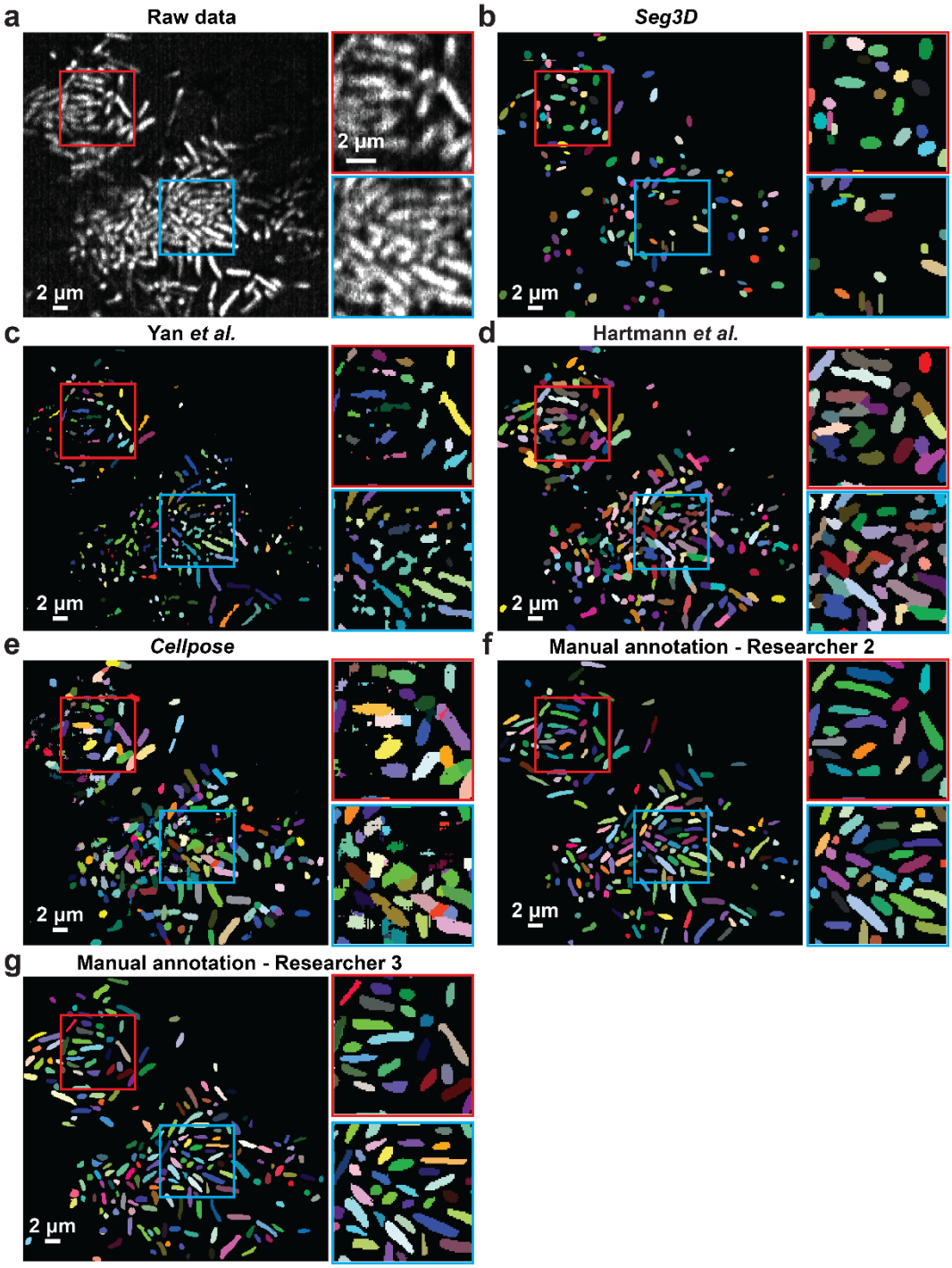

Figure 4.12 Visual comparison of segmentation results achieved by previous segmentation approaches. (a) Experimental dataset is the *E. coli* biofilm containing GFP expressing cells 600 mins after the inoculation. (b) Segmentation result obtained using *Seg3D*[64]. (c) Segmentation result obtained using the algorithm in Yan *et al.*[14]. (d) Segmentation result obtained using Hartmann *et*

al.[16]. (e) Segmentation result obtained using *Cellpose*[35]. (f) (g) manual annotation by two independent researchers.

We attribute the more rapid drop-off of the cell counting accuracy as a function of increasing IoU matching threshold in **Figure 4.11** to the following factors. First, human annotation of experimentally acquired biofilm images differs from the ground truth segmentation masks that are available for simulated data. The shape mismatches between algorithm segmented and manually annotated cell shapes (**Figure 4.13**) lead to a global lowering of voxel-level segmentation accuracy and thus a more rapid drop-off of the cell counting accuracy as a function of increasing IoU matching threshold. Because bacterial cell shapes are not accurately captured by manual annotation (**Figures 4.13**), cell counting accuracies referenced to manual annotations should be compared only at low IoU matching thresholds (0.1-0.3, shaded grey in **Figure 4.11a-c**), as also noted previously[60]. We also note that bacterial cells in experimental images appear motion-blurred if they are only partially immobilized and therefore wiggle during image acquisition. Furthermore, optical aberrations and scattering effects were not included in training data simulations, which may decrease the performance of the CNNs on experimental data. Still, at IoU matching threshold < 0.3, the cell counting accuracy of *BCM3D* remains above 75% while also producing biologically reasonable cell shapes. Thus, the bacterial cell segmentation results of *BCM3D* represent a substantial improvement over other approaches (**Figure 4.11** and **Figure 4.12)**.

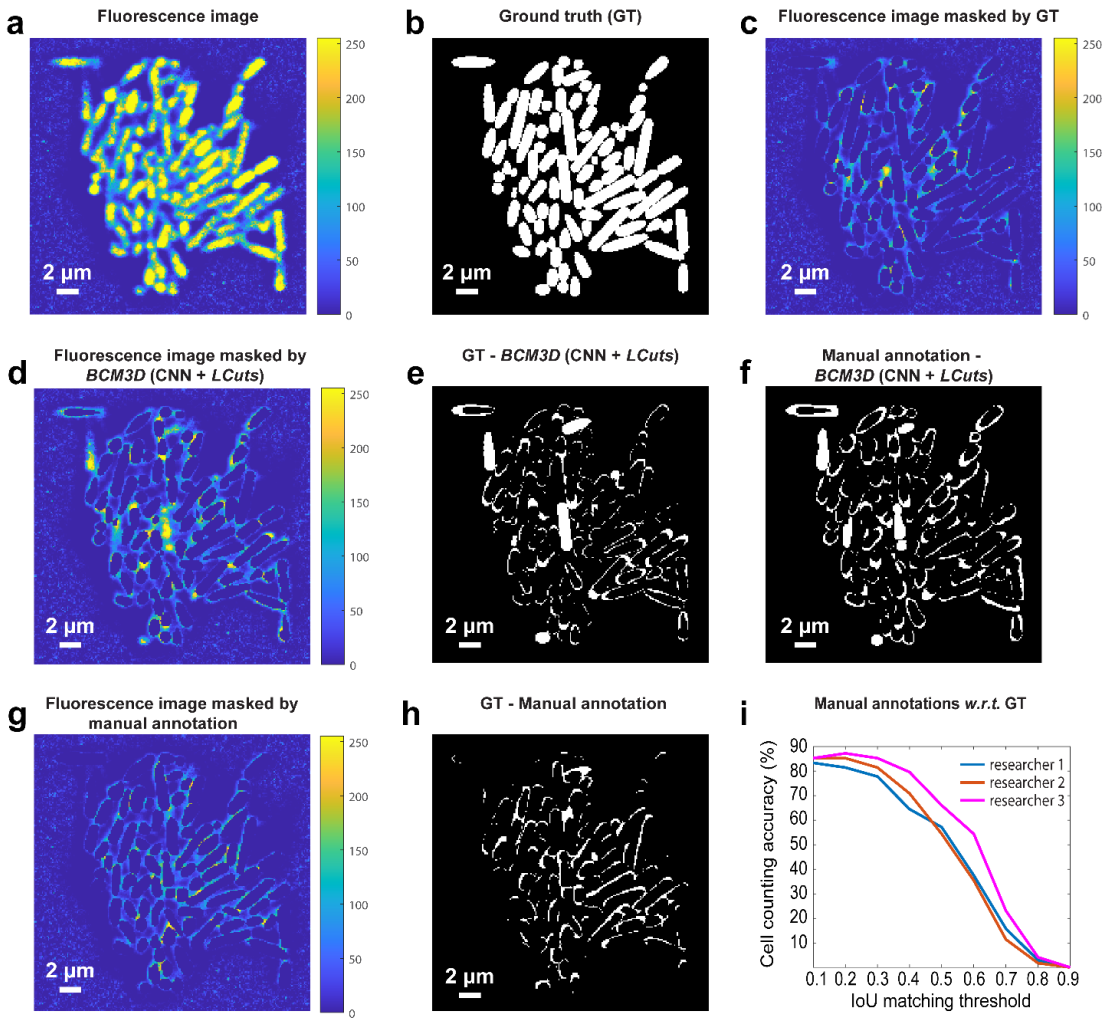

Figure 4.13 (a) Fluorescence image slice of a 3D simulated biofilm and (b) the corresponding ground truth [67]. (c) The fluorescence image slice shown in (a) masked by its corresponding GT shown in (b). The fluorescence is not completely masked because of the diffraction-limited resolution of light microscopy. (d) Fluorescence image slice of the same simulated biofilm masked by the *BCM3D* segmentation result. (e) Absolute value of the difference image between the GT and the *BCM3D* segmentation result. White pixels indicate regions where the two masks do not agree. (f) Absolute value of the difference image between a manual annotated mask (from researcher 3) and the *BCM3D* segmentation result. (g) Fluorescence image slice of the same simulated biofilm masked by the manual annotation result. Researcher 3 chose to draw larger cell

boundaries to mask more of the fluorescence intensity. (h) Absolute value of the difference image between the GT and the manually annotated mask. White pixels indicate regions where the two masks do not agree. (I) Segmentation accuracy achieved by manual annotation performed by three different researchers. Segmentation accuracy is parameterized in terms of cell counting accuracy (*y* axis) and IoU matching threshold (*x* axis, a measure of cell shape estimation accuracy. Curves approaching the upper right-hand corner indicate higher overall segmentation accuracy with respect to the ground truth. While IoU matching thresholds <0.3 yield good cell counting accuracies, the cell counting accuracy sharply decreases for IoU matching thresholds >0.3, because manually annotated cell shapes differ from the ground truth cell shapes.

To demonstrate that *BCM3D* can achieve similarly high segmentation accuracies for membrane-stained cells in different cellular arrangements, we analyzed a small patch of a *M. xanthus* biofilm, which was stained with the membrane intercalating dye FM4-64 (**Figure 4.14**). In contrast to *E. coli* biofilms, the submerged *M. xanthus* biofilm imaged here features cells in a mesh-like arrangement with close cell-to-cell contacts, which presents a unique challenge for 3D single-cell segmentation. To obtain reference data for 3D segmentation accuracy determination, we manually annotated each *xy*, *xz*, and *yz* slice of an entire 3D image stack (**Figure 4.14b**). When referenced to this 3D manual segmentation result, *BCM3D* (**Figure 4.14c**) produced cell counting accuracies above 70% at low (0.1-0.3) IoU matching thresholds, whereas segmentation results obtained by conventional image processing (Hartmann *et al.*) and by generalist CNN-processing (*Cellpose*) produced cell counting accuracies <50% in the same IoU matching threshold region (**Figure 4.14d**). We note however that neither *Cellpose* nor the Hartmann *et al.* algorithm was specifically optimized/designed for segmenting membrane-stained

cells. Indeed, the performance of *Cellpose* on this type of biofilm architecture is inferior to the results achieved using the *in silico*-trained CNNs of *BCM3D* alone (without using *LCuts* post-processing). One reason might be that the pre-trained, generalist *Cellpose* model has not been trained sufficiently on long, thin, and highly interlaced rod-shaped cells, such as those contained in a *M. xanthus* biofilm.

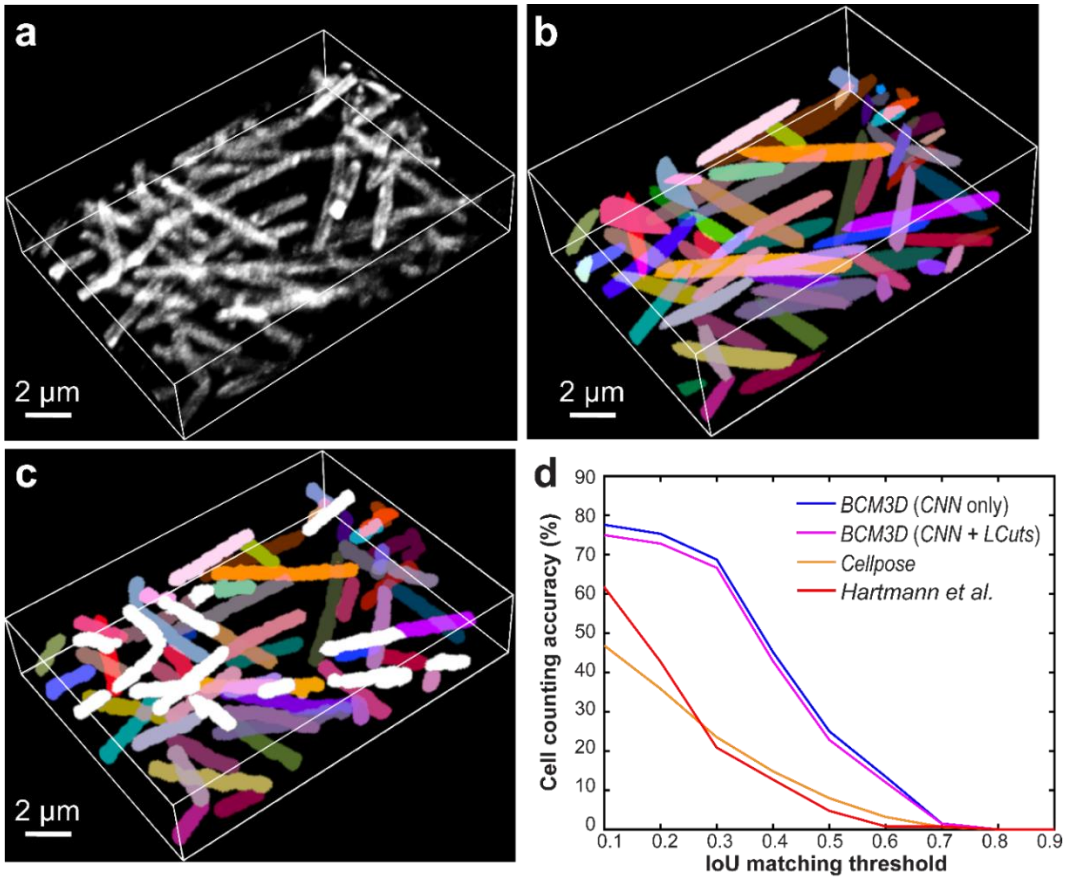

Figure 4.14 3D Segmentation accuracy evaluation using *M. xanthus* biofilm images (cell density = 36.2%, and SBR = 1.58) using *in silico*-trained CNN processing. (a) Maximum intensity projection of a 3D *M. xanthus* fluorescence image. Cells were labeled with membrane-intercalating dye, FM4-64. Similar images were obtained at N = 120 different time points. (b) Maximum intensity projection of the manually obtained 3D segmentation result. (c) Maximum intensity

projection of a CNN-based 3D segmentation result after *LCuts* post-processing. Cells that can be matched with the GT are displayed in the same colors as GT or otherwise colored in white. (d) Segmentation accuracy of compared algorithms parameterized in terms of cell counting accuracy (*y* axis) and IoU matching threshold (*x* axis).

4.3.4 Morphological separation of mixed cell populations

Given the improved segmentation results obtained using *BCM3D*, we reasoned that the same CNNs may have additional capacity to assign segmented objects to different cell types based on subtle morphological differences in the acquired images. Differences in the imaged cell morphologies arise due to physical differences in cell shapes (e.g., spherical vs. rod-shaped cells) or due to differences in the fluorescent labeling protocols (e.g., intracellular vs. cell membrane labeling), because fluorescence microscopes simply measure the spatial distributions of fluorophores in the sample. The ability to separate different cell morphologies is important for the study of multispecies biofilms, where interspecies cooperation and competition dictate population-level outcomes[4, 68-75]. Separation of differentially labeled cells is also important for the study of gene activation in response to cell-to-cell signaling[76]. Expression of cytosolic fluorescent proteins by transcriptional reporter strains is a widely-used technique to visualize activation of a specific gene or genetic pathway in living cells. Such genetic labeling approaches can be complemented by chemical labeling approaches, e.g. using membrane intercalating chemical dyes that help visualize cells non-specifically or environmentally-sensitive membrane dyes that provide physiological information, including membrane composition[77, 78], membrane organization and integrity[79-81], and membrane potential[82, 83]. Chemical and genetic labeling approaches are traditionally implemented in two different color channels. However, there are important drawbacks to using multiple colors. First and foremost, the amount of excitation light delivered is increased

by the necessity to excite differently colored fluorophores, raising phototoxicity and photobleaching concerns. Second, it takes *N* times as along to acquire *N*-color images (unless different color channels can be acquired simultaneously), making it challenging to achieve high temporal sampling in time-lapse acquisition. For these reasons, methods that extract complementary physiological information from a single-color image are preferable.

We evaluated the ability of *BCM3D* to automatically segment and identify rod-shaped and spherical bacterial cells consistent with shapes of *E. coli* and *S. aureus* in simulated images (**Figure 4.2cd**). To segment cells in two-population biofilms, we trained CNNs that classify pixels into five different classes: 'background', 'cell interior of population 1', 'cell boundary of population 1', 'cell interior of population 2' and 'cell boundary of population 2'. Thresholding the CNNs confidence maps can achieve cell counting accuracies larger than 90% for both cell types independent of their population fractions (**Figure 4.15a**). Post-processing of this result using *LCuts* improved the cell counting accuracy by less than 0.5% on average, indicating that under-segmented cell clusters are not prevalent in this dataset.

We next evaluated the ability of *BCM3D* to automatically segment and separate membrane-stained cells that express cytosolic fluorescent proteins from those that do not (**Figure 4.2ab**). Again, the cell counting accuracy is consistently above 80% for all tested mixing ratios (**Figure 4.15b**). Finally, we applied *BCM3D* to experimentally acquired biofilm images of two different *E. coli* strains. Both strains were stained by the membrane intercalating dye FM4-64, but the second strain additionally expressed GFP (**Figure 4.16**). The cells were homogeneously mixed prior to mounting to randomize the spatial distribution of different cell types in the biofilm (see 4.2.1 Imaging of bacterial biofilms with LLSM). Multiple 2D slices from the 3D image stack were manually annotated and compared with the results obtained by *BCM3D*. Consistent with the

single-species experimental data, a cell counting accuracy of 50% is achieved for each cell type at a 0.5 IoU matching threshold and, at lower IoU matching thresholds, the counting accuracies increased to 60% to 70%, (**Figure 4.15cd**). Thus, using appropriately trained CNNs in *BCM3D* enables automated and accurate cell type assignments based on subtle differences in cell morphologies in mixed population biofilms – a capability not available using conventional image processing methods.

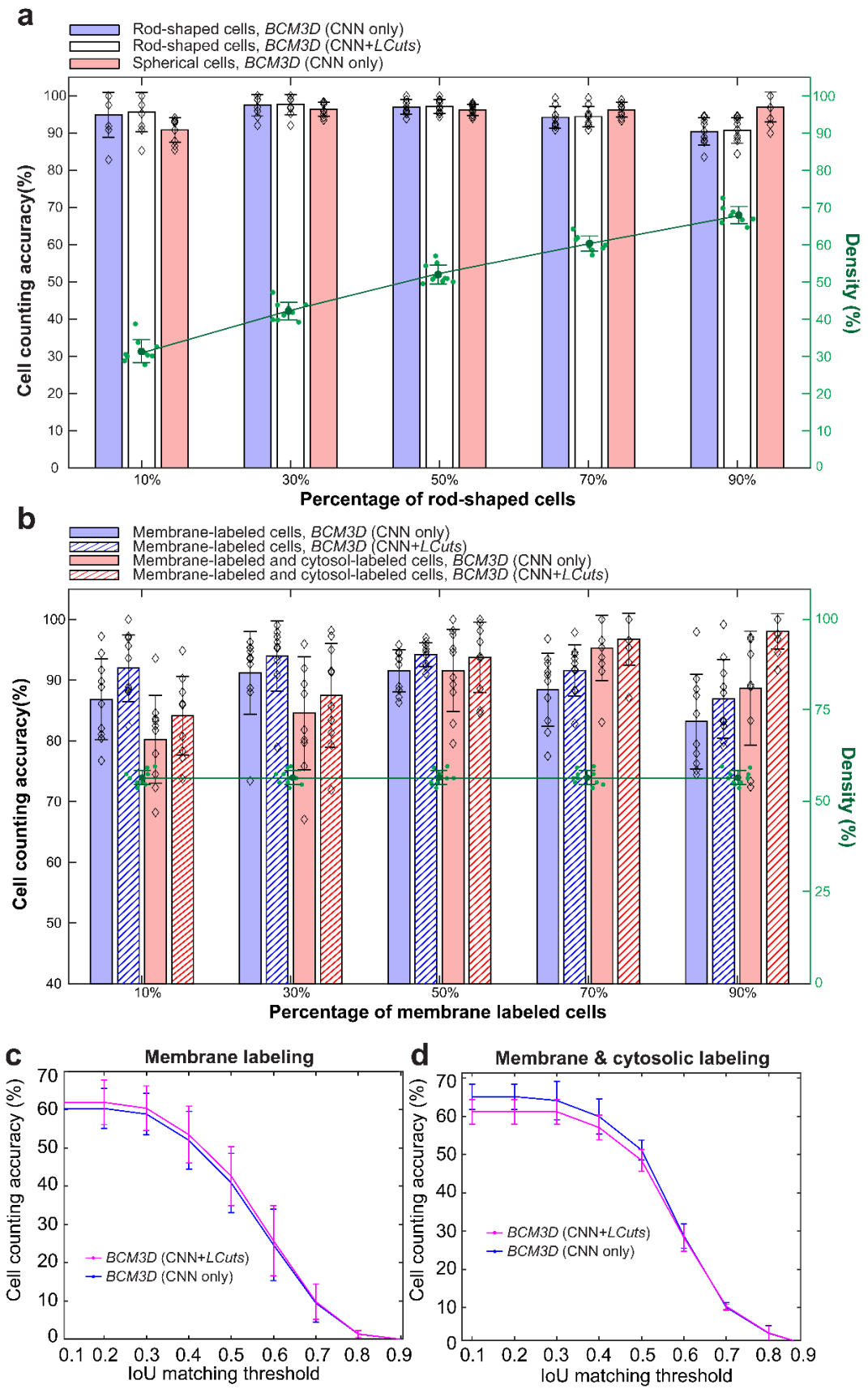
a
Rod-shaped cells, BCM3D (CNN only)
Rod-shaped cells, BCM3D (CNN+LCuts)
Spherical cells, BCM3D (CNN only)
Cell counting accuracy(%)
Density (%)
Percentage of rod-shaped cells
10%
30%
50%
70%
90%
b
Membrane-labeled cells, BCM3D (CNN only)
Membrane-labeled cells, BCM3D (CNN+LCuts)
Membrane-labeled and cytosol-labeled cells, BCM3D (CNN only)
Membrane-labeled and cytosol-labeled cells, BCM3D (CNN+LCuts)
Cell counting accuracy(%)
Density (%)
Percentage of membrane labeled cells
c
Membrane labeling
Cell counting accuracy (%)
BCM3D (CNN+LCuts)
BCM3D (CNN only)
IoU matching threshold
d
Membrane & cytosolic labeling
Cell counting accuracy (%)
BCM3D (CNN+LCuts)
BCM3D (CNN only)
IoU matching threshold

Figure 4.15 Performance of *BCM3D* on mixed-population biofilm images. (a) Cell counting accuracy of *BCM3D* on simulated images containing different ratios of rod-shaped and spherical cells. Black diamonds represent the counting accuracy for N = 10 independently simulated datasets. Green dots represent the cell density for each independent dataset. Error bars represent ± one standard deviation. (b) Cell counting accuracy of *BCM3D* on simulated images with different ratios of membrane-labeled, and membrane-labeled and interior fluorescent protein expressing cells. Black diamonds represent the counting accuracy for N = 10 independently simulated datasets. Green dots represent the cell density for N = 10 independent datasets. Error bars represent ± one standard deviation. (c and d) Cell counting accuracy of *BCM3D* on experimental images of (c) membrane-labeled, and (d) membrane-labeled and interior fluorescent protein expressing *E. coli* cells (mixing ratio ~ 1:1). Each data point is the average of the cell counting accuracies calculated using annotation maps traced by three different researchers (N = 3). Data are presented as mean values ± one standard deviation indicated by error bars.

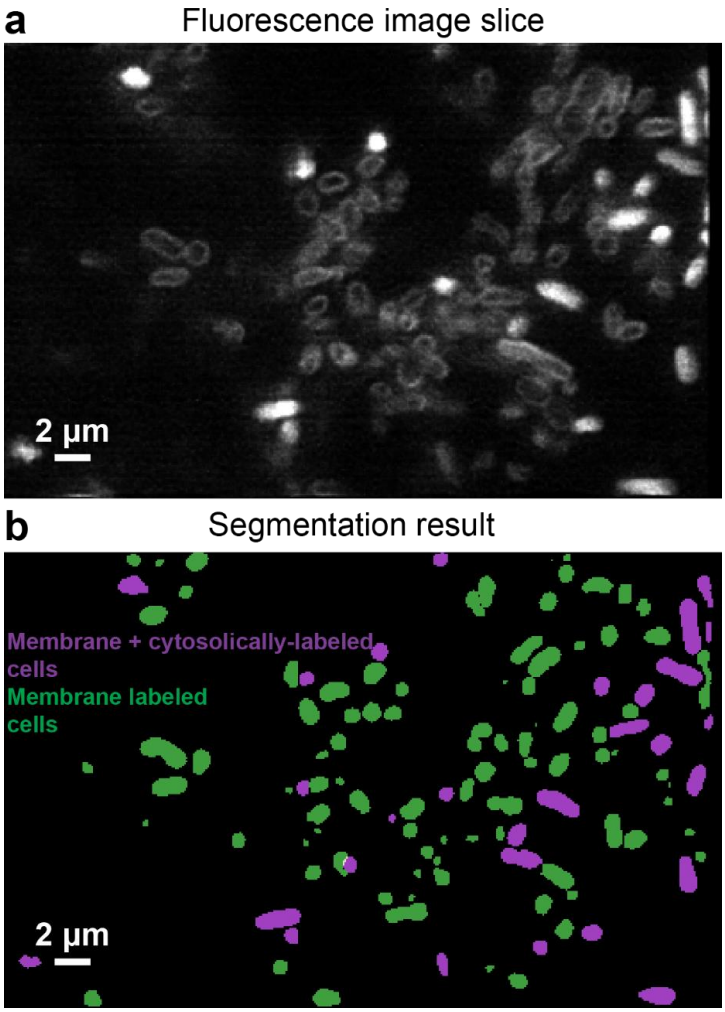

Figure 4.16 (a) Experimental 2D slice of a mixed *E. coli* population containing membrane-stained cells and membrane-stained cells that additionally express an intracellular fluorescent protein. The mixing ratio at the time of inoculation was 50:50. All cells were labeled by the FM4-64 membrane-intercalating dye. (b) *BCM3D* segmentation result corresponding to the image shown in (a). Membrane-stained cells are displayed in green, and cells that were both membrane-stained and cytosolically-labeled are displayed in magenta.

4.4 Conclusions

CNNs have been successful applied to many different problems in biological image analysis, but their ability to segment individual cells in 3D and time-lapse 3D bacterial biofilm images has not yet been fully explored. Here, we demonstrated a new CNN-based image analysis workflow, termed *BCM3D*, for single-cell segmentation and shape classification (morphometry) in 3D images of bacterial biofilms. In this work, we applied *BCM3D* to 3D images acquired by lattice light sheet microscopy. However, *BCM3D* readily generalizes to 3D images acquired by confocal microscopy or advanced super-resolution microscopy modalities, provided that realistic image formation models are used to simulate the training datasets. The use of simulated training data is a major advantage of *BCM3D*, because it overcomes inconsistencies inherent in manual dataset annotation (**Figure 4.13**) and thus solves the problem of obtaining sufficient amounts of accurately annotated 3D image data. The ability to use simulated training data provides needed flexibility not only in terms of the microscope platform used for imaging, but also in terms of the bacterial cell shapes that are to be segmented.

We systematically investigated the advantages and limitations of *BCM3D* by evaluating both voxel- and cell-level segmentation accuracies using simulated and experimental datasets of different cell densities and SBRs. *BCM3D* enabled accurate segmentation of individual cells in crowded environments and automatic assignments of individual cells to specific cell populations for most of the tested parameter space. Such capabilities are not readily available when using previously established segmentation methods that rely exclusively on conventional image and signal processing algorithms.

While *BCM3D* surpasses the performance of previous approaches, we stress that further improvements are possible and, for long-term, high frame-rate time-lapse imaging experiments,

absolutely needed. Our systematic analysis revealed that high cell density and low SBR datasets are particularly challenging for the CNNs used in this work. Future work will therefore focus on increasing the contrast and resolution in bacterial biofilm images. While, the use of optical super-resolution modalities can provide higher spatial resolution, such resolution improvements often come at a cost of reduced image contrast and faster photobleaching/phototoxicity. Software solutions that can process images with limited resolution and low SBRs will therefore play a tremendously important role in biological imaging. *BCM3D* is a general workflow that integrates computational simulation of training data, *in silico*-training of CNNs for a specific task or a specific cell type, and mathematical post-processing of the CNN outputs. Incorporating different training strategies and different CNNs, such as the generalist CNN used in *Cellpose*[35], into the *BCM3D* workflow will enable automated cross-validation of segmentation results when a ground truth or manual annotation map is not available. Furthermore, CNN-based image processing modules developed for contrast enhancement and denoising have also surpassed the performance of conventional methods based on mathematical signal processing[84-87]. Incorporating these tools into the *BCM3D* workflow promises to further improve the single-cell segmentation accuracies. We anticipate that the ability to accurately identify and delineate individual cells in dense 3D biofilms will enable accurate cell tracking over long periods of time. Detailed measurements of behavioral single-cell phenotypes in larger bacterial communities will help determine how macroscopic biofilm properties, such as its mechanical cohesion/adhesion and its biochemical metabolism, emerge from the collective actions of individual bacteria.

References

1. Zhang, M.; Zhang, J.; Wang, Y., et al., Non-invasive single-cell morphometry in living bacterial biofilms. *Nature communications* **2020,** *11* (1), 1-13.

2. Hall-Stoodley, L.; Costerton, J. W.; Stoodley, P., Bacterial biofilms: from the natural environment to infectious diseases. *Nat Rev Microbiol* **2004,** *2* (2), 95-108.

3. O'Toole, G.; Kaplan, H. B.; Kolter, R., Biofilm formation as microbial development. *Annual Review of Microbiology* **2000,** *54*, 49-79.

4. Nadell, C. D.; Drescher, K.; Foster, K. R., Spatial structure, cooperation and competition in biofilms. *Nat Rev Microbiol* **2016,** *14* (9), 589-600.

5. Persat, A.; Inclan, Y. F.; Engel, J. N., et al., Type IV pili mechanochemically regulate virulence factors in Pseudomonas aeruginosa. *Proc Natl Acad Sci U S A* **2015,** *112* (24), 7563-8.

6. Zhang, Q.; Lambert, G.; Liao, D., et al., Acceleration of Emergence of Bacterial Antibiotic Resistance in Connected Microenvironments. *Science* **2011,** *333* (6050), 1764-1767.

7. Donlan, R. M., Biofilms: microbial life on surfaces. *Emerg Infect Dis* **2002,** *8* (9), 881-90.

8. Yan, J.; Bassler, B. L., Surviving as a Community: Antibiotic Tolerance and Persistence in Bacterial Biofilms. *Cell host & microbe* **2019,** *26* (1), 15-21.

9. Kovach, K.; Davis-Fields, M.; Irie, Y., et al., Evolutionary adaptations of biofilms infecting cystic fibrosis lungs promote mechanical toughness by adjusting polysaccharide production. *NPJ Biofilms Microbiomes* **2017,** *3*, 1.

10. Vidakovic, L.; Singh, P. K.; Hartmann, R., et al., Dynamic biofilm architecture confers individual and collective mechanisms of viral protection. *Nat Microbiol* **2018,** *3* (1), 26-31.

11. Berk, V.; Fong, J. C. N.; Dempsey, G. T., et al., Molecular Architecture and Assembly Principles of Vibrio cholerae Biofilms. *Science* **2012,** *337* (6091), 236-239.

12. Stewart, E. J.; Ganesan, M.; Younger, J. G., et al., Artificial biofilms establish the role of matrix interactions in staphylococcal biofilm assembly and disassembly. *Sci Rep* **2015,** *5*, 13081.

13. Stewart, E. J.; Satorius, A. E.; Younger, J. G., et al., Role of environmental and antibiotic stress on Staphylococcus epidermidis biofilm microstructure. *Langmuir* **2013,** *29* (23), 7017-24.

14. Yan, J.; Sharo, A. G.; Stone, H. A., et al., Vibrio cholerae biofilm growth program and architecture revealed by single-cell live imaging. *Proc Natl Acad Sci U S A* **2016,** *113* (36), E5337-43.

15. Drescher, K.; Dunkel, J.; Nadell, C. D., et al., Architectural transitions in Vibrio cholerae biofilms at single-cell resolution. *Proceedings of the National Academy of Sciences* **2016,** *113* (14), E2066-E2072.

16. Hartmann, R.; Singh, P. K.; Pearce, P., et al., Emergence of three-dimensional order and structure in growing biofilms. *Nature Physics* **2019,** *15* (3), 251-256.

17. Gregor, I.; Enderlein, J., Image scanning microscopy. *Curr Opin Chem Biol* **2019,** *51*, 74-83.

18. Waldchen, S.; Lehmann, J.; Klein, T., et al., Light-induced cell damage in live-cell super-resolution microscopy. *Sci Rep* **2015,** *5*, 15348.

19. Chen, B.-C.; Legant, W. R.; Wang, K., et al., Lattice light-sheet microscopy: imaging molecules to embryos at high spatiotemporal resolution. *Science* **2014,** *346* (6208).

20. Li, D.; Shao, L.; Chen, B. C., et al., Extended-resolution structured illumination imaging of endocytic and cytoskeletal dynamics. *Science* **2015,** *349* (6251), aab3500.

21. Nadell, C. D.; Ricaurte, D.; Yan, J., et al., Flow environment and matrix structure interact to determine spatial competition in Pseudomonas aeruginosa biofilms. *Elife* **2017,** *6*.

22. Diaz-Pascual, F.; Hartmann, R.; Lempp, M., et al., Breakdown of Vibrio cholerae biofilm architecture induced by antibiotics disrupts community barrier function. *Nat Microbiol* **2019**.

23. Chang, B. J.; Kittisopikul, M.; Dean, K. M., et al., Universal light-sheet generation with field synthesis. *Nat Methods* **2019,** *16* (3), 235-238.

24. Dean, K. M.; Roudot, P.; Welf, E. S., et al., Deconvolution-free Subcellular Imaging with Axially Swept Light Sheet Microscopy. *Biophysical journal* **2015,** *108* (12), 2807-15.

25. Chakraborty, T.; Driscoll, M. K.; Jeffery, E., et al., Light-sheet microscopy of cleared tissues with isotropic, subcellular resolution. *Nat Methods* **2019,** *16* (11), 1109-1113.

26. Qin, B.; Fei, C.; Bridges, A. A., et al., Cell position fates and collective fountain flow in bacterial biofilms revealed by light-sheet microscopy. *Science* **2020**.

27. Wu, Y.; Wawrzusin, P.; Senseney, J., et al., Spatially isotropic four-dimensional imaging with dual-view plane illumination microscopy. *Nature biotechnology* **2013,** *31* (11), 1032-1038.

28. Dunsby, C., Optically sectioned imaging by oblique plane microscopy. *Optics Express* **2008,** *16* (25), 20306-20316.

29. Voleti, V.; Patel, K. B.; Li, W., et al., Real-time volumetric microscopy of in vivo dynamics and large-scale samples with SCAPE 2.0. *Nat Methods* **2019,** *16* (10), 1054-1062.

30. Flemming, H. C.; Wuertz, S., Bacteria and archaea on Earth and their abundance in biofilms. *Nat Rev Microbiol* **2019,** *17* (4), 247-260.

31. York, A. High NA single-objective light-sheet. https://andrewgyork.github.io/high_na_single_objective_lightsheet/.

32. Bouchard, M. B.; Voleti, V.; Mendes, C. S., et al., Swept confocally-aligned planar excitation (SCAPE) microscopy for high-speed volumetric imaging of behaving organisms. *Nature photonics* **2015,** *9* (2), 113.

33. Ulman, V.; Maska, M.; Magnusson, K. E. G., et al., An objective comparison of cell-tracking algorithms. *Nat Methods* **2017,** *14* (12), 1141-1152.

34. Source code available at: https://github.com/GahlmannLab/BCM3D.git.

35. Stringer, C.; Wang, T.; Michaelos, M., et al., Cellpose: a generalist algorithm for cellular segmentation. *Nature Methods* **2021,** *18* (1), 100-106.

36. Valm, A. M.; Cohen, S.; Legant, W. R., et al., Applying systems-level spectral imaging and analysis to reveal the organelle interactome. *Nature* **2017,** *546* (7656), 162.

37. Glass, D. S.; Riedel-Kruse, I. H., A synthetic bacterial cell-cell adhesion toolbox for programming multicellular morphologies and patterns. *Cell* **2018,** *174* (3), 649-658. e16.

38. Cotter, C. R.; Schuttler, H. B.; Igoshin, O. A., et al., Data-driven modeling reveals cell behaviors controlling self-organization during Myxococcus xanthus development. *Proc Natl Acad Sci U S A* **2017,** *114* (23), E4592-E4601.

39. Gao, R.; Asano, S. M.; Upadhyayula, S., et al., Cortical column and whole-brain imaging with molecular contrast and nanoscale resolution. *Science* **2019,** *363* (6424), eaau8302.

40. Schindelin, J.; Arganda-Carreras, I.; Frise, E., et al., Fiji: an open-source platform for biological-image analysis. *Nature methods* **2012,** *9* (7), 676-682.

41. Goddard, T. D.; Huang, C. C.; Meng, E. C., et al., UCSF ChimeraX: Meeting modern challenges in visualization and analysis. *Protein Sci* **2018,** *27* (1), 14-25.

42. Rudge, T. J.; Steiner, P. J.; Phillips, A., et al., Computational modeling of synthetic microbial biofilms. *ACS Synth Biol* **2012,** *1* (8), 345-52.

43. Reshes, G.; Vanounou, S.; Fishov, I., et al., Cell shape dynamics in Escherichia coli. *Biophysical journal* **2008,** *94* (1), 251-264.

44. Starruß, J.; Peruani, F.; Jakovljevic, V., et al., Pattern-formation mechanisms in motility mutants of Myxococcus xanthus. *Interface focus* **2012,** *2* (6), 774-785.

45. Harris, L. G.; Foster, S.; Richards, R. G., An introduction to Staphylococcus aureus, and techniques for identifying and quantifying S. aureus adhesins in relation to adhesion to biomaterials: review. *Eur Cell Mater* **2002,** *4* (3), 39-60.

46. Yan, T.; Richardson, C. J.; Zhang, M., et al., Computational correction of spatially variant optical aberrations in 3D single-molecule localization microscopy. *Optics Express* **2019,** *27* (9), 12582-12599.

47. Muller, F. D.; Schink, C. W.; Hoiczyk, E., et al., Spore formation in Myxococcus xanthus is tied to cytoskeleton functions and polysaccharide spore coat deposition. *Mol Microbiol* **2012,** *83* (3), 486-505.

48. Çiçek, Ö.; Abdulkadir, A.; Lienkamp, S. S., et al. In *3D U-Net: Learning Dense Volumetric Segmentation from Sparse Annotation*, Cham, Springer International Publishing: Cham, 2016; pp 424-432.

49. Gibson, E.; Li, W.; Sudre, C., et al., NiftyNet: a deep-learning platform for medical imaging. *Computer Methods and Programs in Biomedicine* **2018,** *158*, 113-122.

50. Van Valen, D. A.; Kudo, T.; Lane, K. M., et al., Deep Learning Automates the Quantitative Analysis of Individual Cells in Live-Cell Imaging Experiments. *PLoS Comput Biol* **2016,** *12* (11), e1005177.

51. Acton, S. T., Fast Algorithms for Area Morphology. *Digit Signal Process* **2001,** *11* (3), 187-203.

52. Jaccard, P., The distribution of the flora in the alpine zone. *New Phytologist* **1912,** *11* (2), 37-50.

53. Yu, Y.; Acton, S. T., Speckle reducing anisotropic diffusion. *Trans. Img. Proc.* **2002,** *11* (11), 1260-1270.

54. Tabassum, N.; Vaccari, A.; Acton, S., Speckle removal and change preservation by distance-driven anisotropic diffusion of synthetic aperture radar temporal stacks. *Digit Signal Process* **2018,** *74*, 43-55.

55. Choi, H. I.; Choi, S. W.; Moon, H. P., Mathematical theory of medial axis transform. *Pacific Journal of Mathematics* **1997,** *181* (1), 57-88.

56. Yan, T. Q.; Zhou, C. X., A Continuous Skeletonization Method Based on Distance Transform. *Comm Com Inf Sc* **2012,** *304*, 251-258.

57. Wang, J.; Batabyal, T.; Zhang, M. X., et al., LCuts: Linear Clustering of Bacteria Using Recursive Graph Cuts. *2019 IEEE International Conference on Image Processing (ICIP)* **2019**, 1575-1579.

58. Source code available at: https://github.com/jwang-c/Postprocessing-using-LCuts.

59. Shi, J. B.; Malik, J., Normalized cuts and image segmentation. *Ieee Transactions on Pattern Analysis and Machine Intelligence* **2000,** *22* (8), 888-905.

60. Weigert, M.; Schmidt, U.; Haase, R., et al. In *Star-convex Polyhedra for 3D Object Detection and Segmentation in Microscopy*, 2020 IEEE Winter Conference on Applications of Computer Vision (WACV), 1-5 March 2020; 2020; pp 3655-3662.

61. Ester, M.; Kriegel, H.-P.; Sander, J., et al., A density-based algorithm for discovering clusters a density-based algorithm for discovering clusters in large spatial databases with noise. In *Proceedings of the Second International Conference on Knowledge Discovery and Data Mining*, AAAI Press: Portland, Oregon, 1996; pp 226-231.

62. Moen, E.; Bannon, D.; Kudo, T., et al., Deep learning for cellular image analysis. *Nat Methods* **2019**.

63. Caicedo, J. C.; Roth, J.; Goodman, A., et al., Evaluation of Deep Learning Strategies for Nucleus Segmentation in Fluorescence Images. *Cytometry Part A* **2019,** *95* (9), 952-965.

64. Reyer, M. A.; McLean, E. L.; Chennakesavalu, S., et al., An Automated Image Analysis Method for Segmenting Fluorescent Bacteria in Three Dimensions. *Biochemistry-Us* **2018,** *57* (2), 209-215.

65. Berg, S.; Kutra, D.; Kroeger, T., et al., Ilastik: interactive machine learning for (bio) image analysis. *Nature Methods* **2019**, 1-7.

66. McQuin, C.; Goodman, A.; Chernyshev, V., et al., CellProfiler 3.0: Next-generation image processing for biology. *PLoS Biol* **2018,** *16* (7), e2005970.

67. Battin, T. J.; Besemer, K.; Bengtsson, M. M., et al., The ecology and biogeochemistry of stream biofilms. *Nature Reviews Microbiology* **2016,** *14* (4), 251-263.

68. Liu, J.; Prindle, A.; Humphries, J., et al., Metabolic co-dependence gives rise to collective oscillations within biofilms. *Nature* **2015,** *523* (7562), 550-4.

69. Prindle, A.; Liu, J.; Asally, M., et al., Ion channels enable electrical communication in bacterial communities. *Nature* **2015,** *527* (7576), 59-63.

70. Humphries, J.; Xiong, L.; Liu, J., et al., Species-Independent Attraction to Biofilms through Electrical Signaling. *Cell* **2017,** *168* (1-2), 200-209 e12.

71. Liu, J.; Martinez-Corral, R.; Prindle, A., et al., Coupling between distant biofilms and emergence of nutrient time-sharing. *Science* **2017,** *356* (6338), 638-642.

72. Mitri, S.; Foster, K. R., The genotypic view of social interactions in microbial communities. *Annu Rev Genet* **2013,** *47*, 247-73.

73. Drescher, K.; Nadell, C. D.; Stone, H. A., et al., Solutions to the public goods dilemma in bacterial biofilms. *Curr Biol* **2014,** *24* (1), 50-5.

74. Persat, A.; Nadell, C. D.; Kim, M. K., et al., The mechanical world of bacteria. *Cell* **2015,** *161* (5), 988-97.

75. Papenfort, K.; Bassler, B. L., Quorum sensing signal-response systems in Gram-negative bacteria. *Nat Rev Microbiol* **2016,** *14* (9), 576-88.

76. Kroos, L., Highly Signal-Responsive Gene Regulatory Network Governing Myxococcus Development. *Trends Genet* **2017,** *33* (1), 3-15.

77. Moon, S.; Yan, R.; Kenny, S. J., et al., Spectrally resolved, functional super-resolution microscopy reveals nanoscale compositional heterogeneity in live-cell membranes. *Journal of the American Chemical Society* **2017,** *139* (32), 10944-10947.

78. Bramkamp, M.; Lopez, D., Exploring the existence of lipid rafts in bacteria. *Microbiol. Mol. Biol. Rev.* **2015,** *79* (1), 81-100.

79. Zou, S. B.; Hersch, S. J.; Roy, H., et al., Loss of elongation factor P disrupts bacterial outer membrane integrity. *Journal of bacteriology* **2012,** *194* (2), 413-425.

80. Gonelimali, F. D.; Lin, J.; Miao, W., et al., Antimicrobial properties and mechanism of action of some plant extracts against food pathogens and spoilage microorganisms. *Frontiers in microbiology* **2018,** *9*, 1639.

81. Parasassi, T.; De Stasio, G.; d'Ubaldo, A., et al., Phase fluctuation in phospholipid membranes revealed by Laurdan fluorescence. *Biophysical journal* **1990,** *57* (6), 1179-1186.

82. Strahl, H.; Hamoen, L. W., Membrane potential is important for bacterial cell division. *Proceedings of the National Academy of Sciences* **2010,** *107* (27), 12281-12286.

83. Prindle, A.; Liu, J.; Asally, M., et al., Ion channels enable electrical communication in bacterial communities. *Nature* **2015,** *527* (7576), 59-63.

84. Weigert, M.; Schmidt, U.; Boothe, T., et al., Content-aware image restoration: pushing the limits of fluorescence microscopy. *Nature methods* **2018,** *15* (12), 1090-1097.

85. Krull, A.; Vičar, T.; Prakash, M., et al., Probabilistic noise2void: Unsupervised content-aware denoising. *Frontiers in Computer Science* **2020,** *2*, 5.

86. Krull, A.; Buchholz, T.-O.; Jug, F. In *Noise2void-learning denoising from single noisy images*, Proceedings of the IEEE Conference on Computer Vision and Pattern Recognition, 2019; pp 2129-2137.

87. Buchholz, T.-O.; Prakash, M.; Schmidt, D., et al. In *DenoiSeg: joint denoising and segmentation*, European Conference on Computer Vision, Springer: 2020; pp 324-337.

Chapter 5 *BCM3D 2.0*: Accurate segmentation of single bacterial cells in dense biofilms using computationally generated intermediate image representations

This chapter is adapted from Zhang, J., Wang, Y., et al. *bioRxiv.* **2021**[1].

5.1 Introduction

Most terrestrial bacteria live in 3-dimensional tissue-like communities, named biofilms, and as multicellular communities, bacteria can colonize various biotic and abiotic surfaces. Biofilm-dwelling bacteria interact intimately not only with each other and the surface they reside on, but also with a self-produced extracellular matrix (ECM) that consists of proteins, DNA, and polysaccharides[2-4]. The sum total of these interactions helps biofilms develop emergent capabilities beyond those of isolated cells[2, 3, 5, 6]. Most notably, biofilms are more tolerant towards physical, chemical, and biological stressors[6-8]. Understanding how such capabilities emerge from the cooperative or antagonistic behaviors among individual cells requires live-cell compatible imaging technologies that are capable of resolving and tracking single cells within dense 3D biofilms.

Recently developed light sheet-based fluorescence imaging modalities combine high resolution with fast imaging speed and low phototoxicity at levels that cannot be matched by confocal microscopy[9-11]. Light sheet-based microscopy modalities are therefore increasingly used for non-invasive time-lapse imaging of eukaryotic cells and tissues[12-14] as well as bacterial biofilms[15-17]. Depending on the type of biofilm, the cell density may however be too high to clearly resolve the gaps between cells given the diffraction-limited resolution of the microscope. Super-resolution imaging modalities, such as structured illumination microscopy[18, 19], improve the spatial resolution, but experimental improvements in spatial resolution always come at the cost of

decreased temporal resolution and increased light exposure to the specimen, which again raises photobleaching and phototoxicity concerns[20, 21]. An additional challenge arises for cell tracking studies. Tracking motile cells may require high frame rate imaging to achieve sufficient temporal resolution. Higher frame rates often need to be accompanied by a proportional decrease in excitation laser intensities to mitigate photobleaching and phototoxicity. The decreased excitation laser intensities then result in lower signal-to-background ratios (SBRs) in the individual images. The inherent trade-offs between spatial and temporal resolution, SBR, and photobleaching and phototoxicity is driving the continued development of new and improved image processing approaches that extract ever increasing amounts of useful information from the available experimental images.

Image processing pipelines based on supervised training of deep convolutional neural networks (CNNs) have been shown to outperform conventional image processing approaches for a variety of tasks in biomedical image analysis[22, 23]. For 3D biofilm image segmentation, we have recently developed Bacterial Cell Morphometry 3D (*BCM3D 1.0*), which achieved state-of-the-art performance for bacterial cell counting and cell shape estimation[24]. *BCM3D 1.0* does not rely on manually annotated training data, but instead combines *in silico*-trained CNNs for voxel classification with graph-theoretical linear clustering (mLCuts[25]) to post-process the thresholded CNNs outputs (i.e. the confidence maps for voxel-level classification). Using this approach, *BCM3D 1.0* automatically identifies individual cells in 3D images of 3D bacterial biofilms, reports their 3D shape and orientation, and classifies cell types with different morphologies. However, processing datasets with low SBRs and high cell densities remains challenging. Specifically, over- and under-segmentation errors increase in frequency for low SBR and high cell density datasets.

Cellpose[26] ,*StarDist*[27] and the work by Scherr *et al.*,[28] are CNN-based approaches that create intermediate image representations for better segmentation. We reasoned that solving an image-to-image translation task may prove to be a more robust strategy for handling extreme imaging conditions than the voxel classification approach implemented in *BCM3D 1.0* or, at least, yield complementary segmentation results to *BCM3D 1.0*. Two different intermediate image representations are generally employed. The first representation is used to locate objects and the second representation is used to highlight the boundaries of objects. In previous work[26-28], the CNN-predicted Euclidean distance to the nearest background pixel/voxel or the CNN-predicted object/background probability map was used to locate objects. Generation of boundary representations vary more widely: *StarDist* and *Cellpose* use star-convex polygons and spatial gradients separately to give complete boundaries, which can be used for object shape estimation. Scherr *et al.* instead enhance boundary regions that are close to other objects to prevent them from merging. Inspired by these approaches, we expanded the *BCM3D* workflow with a complementary CNN-based processing pipeline that translates the raw 3D fluorescence images into two distinct intermediate image representations that, in combination, are more amenable to conventional mathematical image processing, namely seeded watershed[29] and Otsu thresholding[30]. For object localization, we adapted the approach used by *StarDist*[27] and Scherr et al.[28]. For boundary information, however, we generated a new intermediate image representation that provides a complete 3D boundary of an object and additionally highlights whether the boundary is near other objects. We establish that, when combined and processed appropriately, these intermediate image representations provide biofilm segmentation results with higher accuracy than *BCM3D 1.0*. Importantly and in contrast to *BCM3D 1.0,* generation of intermediate image representations does not require image deconvolution as a pre-processing step. Deconvolution can lead to noise

amplification[31] that then leads to false positive segmentation objects with physiologically unreasonable shapes. We show that, using intermediate image representations, experimentally acquired biofilm images can be successfully segmented using CNNs trained with computationally simulated biofilm images – a feature that provides the flexibility to segment a wide variety of different cell shapes. Finally, we show that improvements in segmentation accuracy enables accurate multi-cell tracking, which is demonstrated using 3D simulated and experimental time-lapse biofilm images.

5.2 Methods

5.2.1 Lattice Light Sheet Microscope Imaging of Bacterial Biofilms

Fluorescence images of bacterial biofilms were acquired on a home-built lattice light sheet microscope (LLSM). LLSM enables specimen illumination with a thin light sheet derived from a 2D optical lattice[32, 33]; here, an intensity uniform light sheet was produced by dithering a square lattice. The average illumination intensity across the light sheet was less than 1 W/cm^2. The sub-micrometer thickness of the light sheet is maintained over a propagation distance of ~30 μm to achieve high resolution, high contrast imaging of 3D specimens comparable to confocal microscopy but with lower concomitant photobleaching and phototoxicity. Widefield fluorescence images of illuminated planes in the specimen are recorded on a sCMOS detector (Hamamatsu ORCA Flash v2). 3D biofilm images were acquired by translating the specimen through the light sheet in 200 nm step sizes using a piezo nano-positioning stage (Mad City Labs, NanoOP100HS). The data acquisition program is written in LabVIEW 2013 (National Instruments).

Kanamycin resistant *S. oneidensis* MR-1, constitutively expressing GFP, were cultured at 30 °C overnight in LB medium with 50 μg/ml Kanamycin. Overnight cultures were diluted 100 times into the same culture medium, grown to an optical density at 600 nm (OD600) of 0.4 – 1.0,

and then diluted to OD600 ~ 0.05 using M9 media with 0.05% (W/V) casamino acids. Poly-l-lysine coated round glass coverslips with the diameter of 5 mm were put into a 24-well plate (Falcon) and 400 μL of diluted cell culture was added to the well. Cells were allowed to settle to the bottom of the well and adhere to the coverslip for 1 hour. After the settling period, the coverslip was gently rinsed with M9 media to flush away unattached cells. Then 400 μL of M9 media (0.05% casamino acids) were added to ensure immersion of the coverslips. The well plate was set in a 30 °C chamber for 72-96 hours to allow dense biofilms to develop. Media were exchanged every 24 hours. Before imaging, the coverslip was rinsed again with fresh M9 media. The rinsed coverslip was then mounted onto a sample holder and placed into the LLSM sample-basin filled with M9 media. GFP was excited using 488 nm light sheet excitation. 3D biofilm stacks were acquired by translating the specimen through the light sheet in 200 nm or 235 nm steps. Each 2D slice was acquired with an exposure time of 5 ms or 10 ms.

Samples for time-lapse images were prepared by the same procedures, except imaging was started after either 24-hour or 48-hour cell attachment period, and the imaging experiment was carried out in LM medium (0.02% (W/V) yeast extract, 0.01% (W/V) peptone, 10 mM HEPES (pH 7.4), 10 mM $NaHCO_3$) with a lactate concentration of 0.5 mM.[34] Time-lapse images were recorded every 30 seconds for 15 minutes or 5 minutes for 5 hours for the two datasets shown in **Figure 5.8** with the same imaging parameters as detailed above.

5.2.2 Raw Data Processing

Raw 3D stacks were deskewed and rotated as described previously[35], but the deconvolution step was omitted. If necessary, background subtraction can be applied to reduce background signal. 3D images were rendered using the 3D Viewer plugin in Fiji[36] or ChimeraX[37]. Sample drift over the course of a time-lapse imaging experiment was corrected by Correct 3D Drift[38], a Fiji plug-in

that performs registration by phase correlation, a computationally efficient method to determine translational shifts between images at two different time points.

5.2.3 Generation of simulated biofilm images

Data for CNNs training was computationally generated as described previously[24]. Briefly, CellModeller[39], an individual-based computational model of biofilm growth, was used to simulate growth and division of individual rod-shaped cells in a population (**Figure 5.1a**). A minimum distance criterion between cells is imposed at each time point to alleviate cellular collisions that are due to cell growth. We chose cell diameter and cell length (d, l) parameters consistent with a given bacterial species, namely (1 μm, 3 μm) for *E. coli*[40], (0.7 μm, 6 μm) for *M. xanthus*[41], and (0.6 μm, 2 μm) for *S. oneidensis*[42]. 3D fluorescence intensity images (**Figure 5.1b**) were generated by convolving randomly positioned fluorophores in the cytoplasm or the membranes of simulated cells (**Figure 5.1cd**) with experimentally measured point spread functions (PSFs), and then adding experimentally measured background and noise (Poisson detection noise, based on the summed background and signal intensities, as well as Gaussian read noise, experimentally calibrated for our detector at 3.04 photons per pixel on average)[43].

The fluorescence signal intensity in the simulated images was adjusted to match the signal to background ratios (SBRs) of experimentally acquired data. To estimate the SBRs of both simulated and experimental images, we manually selected 10 ‘signal’ and 10 ‘background’ regions in the images. The SBR was calculated by dividing the mean background intensity by the mean signal intensity. To estimate the local density of a biofilm, the image was partitioned into several 3D tiles 64 by 64 by 8 voxels in size and the total cell volume contained in each tile was divided by the tile volume. The reported cell density was computed as the average of the 10 densest tiles for each dataset.

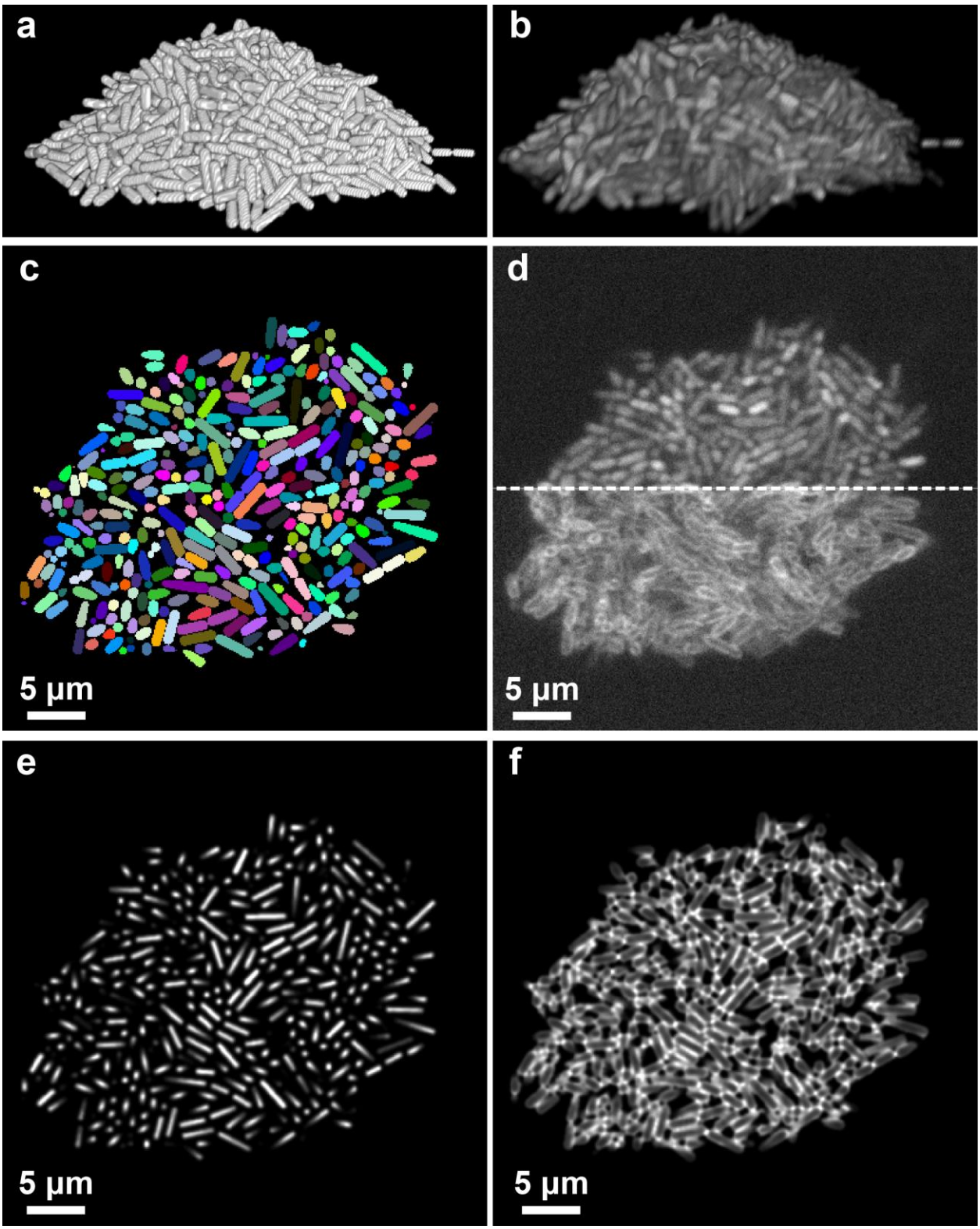
a
b
c
5 µm
d
5 µm
e
5 µm
f
5 µm

Figure 5.1 Simulation of fluorescent biofilms images and intermediate image representations. (a) Cell arrangements obtained by CellModeller. (b) Simulated 3D fluorescence image based on the cell arrangements in a. (c) Ground truth information of a 2D slice. Different cells are shown in different colors and intercellular spaces (background voxels) are displayed in black. (d) 2D slices of the simulated fluorescence image corresponding to the ground truth shown in c. The upper panel shows cells containing cytosolic fluorophores, the lower panel shows cells with fluorescently stained membranes. (e and f) Intermediate image representations generated from the ground truth information shown in c. See text for details.

5.2.4 Generation of intermediate image representations

To generate 'distance to nearest cell exterior' images (**Figure 5.1e**, **Figure 5.2**) from ground truth data (**Figure 5.2ab**), the Euclidean distance of each voxel inside a cell to the nearest voxel not belonging to that cell was calculated. The so-obtained distances were then normalized to the maximum value of that cell (**Figure 5.2c**). In order to obtain a steeper gradient in distance values, the distance values were additionally raised to the third power (**Figure 5.2d**), so that the resulting images show highly peaked intensity near the cell center. In a final step, the 'distance to nearest cell exterior' images were smoothed by Gaussian blurring (kernel size = 5 voxels in each dimension) (**Figure 5.2e**).

To help distinguish touching cells, we calculated a second image representation, the 'proximity enhanced cell boundary' image (**Figure 5.1f**, **Figure 5.2**). First, we subtracted the normalized distances to the nearest voxel not belonging to this cell (**Figure 5.2c**) from the binary map (**Figure 5.2b**). Second, we calculated the inverse of the Euclidean distance of each voxel inside a cell to the nearest voxel belonging to another cell, an intermediate image representation that has been proven useful to prevent objects merging in 2D[28] (**Figure 5.2g**). These two

intermediate images were then multiplied together (**Figure 5.2h**) and small holes in the resulting images (**Figure 5.2h** inset) were filled using grayscale closing (**Figure 5.2i** inset). The resulting intermediate images provides a complete boundary of an object but also highlights whether the boundary is in close proximity to any other objects. Compared to previous methods that only provide a complete boundary or only provide boundary areas that are close to any other objects, this new intermediate image representation provides a more informative boundary representation. In a final step, the 'proximity enhanced cell boundary' images were smoothed by Gaussian blurring (kernel size = 5 voxels in each dimension) (**Figure 5.2i**).

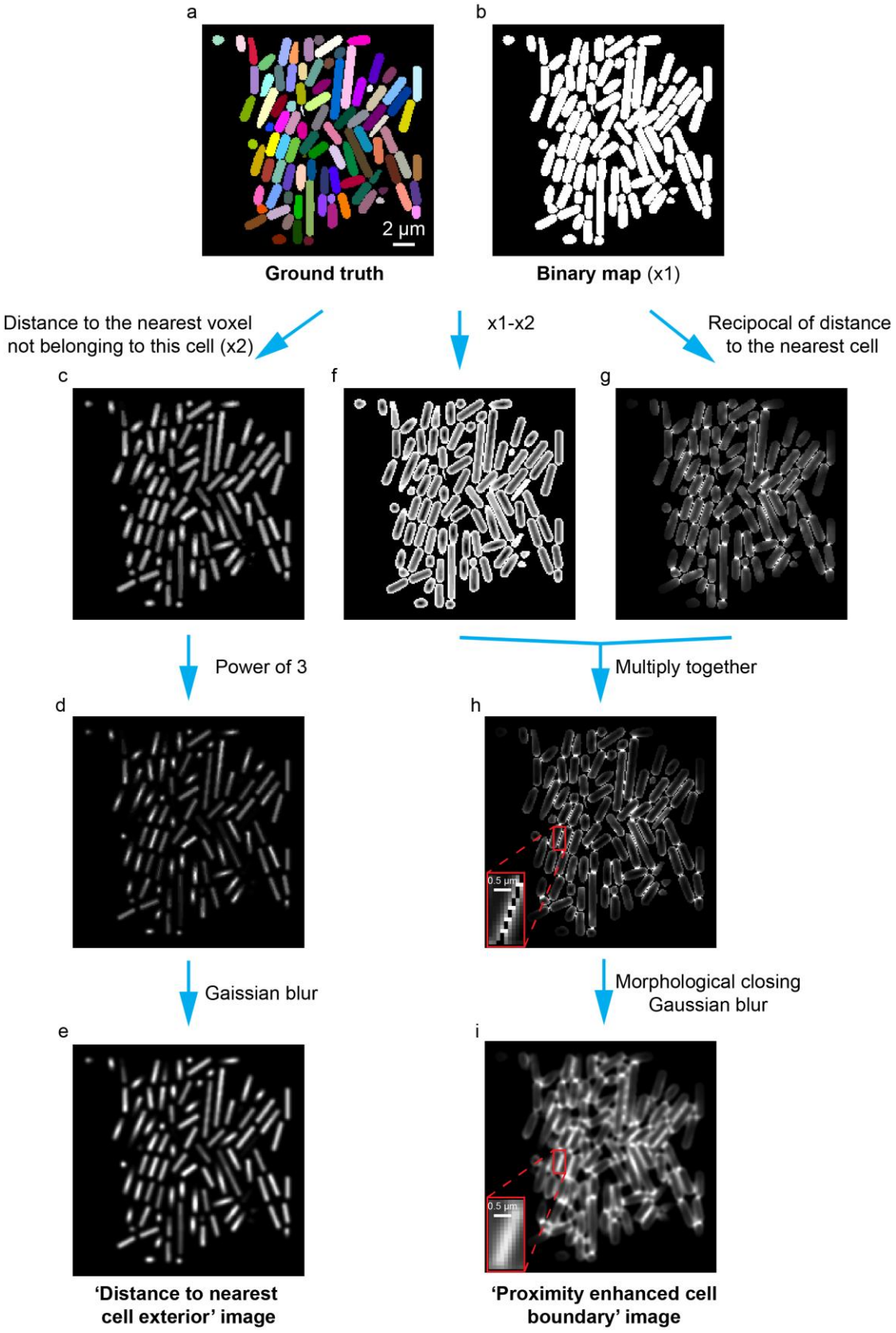
a
b
2 µm
Ground truth
Binary map (x1)
Distance to the nearest voxel not belonging to this cell (x2)
x1-x2
Recipocal of distance to the nearest cell
c
f
g
Power of 3
Multiply together
d
h
0.5 µm
Gaissian blur
Morphological closing
Gaussian blur
e
i
0.5 µm
'Distance to nearest cell exterior' image
'Proximity enhanced cell boundary' image

Figure 5.2 Schematic of generating intermediate image representations. (a) Ground truth cell positions. (b) Binary maps based on the ground truth. (c) Images of distance to the nearest voxel not belonging to this cell. (d) A steeper gradient in distance values is obtained by raising each voxel value in panel c to the third power. (e) Smooth images to get 'distance to nearest cell exterior' image representation. (f) Obtain cell boundary by subtracting (c) from (b). (g) Highlight boundary areas that are close to other cells by calculating reciprocal of distance to the nearest cell. (h) Multiply (f) and (g). The inset shows small holes between two cells' boundary. (i) Small holes (inset) are removed in the 'proximity enhanced cell boundary' image by morphological closing and Gaussian blurring.

5.2.5 Training the convolutional neural network

To generate the above-mentioned intermediate image representations from experimental data, we trained 3D U-Net Based CNNs using the CSBDeep Python package[20]. We employed a network architecture depth of 2, a convolution kernel size of 3, 32 initial feature maps, and a linear activation function in the last layer. To achieve robust performance, we trained this network using ten to twenty simulated biofilm images with randomly selected cell densities and signal-to-background ratio. To ensure the broad applicability of these networks, half of these images were biofilms containing cells expressing cytosolic fluorescence and the other half were biofilms containing membrane-stained cells (see **Figure 5.1d**). Instead of directly learning the intermediate image representations $g(x)$ from the input raw data x, the networks were trained to learn the residual $\tilde{g}(x)$ to the input of the networks, i.e. $g(x) = \tilde{g}(x) + x$. This strategy provides better performance, because solvers are more efficient in solving residual functions than unreferenced functions[44]. The loss function was taken as the mean absolute error (MAE) between the generated

and the target images. The networks were trained for 100 epochs with 100 parameter update steps per epoch and an initial learning rate 0.0004. The learning rate is reduced by a half if the validation loss is not decreasing over 10 epochs. Using these parameters, it took approximately 1 hour to train the CNNs on a NVIDIA Tesla V100 GPU with 32 GB memory.

To test whether segmentation objects have physiologically reasonable cell shapes, we trained a 3D CNNs based classification model using tensorflow 2.0. We adapted a network architecture from Zunair et.al.,[45]; mainly includes three 3D convolutional layers, one global average pooling layer and a sigmoid activation function in the last layer. To achieve robust performance, we trained this network using 733 manually confirmed segmentation objects from experimental data (411 reasonable shaped objects, 322 oddly shaped objects). Training data were augmented by rotation and flip. The loss function was taken as the binary cross entropy between the model output and the corresponding target value. The networks were trained for 100 epochs with a batch size of 5 and an initial learning rate 0.0002. The learning rate is reduced by a half if the validation loss is not decreasing over 15 epochs. Using these parameters, it took approximately 17 mins to train the CNNs on a NVIDIA Tesla V100 GPU with 32 GB memory.

5.2.6 Thresholding of CNN-produced 'distance to nearest cell exterior' images

We processed the predicted intermediate image representations by using scikit-image Python library[46]. Predicted 'distance to nearest cell exterior' images were first normalized by a simple percentile-based normalization method (**Figure 5.3a**), which we define for an input u as

$$N(u; p_{low}, p_{high}) = \frac{u - perc(u, p_{low})}{perc(u, p_{high}) - perc(u, p_{low})}$$

Where perc(u,p) is the p-th percentile of all voxel values of u. We typically use $p_{low} = 3$ and $p_{high} \in (99.5, 99.9)$. After applying Otsu-thresholding[30] to the 'distance to nearest cell exterior' image to obtain a binary image (**Figure 5.3b**), connected voxel clusters can be isolated and identified as single cell objects by labeling connected regions. To split clusters that are only connected by one or two voxels, the boundary voxels of each object were set to zero before labeling connected regions (**Figure 5.3c**). After labeling, the erased boundary voxels were added back to each object (**Figure 5.3d**). A conservative size-exclusion filter was applied: small objects with volume smaller than the radius cubed of the targeted cells were considered background noise and filtered out.

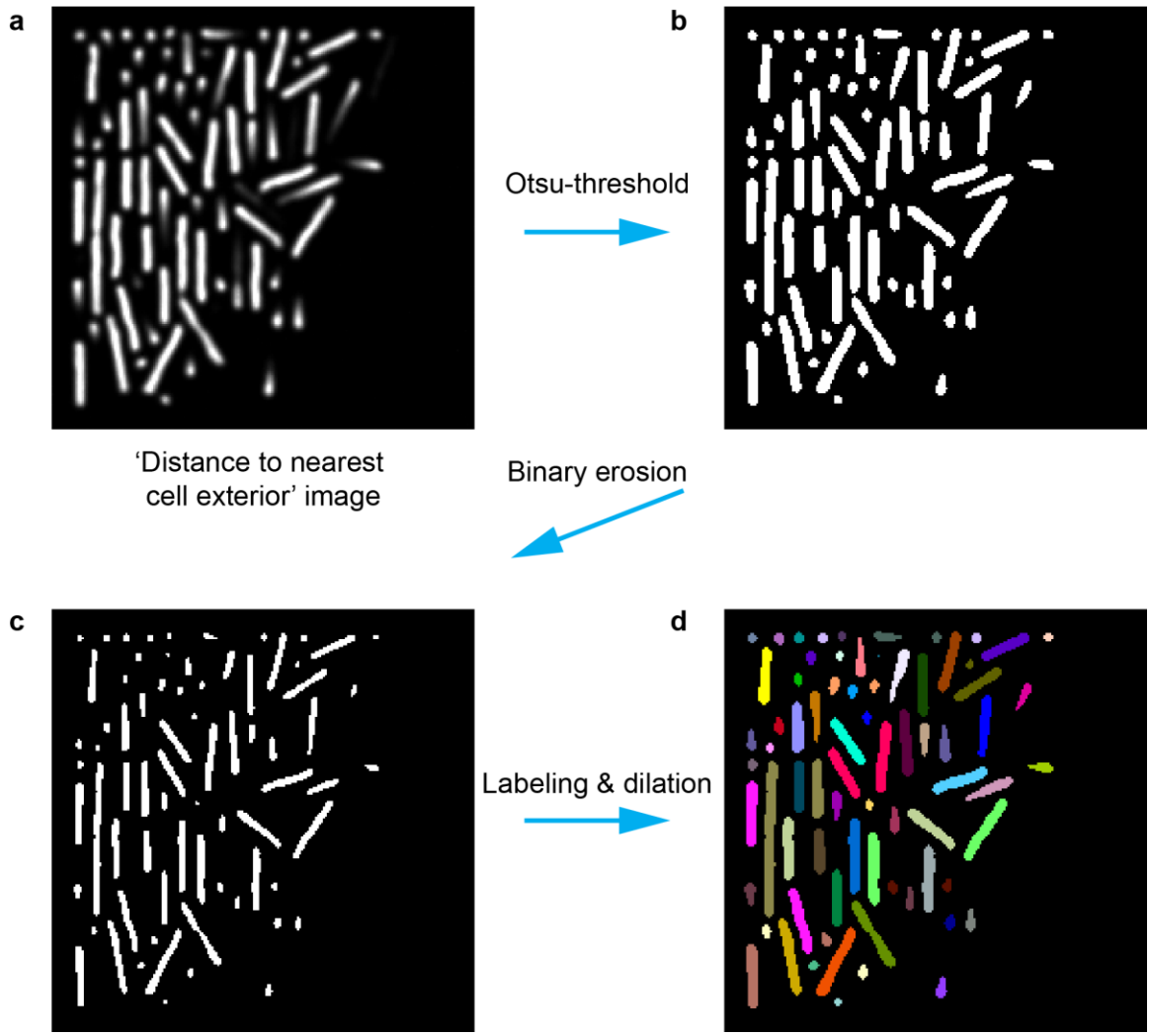

Figure 5.3 Schematic of thresholding of CNN-produced ‘distance to nearest cell exterior’ image. (a) ‘Distance to the nearest cell exterior’ image. (b) Apply Otsu-threshold to obtain binary images. (c) To split clusters that are only connected by one or two voxels, the boundary voxels of each object were set to zero. (d) Identify individual cell objects by labeling connected regions and then add back erased boundary voxels.

5.2.7 Post-processing of initial thresholding result by introducing ‘proximity enhanced cell boundary’ images

Thresholding of the ‘distance to nearest cell exterior’ image produces a binary image (background = 0, cell = 1), where groups of connected, non-zero voxels identify individual cells in most cases. However, when cells are touching, they are often not segmented as individuals, but remain part of the same voxel cluster (undersegmentation). On the other hand, a small part of a cell may be erroneously identified as another cell (oversegmentation). To address these errors and further improve the segmentation accuracy, we included ‘proximity enhanced cell boundary’ image, seeded watershed[29], and multi-level Otsu thresholding[47] to post-process the binary images obtained from the normalized ‘distance to nearest cell exterior’ images (**Figure 5.4**).

Step 1. Objects that need further processing were found by evaluating its volume and solidity, i.e., the volume to convex volume ratio. Here, volume is defined as the number of voxels occupied by an object. Convex volume is defined as the number of voxels of a convex hull, which is the smallest convex polygon that encloses an object. The upper limit was found by using the interquartile rule, i.e. the upper limit is quartile 3 (Q3) plus 1.5 times interquartile range (IQR). If an object's volume or solidity is larger than the upper limit, it will be singled out for further processing. All these objects together generate a new binary image (**Figure 5.4e**).

Step 2. To identify and delineate individual cells in the undersegmented connected voxel clusters, CNN-produced 'proximity enhanced cell boundary' images were first normalized by the same percentile-based normalization method. We used seeded watershed after combining 'distance to nearest cell exterior' images and 'proximity enhanced cell boundary' images. Specifically, we generated a difference map by subtracting the 'proximity enhanced cell boundary' image from the 'distance to nearest cell exterior' image and then set all negative valued voxels to zero (**Figure 5.4abc**). This difference map was then multiplied by the binary image generated in Step 1 (**Figure 5.4f**). Then, the resulting image was segmented by seeded watershed. Seeds were obtained by Otsu thresholding of the difference map and seeds with a volume smaller than 30 voxels were removed (**Figure 5.4g**). These new objects were again evaluated by their volume and solidity; if there still exist unmatched objects, a multi-level Otsu thresholding will be applied to further generate seeds. Unlike simple Otsu thresholding, which only separates voxels into two classes, foreground and background, multi-level Otsu calculates several thresholds, determined by the number of desired classes. Here, we used the following five classes: background, transition area between background and cell border, cell border, transition area between cell border and cell interior, cell interior. Seeds were extracted by using the third and the fourth threshold successively, i.e. the threshold between the third and the fourth classes (cell border, transition area between cell border and cell interior), and the threshold between the fourth and the fifth classes (transition area between cell border and cell interior, cell interior). The same size filter was used to remove unreasonable small seeds (**Figure 5.4h**).

Step 3: All post-process objects were added together (**Figure 5.4i**) and combined with the initially reasonable objects, i.e., the objects haven't been singled out in Step 1. A conservative size-exclusion filter was applied: small objects with volume 10 times smaller than the upper limit

volume were considered unreasonable small parts and filtered out. Since the ‘distance to nearest cell exterior’ images were confined to the cell interior, we dilated each object by 1-2 voxels to increase the cell volumes using standard morphological dilation (**Figure 5.4j**).

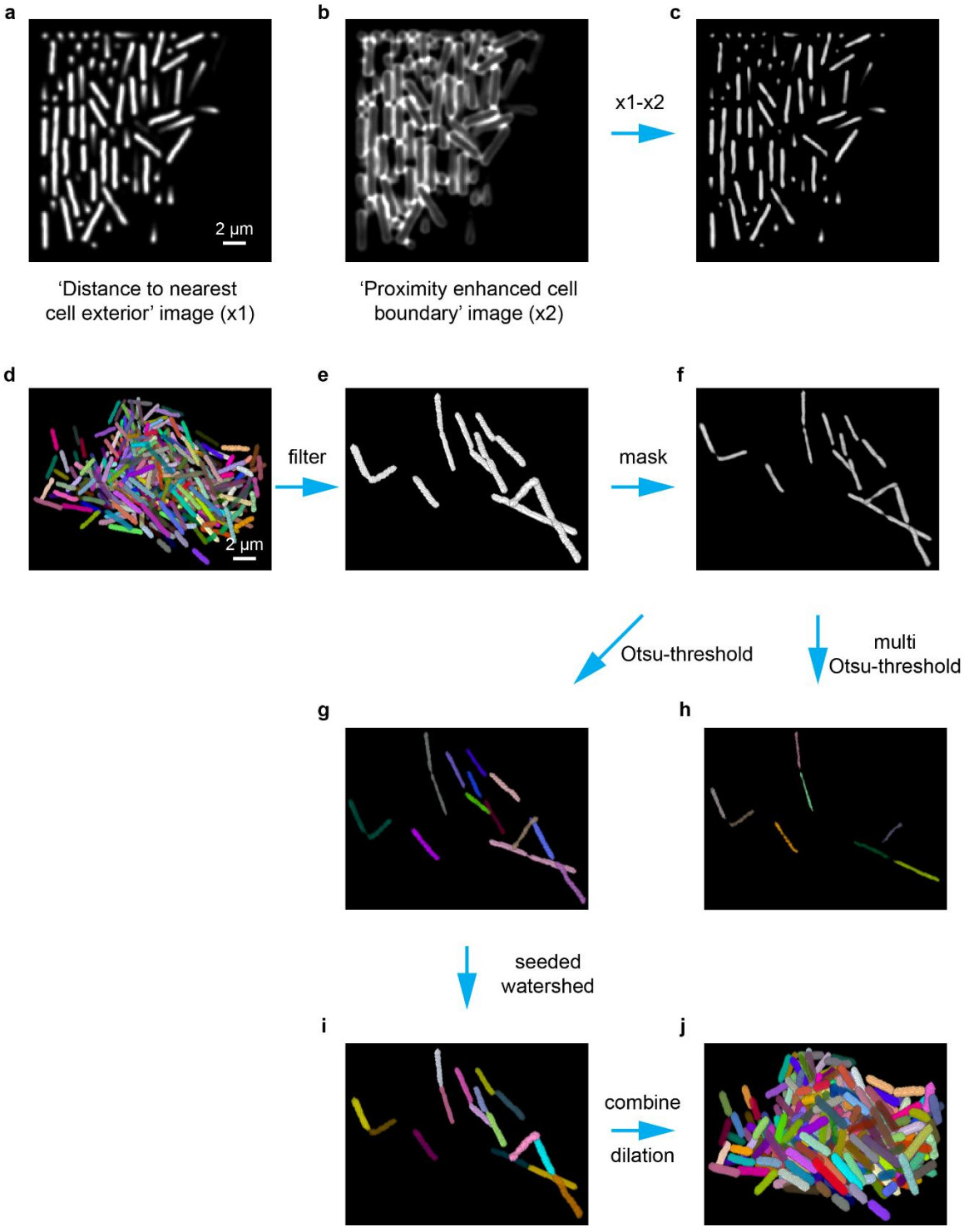

Figure 5.4 Post-processing pipeline using a combination of intermediate image representations. (a) 'Distance to nearest cell exterior' image. (b) 'Proximity enhanced cell boundary' image. (c) Generate difference map by subtracting (b) from (a) and set negative values to zero. (d)

Segmentation results from **Figure 5.3**. (e) Identify objects that need further processing using volume and solidity filters and transfer to binary map. (f) Mask (c) by multiplying (c) with (e). (g) To further split undersegmented clusters, apply seeded-watershed to (f), seeds are obtained by applying Otsu-threshold to (f). (h) If there still are undersegmented clusters after (g), more seeds are obtained by applying multi-level Otsu-threshold to (f). (i) Combine segmented objects from (g) and (h). (j) Combine (i) and (d) to get final segmentation results.

5.2.8 Tracking

Simpletracker in MATLAB was used to build tracking graphs and spatially resolved lineage trees[48]. *Simpletracker* implements the Hungarian algorithm and nearest neighbor trackers for particle tracking that links particles between frames in 2D or 3D. We used 1 μm and 1.5 μm as the maximum distance threshold for cell linking for simulated and experimental data, respectively. We used the nearest neighbor algorithm to associate the centroids of segmented objects in subsequent frames, such that the closer pairs of centroids are linked first. In order to determine a cell division event, a distance threshold of 1 μm and 1.5 μm for simulated and experimental data, respectively, a cell volume threshold of 1.5 (parent cell should be 1.5 times larger than the daughter cell), and a cell length threshold of 1.5 (parent cell should be 1.5 times longer than the daughter cell), were used to determine parent-daughter relationships between cell pairs on consecutive frames.

5.2.9 Performance evaluation

Segmentation accuracy was quantified as cell counting accuracy and cell shape estimation accuracy. The cell counting accuracy (CA) was calculated as previously described[24]:

$$CA = \frac{TP}{TP + FP + FN}$$

where, TP is the number of truth positive objects, FP is the number of false positive objects, and FN is the number of false positive objects. Cell shape estimation is evaluated by two separate measures. Single-cell segmentation accuracy (SSA) takes the mean Intersection-over-Union (IoU) value (aka the Jaccard index[49]) over segments that have a matching ground truth/manual annotation object:

$$SSA = \frac{1}{N_{match}} \sum_{i}^{N_{match}} \frac{|Seg_i \cap GT_i|}{|Seg_i \cup GT_i|}$$

where, $|Seg_i \cap GT_i|$ is volume of overlap between the predicted object and the ground truth object, and $|Seg_i \cup GT_i|$ is the volume enclosed by both the predicted object and the ground-truth object. We note that the SSA metric can take on high values even if the shape of a segmented object does not accurately represent the shape of the corresponding ground truth object. For example, a predicted round object with a diameter of 20 covered by a ground truth square object with a length of 20 gives a 0.8 IoU value, which could be interpreted as good performance. From a biological perspective however, this would signify a substantial inaccuracy in shape estimation. To measure differences in cell shape in a more discriminating way, we additionally computed a single-cell boundary F1 score (SBF1)[50]. The SBF1 of the abovementioned square vs circular object example is 0.67. The SBF1 score is computed as

$$SBF1 = \frac{1}{N_{match}} \sum_{i}^{N_{match}} \frac{2 \cdot prcecision_i \cdot recall_i}{prcecision_i + recall_i}$$

where precision is the ratio of matching boundary points in a matched segmentation object to the total points of its boundary. Similarly, recall is the ratio of the matching boundary points to the total points of ground truth boundary. According to the definition of boundary F1 score[51], a distance error tolerance is used to decide whether a point on the predicted boundary has a match on the ground truth boundary. For our 3D data, we use $\sqrt{3}$ voxels.

To quantify tracking accuracy, we used the acyclic oriented graph metric (*AOGM*)[52]. The *AOGM* value is calculated as the weighted sum of the number of graph operations required to convert the estimated graph to the ground truth graph, i.e.:

$$AOGM = w_{NS}NS + w_{FN}FN + w_{FP}FP + w_{ED}ED + w_{EA}EA + w_{EC}EC$$

The tracking accuracy can then be computed using a normalized *AOGM* value, where $AOGM_0$ is the number of operations to build the ground truth graph from an empty graph:

$$TRA = 1 - min(AOGM, AOGM_0)/AOGM_0$$

There are three types of graph operations that are associated with detection errors: the number of false negatives (*FN*), the number of false positives (*FP*), and the number of missed splits (*NS*: m reference cells ($m > 1$) are assigned to a single segmented cell); and three types of graph operations that are associated with object linking: edge deletion (ED), addition (*EA*), and alteration of the semantics of an edge (*EC*: The semantics of an edge can either represent the same cells over time or represent a parent-daughter relationship). To focus on object matching over time (i.e. the association performance of the algorithm), we used an equally weighted sum of the lowest number of graph operations on edges only (*TRA_edge*). To give a more comprehensive view, we used an equally weighted sum of the number of graph operations on all six operations (*TRA_full*).

To estimate tracking accuracy for experimental data, we manually traced a small subset (n = 25) ancestor cells over time based on *BCM3D 2.0* segmentation masks. Two researchers

performed tracking independently, manually determining parent-daughter relationships within the lineages originating from the ancestor cells. This lineage information was then used to compute *TRA_edge.*

5.3 Results

5.3.1 Cell segmentation using intermediate image representations

High cell density and low SBR datasets are encountered often in biofilm research, especially when cells seem to touch each other and biofilms extend far into the vertical (*z*-) dimension, so that light scattering becomes pronounced [53]. We therefore sought to improve bacterial cell segmentation accuracy for high cell density and low SBR biofilm images in particular. Our previous approach (*BCM3D 1.0*) relied on deconvolution as a preprocessing step to increase the SBR and to sharpen the image. However, deconvolution can introduce artifacts into an image, such as ringing[54], and noise amplification[55], and thereby introduce errors into the segmentation results. The segmentation pipeline of *BCM3D 2.0*, in contrast, works on the raw image data directly without the need for deconvolution.

We compared two commonly used cell labeling approaches, namely cell interior labeling through expression of cytosolic fluorescent proteins and cell membrane staining through membrane-embedded fluorescent dyes. For cell interior labeling (**Figure 5.5ab**), *BCM3D 2.0* consistently produces cell counting accuracies of >95%, when SBRs > 1.3 and cell densities < 65%. A clear drop off in cell counting accuracy is observed for SBRs < 1.3, but >70% is still achieved even for high cell densities of 65%. The performance of *BCM3D 2.0* on low SBR datasets represents a large improvement (>20%) over the performance of *BCM3D 1.0*. Membrane staining (**Figure 5.5cd**) produces even more challenging images for segmentation, due to the less pronounced inter-cellular fluorescence intensity minima (red arrow in **Figure 5.5bd**). We again

observe a drop in cell counting accuracy for SBRs < 1.3. This drop off is however much less pronounced than for the previous results obtained with *BCM3D 1.0*, and represents an even larger (>29%) improvement for such extremely low SBR datasets. Visual inspection of slices through the image volumes (**Figure 5.5bd**) reveals that even for SBR = 1.3, the cell bodies are difficult to distinguish for expert human annotators, especially for membrane-stained cells. Despite the low contrast in the SBR = 1.3 datasets, *BCM3D 2.0* is still able to achieve >90% cell counting accuracies, which, depending on cell density, represents a 6-26% increase relative to *BCM3D 1.0*.

To determine the improvement in cell shape estimation, we plotted the cell counting accuracies as a function of IoU matching threshold, a quantitative measure of cell shape similarity relative to the ground truth, for SBR = 1.3 and cell density 62% (**Figure 5.5ef**). The cell counting accuracies obtained by *BCM3D 2.0* are consistently higher than *BCM3D 1.0* for IoU matching thresholds larger than 0.5, indicating that cell shapes are more accurately estimated by *BCM3D 2.0*. Similar trend is observed for single-cell segmentation accuracy and single-cell boundary F1 score[50] – two additional metrics for segmentation accuracy (**Table 5.1**). Taken together, these results establish that more robust cell segmentation can be achieved using the *BCM3D 2*.0 image processing pipeline, which uses CNNs to generate intermediate image representations for subsequent mathematical processing.

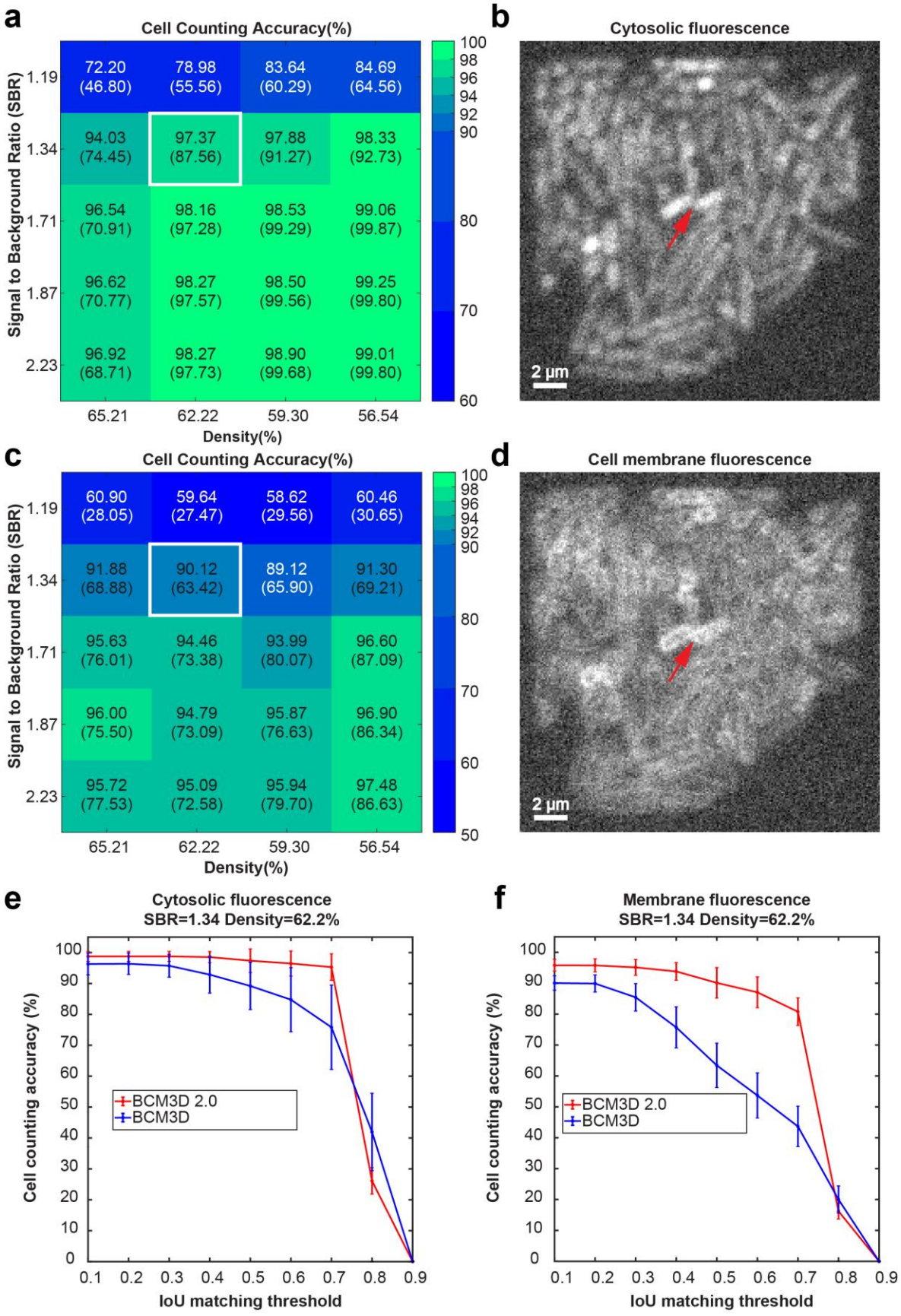
a
Cell Counting Accuracy(%)
72.20 (46.80)
78.98 (55.56)
83.64 (60.29)
84.69 (64.56)
94.03 (74.45)
97.37 (87.56)
97.88 (91.27)
98.33 (92.73)
96.54 (70.91)
98.16 (97.28)
98.53 (99.29)
99.06 (99.87)
96.62 (70.77)
98.27 (97.57)
98.50 (99.56)
99.25 (99.80)
96.92 (68.71)
98.27 (97.73)
98.90 (99.68)
99.01 (99.80)
Signal to Background Ratio (SBR)
1.19
1.34
1.71
1.87
2.23
65.21
62.22
59.30
56.54
Density(%)
100
98
96
94
92
90
80
70
60
b
Cytosolic fluorescence
2 μm
c
Cell Counting Accuracy(%)
60.90 (28.05)
59.64 (27.47)
58.62 (29.56)
60.46 (30.65)
91.88 (68.88)
90.12 (63.42)
89.12 (65.90)
91.30 (69.21)
95.63 (76.01)
94.46 (73.38)
93.99 (80.07)
96.60 (87.09)
96.00 (75.50)
94.79 (73.09)
95.87 (76.63)
96.90 (86.34)
95.72 (77.53)
95.09 (72.58)
95.94 (79.70)
97.48 (86.63)
Signal to Background Ratio (SBR)
1.19
1.34
1.71
1.87
2.23
65.21
62.22
59.30
56.54
Density(%)
100
98
96
94
92
90
80
70
60
50
d
Cell membrane fluorescence
2 μm
e
Cytosolic fluorescence
SBR=1.34 Density=62.2%
Cell counting accuracy (%)
IoU matching threshold
BCM3D 2.0
BCM3D
f
Membrane fluorescence
SBR=1.34 Density=62.2%
Cell counting accuracy (%)
IoU matching threshold
BCM3D 2.0
BCM3D

Figure 5.5 Performance of *BCM3D 2.0* on previously unseen simulated biofilm images. (a) Cell counting accuracy (using an IoU matching threshold of 0.5 for each segmented object) averaged over *N*=10 replicate datasets for cells labeled with cytosolic fluorophores. (b) Example image of cells labeled with cytosolic fluorophores (Cell density = 62.2%, SBR = 1.34, indicated by white rectangle in panel a). (c) Cell counting accuracy (using an IoU matching threshold of 0.5 for each segmented object) averaged over *N*=10 replicate datasets for cells labeled with membrane-localized fluorophores. (d) Example image of cells labeled with membrane-localized fluorophores (Cell density = 62.2%, SBR = 1.34, indicated by white rectangles in panel c). The red arrow indicates a close cell-to-cell contact. (e and f) Comparison of segmentation accuracies achieved by *BCM3D 1.0* and *BCM3D 2.0* for cytosoclic and membrane labeling, respectively (SBR = 1.34, cell density = 62.2%). Segmentation accuracy is parameterized in terms of cell counting accuracy (*y* axis) and IoU matching threshold (*x* axis). Each data point is the average of *N*=10 independent biofilm images. Data are presented as mean values ± one standard deviation.

	Cytosolic labeling		Membrane labeling	
	SSA	SBF1	SSA	SBF1
BCM3D 1.0	0.796 ± 0.021	0.983 ± 0.008	0.756 ± 0.009	0.961 ± 0.007
BCM3D 2.0	0.791 ± 0.004	**0.995** ± **0.001**	**0.773** ± **0.005**	**0.988** ± **0.002**

Table 5.1 Quantitative comparison of single cell level segmentation accuracy between *BCM3D 1.0* and *BCM3D 2.0*. SSA and SBF1 estimate how accurately the shape of a matched object compare with it of the corresponding ground truth. Here, the IoU threshold is 0.5 and the distance

error tolerance for SBF1 is $\sqrt{3}$ voxels. (See methods for details). Data are presented as mean values ± one standard deviation, the better performance (if different within error) is marked in bold.

5.3.2 Segmentation of experimentally obtained biofilm images

To test the performance of *BCM3D 2.0* on experimental data, we acquired images of *S. oneidensis* biofilms expressing GFP. Visual inspection of the segmentation results obtained by applying *BCM3D 2.0* (see Methods), showed physiologically reasonable cell shapes for a majority of segmented objects (**Figure 5.6**). To quantitatively evaluate segmentation performance, manual annotation results are often used as references. However, manual annotation of 3D biofilm images is inconsistent itself and it therefore very time consuming to provide reliable results[24], especially for 3D data. We therefore chose to assess the segmentation accuracy using representative morphological observables that are available after segmentation, namely object volume, object solidity (volume fraction of the object as compared to the smallest convex polygon that encloses it), major axis length, longer minor axis length, and the ratio of the two minor axes lengths (longer minor axis divided by the shorter one). We performed principal component analysis (PCA) using these morphological observables and project each segmented object onto a plane spanned by the first two principal components. For simulated data (for which the ground truth is known) this approach shows a distribution for which the correctly segmented objects are concentrated near the origin, whereas the incorrectly segmented objects are predominantly located at the periphery (**Figure 5.6a** inset).

We next applied the same PCA approach to experimental segmentation results obtained for a *S. oneidensis* biofilm containing ~3000 cells (**Figure 5.6a**). Similar to simulated data, most of the segmentation objects cluster near the origin of the two principal component axes. However, several segmented objects are asymmetrically scattered around the periphery of the distribution.

Inspecting the 3D shapes of a few manually selected objects revealed that, consistent with simulated data, physiologically reasonable cell shapes cluster near the center of the distribution, while oddly shaped objects predominantly localize at the periphery. To automatically separate oddly shaped objects from the physiologically reasonable, rod-shape shaped objects, we trained a 3D CNN with manually validated segmentation objects (obtained from experimental data, see methods). The trained network efficiently separates rod-shaped objects (~86% of total) from oddly shaped objects (~14% of total). This classification enables the display of both subpopulations separately even though they are completely intermixed in 3D space (**Figure 5.6bc**).

We further compared the distributions of solidity and minor axis ratio between rod-shaped and oddly shaped populations. Rod-shaped objects are characterized high values of solidity and minor axis ratio (**Figure 5.6de**). In contrast, solidity and minor axis ratio for oddly shaped objects take on values less than one and thus show a much broader distribution (**Figure 5.6de** insets). These results show that, when using *BCM3D 2.0*, ~86% of cells are segmented with physiologically reasonable cell shapes. The remaining 14% of cells can then either be excluded from the analyses or be subjected to further processing to identify and correct the remaining segmentation errors[24, 25, 50].

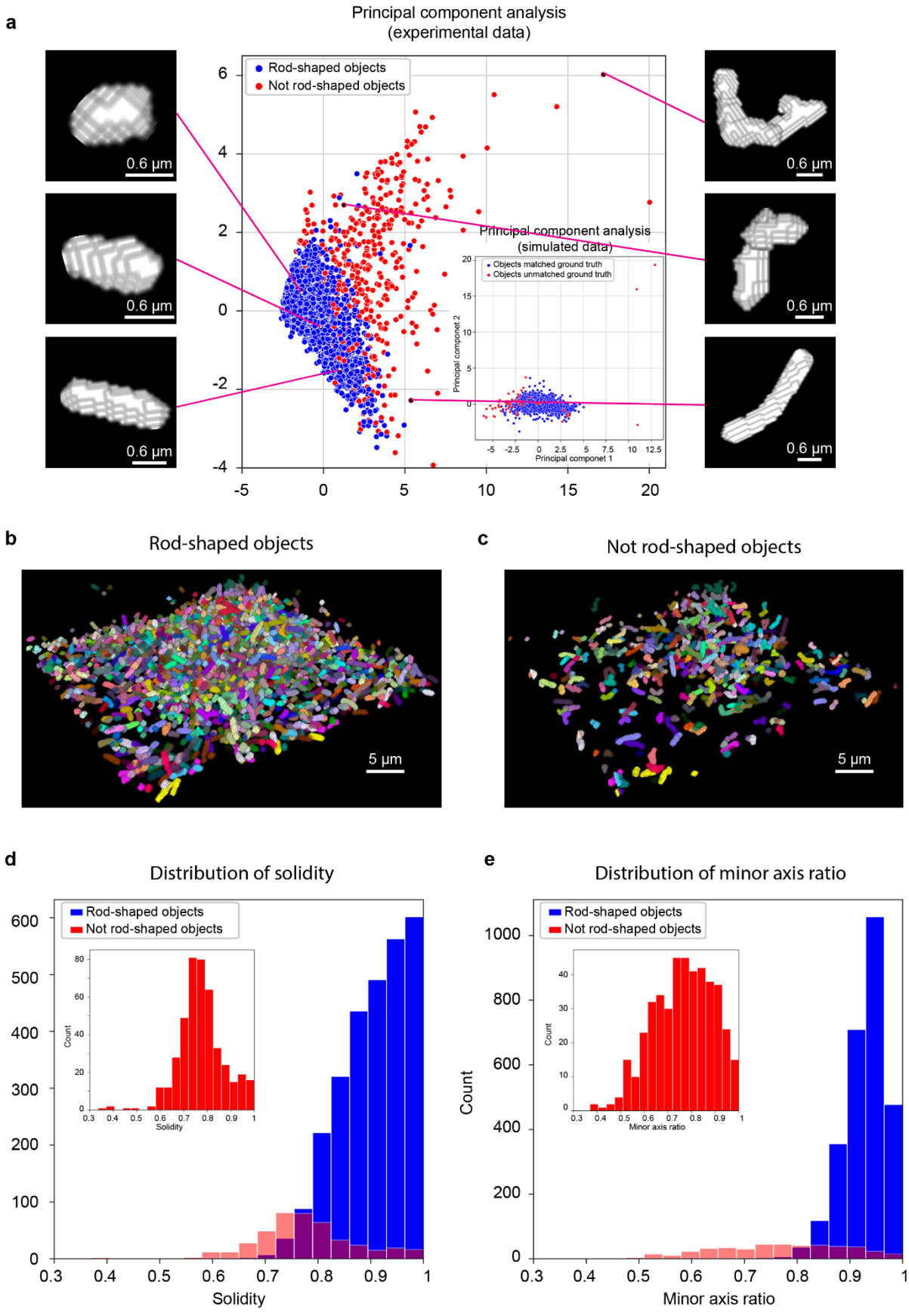
a
Principal component analysis
(experimental data)
Rod-shaped objects
Not rod-shaped objects
Principal component analysis
(simulated data)
Objects matched ground truth
Objects unmatched ground truth
Principal componet 2
Principal componet 1
0.6 µm
b
Rod-shaped objects
5 µm
c
Not rod-shaped objects
5 µm
d
Distribution of solidity
Rod-shaped objects
Not rod-shaped objects
Count
Solidity
e
Distribution of minor axis ratio
Rod-shaped objects
Not rod-shaped objects
Count
Minor axis ratio

Figure 5.6 Performance of *BCM3D 2.0* on experimental biofilm images. (a) Principal component analysis of the segmentation objects (obtained from experimentally acquired images) that were classified by a pre-trained 3D CNN into either physiologically reasonable rod-shaped cells or oddly shaped (not-rod shaped) cells. Three examples cell shapes of each class are shown to the right and left, respectively. Inset: same analysis on simulated biofilm images. (b) Segmentation objects classified as physiologically reasonable rod-shaped cells. (c) Segmentation objects classified as oddly shaped. (d) and (e) Comparison of the solidity and minor axis ratio distributions of rod-shaped and oddly shaped objects.

5.3.3 Accurate *BCM3D 2.0* segmentation enables multi-cell tracking in biofilms.

Simultaneous multi-cell tracking and lineage tracing is critical for analyzing single-cell behaviors in bacterial biofilms. We asked whether the cell segmentation performance of *BCM3D 2.0* was sufficient to enable accurate tracking of individual cells in biofilms. To address this question, we employed a tracking-by-detection approached using simulated biofilm images of different SBRs (**Figure 5.7a**). We evaluated tracking accuracy, as a function of SBR, using the widely used *TRA* metrics based on Acyclic Oriented Graph Matching (AOGM)[52]. In acyclic oriented graphs, cells in different time frame are represented as vertices and linkages between cells from frame-to-frame are represented as edges. When the cells (vertices) are placed at their actual (x,y,z) spatial coordinates, then the cell linkages (edges) represent the branches of a spatially resolved lineage tree (**Figure 5.7b**). The *TRA* metrics quantify how many elementary graph operations are needed to transform an estimated graph into a ground truth graph. *TRA_edge* considers three edge operations, while *TRA_full* considers all six graph operations[52].

To link the same cells across two different time points, we used a nearest neighbor algorithm[56]. When using spatial distance as the sole metric for cell linking, the AOGM tracking

accuracy has a positive correlation with SBR (**Figure 5.7c**), which highlights the importance of accurate cell segmentation in multi-object tracking-by-detection[57]. *BCM3D 2.0* enables a tracking accuracy that is similar to the ground truth tracking accuracy (same nearest neighbor tracking algorithm applied to the ground truth segmentation masks) for SBRs of 1.65 and higher. We note that, given the high cell density in this test dataset, the ground truth tracking accuracy does not reach the optimum (100%) even with error-free segmentation. At SBR's less than 1.65, tracking accuracy decreases rapidly due to the lack of consistent segmentation results. The importance of accurate segmentation is further supported, by the linear dependence of *TRA* as a function of cell counting accuracy (**Figure 5.7d**).

Another key factor for simultaneous multi-object tracking is the time resolution[57]. The relative movement (RM) of objects from frame to frame is therefore a useful metric to quantify the level of difficulty for cell tracking. The relative movement ($RM_{i,j}$) in time frame *i*, for a given cell *j* is defined the ration between the distance of cell *j* to iteself between frame i and *i*+1 and the distance of cell *j* in frame *i* to its closest neighbor at frame *i* + 1. The *RM* metric is then the average $RM_{i,j}$ of all cells for each frame[58]. A $RM > 1$ means that any tracking method that considers only distance (and distance related features) is likely to fail, whereas a RM of 0.5 is considered challenging[58]. For the simulated biofilm images here, $RM \sim 0.2$, which indicates that the time resolution is good enough for successful single cell tracking using a nearest neighbor algorithm. Indeed, under these conditions, many cells can be tracked for several generations (**Figure 5.7b**), which allows for the estimation single-cell doubling cycles in the biofilm (**Figure 5.7e**). However, even at $RM \sim 0.2$, some cell division events are missed, so that a few branches of the lineage three are not successfully traced. We therefore tested how time resolution affects tracking accuracy. When the time resolution is decreased by a factor of two and three, the *TRA_edge* metrics decrease

from 91% to 87% and 81%, respectively. The percentage of the parent-daughter misassignment error or edge-correction (EC) error over the number of total errors, increases from 1.4% to 3.6 and to 5.2 % (**Figure 5.7f**). Taken together, these results show that segmentation based multi-object tracking accuracy is highly dependent on segmentation accuracy (which depends on image SBR and cell density[24]) and time resolution. It is therefore critical to consider these parameters, when single-cell resolved observables, such as cell trajectories, single cell volume increases, and single-cell doubling times, are measured.

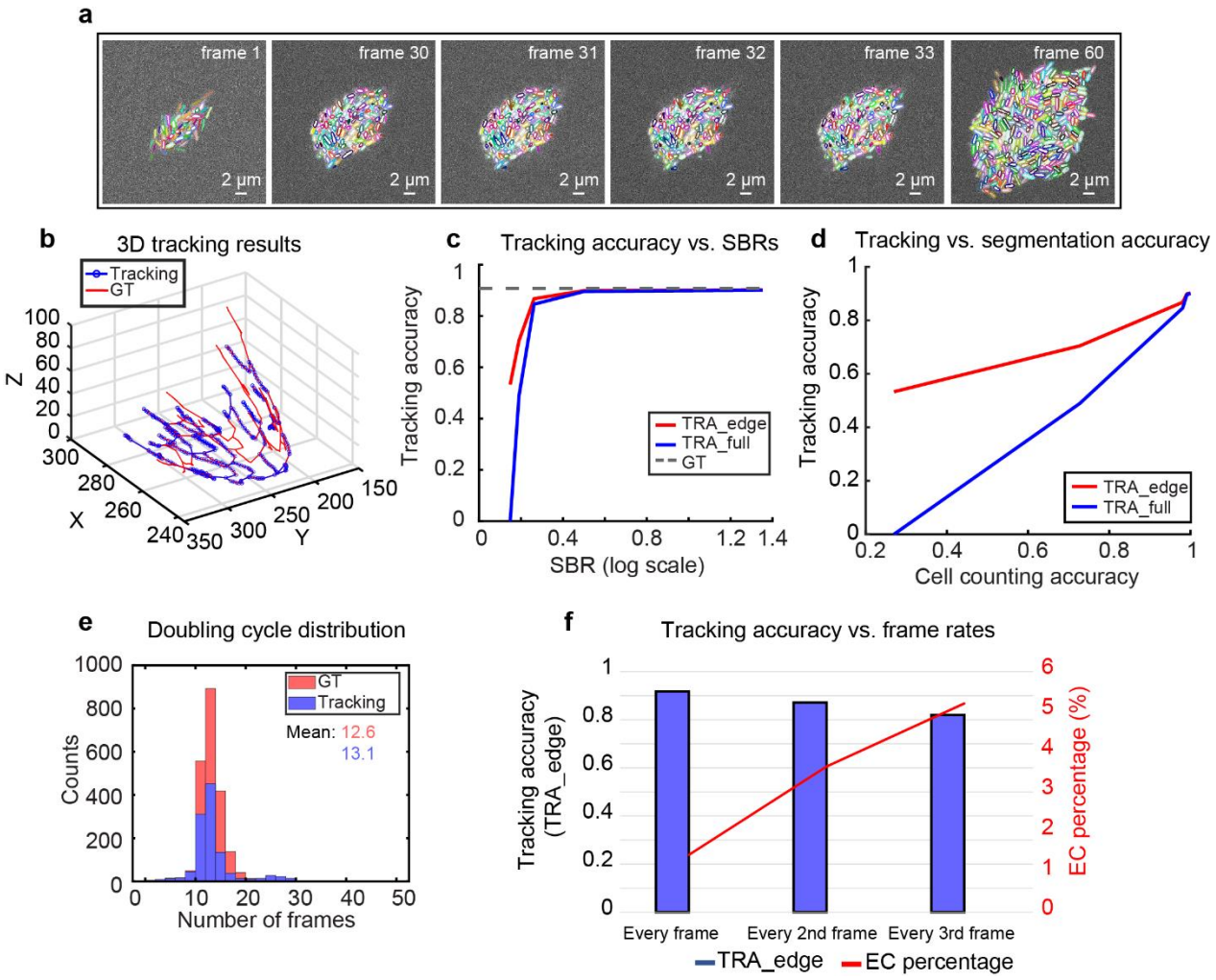

Figure 5.7 Multi-cell tracking in simulated biofilms. (a) Simulated fluorescence time-lapse images of growing *E. coli*-like biofilm. The SBRs of these images are estimated to be 1.65. Contours are

color-coded based on segmentation and tracking results. (b) An example of 3D tracking and lineage tracing for simulated biofilm images. For clarity, spatial trajectories and lineages originating from a single ancestor cell is displayed. The estimated graph is shown in blue and the corresponding ground truth graph is shown in red. The entire biofilm contains over sixty graphs of this type. (c) Two AOGM metrics calculated as *TRA_edge* and *TRA_full* are plotted against image SBRs. The grey dashed line indicates tracking of the GT segmentation using the same tracking algorithm. (d) Same data as in panel c plotted as a function of cell counting accuracy at IoU = 0.5, a segmentation accuracy metric that increases for increasing SBR in the raw images[59]. (e) Doubling cycle distribution of simulated data and corresponding tracking results. A completed cell cycle is defined as a track in which the parent cell is able to split twice. This threshold results in a lower count numbers of estimated cell division, but does not alter the shape of the distribution. (f) *TRA_edge* (left axis) and edge correction (EC) percentage (right axis) for different temporal sampling. EC percentage indicates how many parent-daughter relationships are misassigned based on the tracking results.

5.3.4 Multi-cell tracking in the initial phase of *S. oneidensis* biofilm

Cell segmentation and subsequent multi-cell tracking in experimentally acquired 3D images presents additional challenges that were not modeled in the computationally simulated data. These challenges include optical aberrations in the imaging system, broader cell shape distributions in experimental biofilms, cell motility, and association and dissociation dynamics of individual cells to and from the biofilm. To determine whether the *BCM3D 2.0* segmentation results enable multi-cell tracking using a nearest neighbor algorithm, we manually traced a subset of ancestor cells over the course of a 15-minute 3D biofilm movie acquired with a time resolution of 30 seconds (**Figure 5.8ab**). Manual determination of cell-to-cell correspondences in

consecutive image volumes generated 583 cell-cell and 3 parent-daughter linkages. Taking this manual annotation as the reference graph, the *RM* metric was determined to be ~0.2 and the *TRA_edge* metric was determined to be 93.5%. Steadily increasing single cell volumes corresponding to growth rates of 7.4×10^{-3}, 7.6×10^{-3}, 1.2×10^{-3}, and 6.8×10^{-3} μm^3/min, which are followed by cell division events in two cases are readily detected by the algorithm (**Figure 5.8c**). We also found a high number of cell dispersion events resulting in the termination of some trajectories, most often right after cell division (**Figure 5.8c**).

Although *BCM3D 2.0* in combination with high-frame rate imaging enables accurate cell tracking, it may not be feasible to maintain high-frame rate volumetric imaging for extended time periods due to phototoxicity and photobleaching concerns. To further test the limits of nearest neighbor tracking, we tracked *S. oneidensis* biofilm growth for five hours at a time resolution of 5 minutes (**Figure 5.8de**). We manually traced a subset of founder cells over the course of the experiment, generating 262 cell-cell and 17 parent-daughter linkages. The *RM* metric was determined to be ~0.4 and *TRA_edge* metric was determined to be 80.0% for this manually selected subset. While the nearest neighbor tracking algorithm is capable of making somewhat accurate cell-cell linkages for a few consecutive frames, tracking the same cells for long time periods and correctly detecting cell-division events is error-prone, at least for the *S. oneidensis* biofilms imaged here. The red arrow in **Figure 5.8f** indicates a manually validated cell splitting event that was missed by the algorithm due to the distance threshold of 1.5 μm not met when searching for potential daughter cells in the next frame (see methods). After the cell division event, daughter cell remains tethered to the parent, which resulted in an undersegmentation error in the subsequent frame and thus a doubling in cell volume (red box in **Figure 5.8f**). The magenta box in **Figure 5.8f** indicates a second case of failure in which many cells in this biofilm region start moving

rapidly, so that trajectories cannot be manually validated. The division event marked on the trajectory is thus likely to be a false positive detection in which it is erroneously linked to a different neighboring cell.

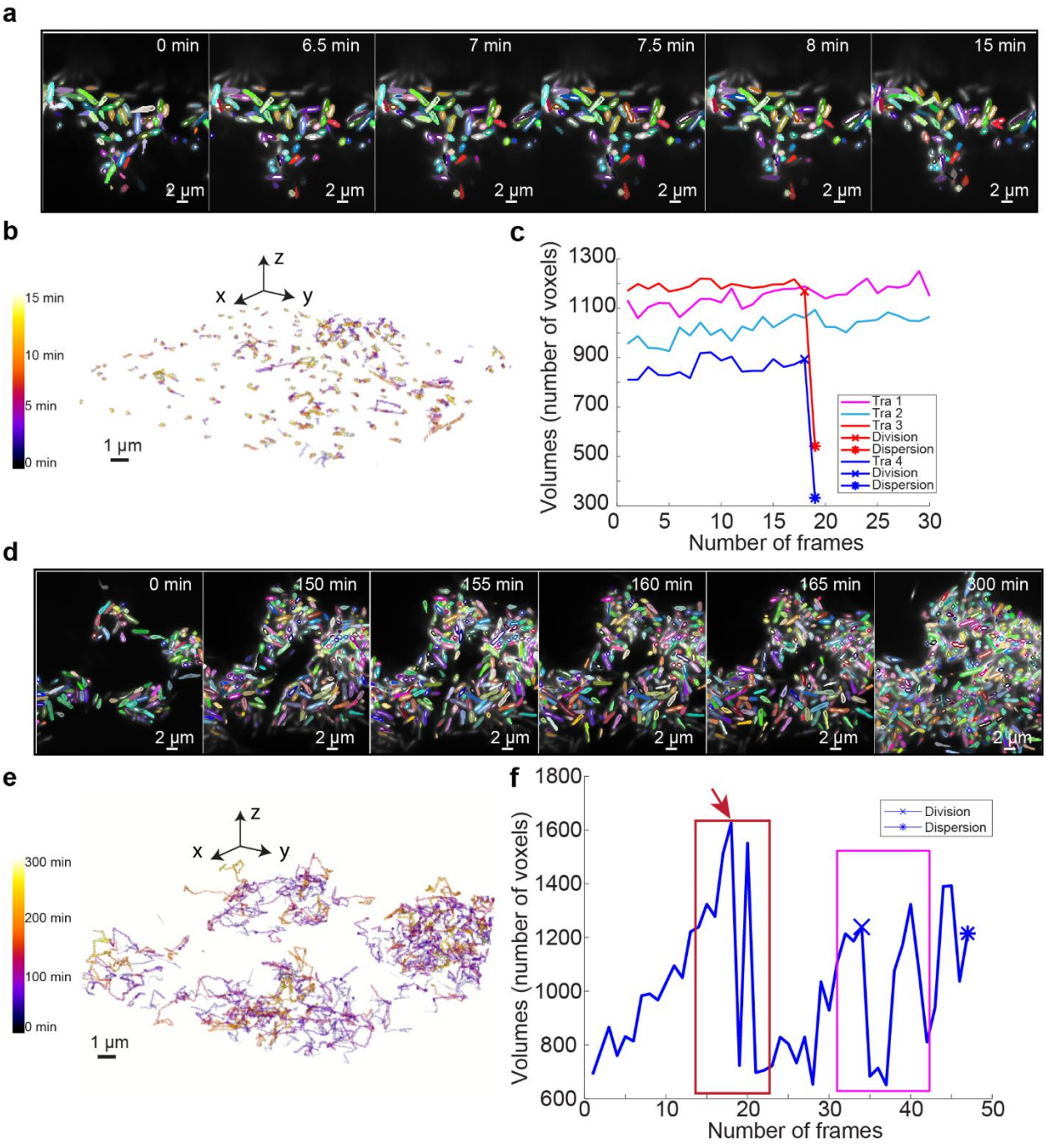

Figure 5.8 (a) Experimentally acquired fluorescence time-lapse images of a growing *S. oneidensis* biofilm with overlaid single-cell segmentation contours. Images were acquired every 30 seconds for 15 minutes. Corresponding cells in different frames are displayed in the same color. (b) Individual cell trajectories in the biofilm shown in panel a. Cells move very little during the short 15-minute imaging time. (c) Cell volume over time for two selected cells. Cell division and dispersion events are indicated for each trajectory. (d) Experimentally acquired fluorescence time-lapse images of a growing *S. oneidensis* biofilm with overlaid single-cell segmentation contours. Images were acquired every five minutes for five hours. Corresponding cells in different frames are displayed in the same color. (e) Individual cell trajectories in the biofilm shown in panel a. Cell displacements are more pronounced over the 5-hour imaging time. (f) Cell volume over time for a selected cell. Cell division and dispersion events are indicated on the trajectory. The red arrow indicates a manually determined cell division event. The boxes indicate two separate failure cases (see the main text for discussion).

5.4 Conclusions

We expanded the *BCM3D* workflow with a complementary CNN-based processing pipeline, named *BCM3D 2.0*, which transfers raw 3D fluorescence images to intermediate image representations that are more amenable to conventional mathematical image processing (specifically, seeded watershed and single- and multi-level Otsu thresholding). Using the *BCM3D 2.0* image processing pipeline, improved segmentation results are obtained, especially for challenging datasets characterized by low SBRs and high cell densities. *BCM3D 2.0* consistently achieves better segmentation accuracy than its predecessor, *BCM3D 1.0*, which represented the previous state-of-the-art for 3D cell segmentation in bacterial biofilms.

We used the segmentation results provided by *BCM3D 2.0* as the input to a nearest neighbor tracking algorithm to explore the possibility of simultaneous multi-cell tracking in 3D biofilms. We found that accurate multi-cell tracking in 3D time-lapse movies is possible with a nearest neighbor tracking algorithm, only if the relative cell movement (RM) between consecutive frames is small. Depending on the type of biofilm and the bacterial species, small RM values can be achieved using moderate time resolutions of 1-5 minutes. However, for the motile *S. oneidensis* cells imaged here, a time resolution of 5 minutes was insufficient for accurate cell tracking in dense biofilm regions. Tracking accuracy is reduced especially if cells undergo large and unpredictable displacements within the biofilm, and when cells associate or dissociate to and from the biofilm.

A clear experimental solution would be to image biofilms at high time resolutions. However, every fluorescence imaging modality is subject to trade-offs between the achievable spatial and temporal resolution, image contrast (SBR), and phototoxicity and photodamage. When imaging *S. oneidensis* biofilms every 30 s, we did not observe any apparent phototoxicity and photodamage to the cells. Even so, after several hours of time-lapse imaging, the majority of cells dispersed from the field-of-view. Whether this behavior is part of a negative phototaxis response of *S. oneidensis* remains to be investigated more quantitatively in future work. If reducing the total radiation dose delivered to the cells is an experimental necessity, light sheet-based microscopy approaches offer substantial advantages over confocal microscopy[53]. In our lattice light sheet microscope, a high (30 s) time resolution could possibly be maintained at a lower, more tolerated radiation dose by further decreasing the excitation laser intensities at the sample and acquiring images at even lower SBRs.

While *BCM3D 2.0* is capable of segmenting biofilm datasets of lower SBR than previous methods, further modifications to the image processing pipeline may be needed to enable the tracking of extremely light sensitive or highly motile bacterial species. Additional modifications could be made to further improve segmentation accuracy for datasets with even lower SBRs than those successfully segmented here. On the other hand, more sophisticated tracking algorithms could be employed that consider additional features beyond the Euclidian distances between objects. Recently developed deep learning-based cell trackers for both 2D and 3D data[60, 61] are primarily designed for mammalian cells that have very unique cell shapes that can be used to define similarity features that inform cell linking across different frames. To what extent such approaches would improve tracking of bacterial cells that have very homogeneous cell shapes remains to be explored. Further benefits may also be gained by utilizing punctate cell labeling schemes[62] or adaptive microscopy approaches in which higher illumination intensity frames are interspersed with lower illumination intensity frames and the segmentation results in lower SBR frames are informed by the more accurate results obtained in the higher SBR frames.

In summary, the ability to accurately identify and track individual cells in dense 3D biofilms over long periods of time will require the combination of non-invasive and perhaps adaptive fluorescence microscopy approaches for long-term time-lapse imaging, as well as sophisticated image analysis and multi-object tracking tools that provide robust results even for datasets with limited spatial and temporal resolution, and image contrast. Here, we have presented an image processing pipeline that enables improved segmentation of dense biofilm-dwelling cells based on 3D fluorescence images of low SBR. The feasibility of simultaneous multi-cell tracking using a simple nearest neighbor tracking algorithm was shown to be feasible if a sufficiently high time resolution can be maintained. The tools developed here can thus be leveraged to improve our

understanding of how coordinated behaviors among biofilm-dwelling cells eventually produce in the macroscopic properties of bacterial biofilms.

References

1. Zhang, J.; Wang, Y.; Donarski, E., et al., BCM3D 2.0: Accurate segmentation of single bacterial cells in dense biofilms using computationally generated intermediate image representations. *bioRxiv* **2021**, 2021.11.26.470109.

2. Nadell, C. D.; Drescher, K.; Foster, K. R., Spatial structure, cooperation and competition in biofilms. *Nature Reviews Microbiology* **2016,** *14* (9), 589.

3. Flemming, H. C.; Wingender, J.; Szewzyk, U., et al., Biofilms: an emergent form of bacterial life. *Nat Rev Microbiol* **2016,** *14* (9), 563-75.

4. Jayathilake, P. G.; Gupta, P.; Li, B., et al., A mechanistic Individual-based Model of microbial communities. *PLoS One* **2017,** *12* (8), e0181965.

5. Persat, A.; Nadell, C. D.; Kim, M. K., et al., The mechanical world of bacteria. *Cell* **2015,** *161* (5), 988-997.

6. De la Fuente-Núñez, C.; Reffuveille, F.; Fernández, L., et al., Bacterial biofilm development as a multicellular adaptation: antibiotic resistance and new therapeutic strategies. *Current opinion in microbiology* **2013,** *16* (5), 580-589.

7. Frost, I.; Smith, W. P.; Mitri, S., et al., Cooperation, competition and antibiotic resistance in bacterial colonies. *The ISME journal* **2018,** *12* (6), 1582-1593.

8. Yan, J.; Bassler, B. L., Surviving as a community: antibiotic tolerance and persistence in bacterial biofilms. *Cell host & microbe* **2019,** *26* (1), 15-21.

9. Stelzer, E. H., Light-sheet fluorescence microscopy for quantitative biology. *Nature methods* **2015,** *12* (1), 23-26.

10. Power, R. M.; Huisken, J., A guide to light-sheet fluorescence microscopy for multiscale imaging. *Nature methods* **2017,** *14* (4), 360-373.

11. Voleti, V.; Patel, K. B.; Li, W., et al., Real-time volumetric microscopy of in vivo dynamics and large-scale samples with SCAPE 2.0. *Nature methods* **2019,** *16* (10), 1054-1062.

12. Mimori-Kiyosue, Y., Imaging mitotic processes in three dimensions with lattice light-sheet microscopy. *Chromosome Research* **2021**, 1-14.

13. Rosenberg, J.; Cao, G.; Borja-Prieto, F., et al., Lattice light-sheet microscopy multi-dimensional analyses (LaMDA) of T-cell receptor dynamics predict T-cell signaling states. *Cell systems* **2020,** *10* (5), 433-444. e5.

14. Manley, H. R.; Potter, D. L.; Heddleston, J. M., et al., Frontline Science: Dynamic cellular and subcellular features of migrating leukocytes revealed by in vivo lattice lightsheet microscopy. *Journal of leukocyte biology* **2020,** *108* (2), 455-468.

15. Yordanov, S.; Neuhaus, K.; Hartmann, R., et al., Single-objective high-resolution confocal light sheet fluorescence microscopy for standard biological sample geometries. *Biomedical optics express* **2021,** *12* (6), 3372-3391.

16. Qin, B.; Fei, C.; Bridges, A. A., et al., Cell position fates and collective fountain flow in bacterial biofilms revealed by light-sheet microscopy. *Science* **2020**, eabb8501.

17. Parthasarathy, R., Monitoring microbial communities using light sheet fluorescence microscopy. *Current opinion in microbiology* **2018,** *43*, 31-37.

18. Heintzmann, R.; Huser, T., Super-Resolution Structured Illumination Microscopy. *Chemical Reviews* **2017,** *117* (23), 13890-13908.

19. Gustafsson, M. G.; Shao, L.; Carlton, P. M., et al., Three-dimensional resolution doubling in wide-field fluorescence microscopy by structured illumination. *Biophysical journal* **2008,** *94* (12), 4957-4970.

20. Weigert, M.; Schmidt, U.; Boothe, T., et al., Content-aware image restoration: pushing the limits of fluorescence microscopy. *Nature methods* **2018,** *15* (12), 1090-1097.

21. Chen, J.; Sasaki, H.; Lai, H., et al., Three-dimensional residual channel attention networks denoise and sharpen fluorescence microscopy image volumes. *Nature Methods* **2021,** *18* (6), 678-687.

22. Moen, E.; Bannon, D.; Kudo, T., et al., Deep learning for cellular image analysis. *Nat Methods* **2019**.

23. Jeckel, H.; Drescher, K., Advances and opportunities in image analysis of bacterial cells and communities. *FEMS Microbiology Reviews* **2020**.

24. Zhang, M.; Zhang, J.; Wang, Y., et al., Non-invasive single-cell morphometry in living bacterial biofilms. *Nature communications* **2020,** *11* (1), 1-13.

25. Wang, J.; Batabyal, T.; Zhang, M., et al. In *LCuts: linear clustering of bacteria using recursive graph cuts*, 2019 IEEE International Conference on Image Processing (ICIP), IEEE: 2019; pp 1575-1579.

26. Stringer, C.; Wang, T.; Michaelos, M., et al., Cellpose: a generalist algorithm for cellular segmentation. *Nature Methods* **2021,** *18* (1), 100-106.

27. Weigert, M.; Schmidt, U.; Haase, R., et al. In *Star-convex polyhedra for 3d object detection and segmentation in microscopy*, Proceedings of the IEEE/CVF Winter Conference on Applications of Computer Vision, 2020; pp 3666-3673.

28. Scherr, T.; Löffler, K.; Böhland, M., et al., Cell segmentation and tracking using CNN-based distance predictions and a graph-based matching strategy. *Plos One* **2020,** *15* (12), e0243219.

29. Meyer, F.; Beucher, S., Morphological segmentation. *Journal of visual communication and image representation* **1990,** *1* (1), 21-46.

30. Otsu, N., A threshold selection method from gray-level histograms. *IEEE transactions on systems, man, and cybernetics* **1979,** *9* (1), 62-66.

31. Laasmaa, M.; Vendelin, M.; Peterson, P., Application of regularized Richardson–Lucy algorithm for deconvolution of confocal microscopy images. *Journal of microscopy* **2011,** *243* (2), 124-140.

32. Valm, A. M.; Cohen, S.; Legant, W. R., et al., Applying systems-level spectral imaging and analysis to reveal the organelle interactome. *Nature* **2017,** *546* (7656), 162.

33. Chen, B.-C.; Legant, W. R.; Wang, K., et al., Lattice light-sheet microscopy: imaging molecules to embryos at high spatiotemporal resolution. *Science* **2014,** *346* (6208).

34. Thormann, K. M.; Saville, R. M.; Shukla, S., et al., Initial Phases of biofilm formation in Shewanella oneidensis MR-1. *J Bacteriol* **2004,** *186* (23), 8096-104.

35. Gao, R.; Asano, S. M.; Upadhyayula, S., et al., Cortical column and whole-brain imaging with molecular contrast and nanoscale resolution. *Science* **2019,** *363* (6424), eaau8302.

36. Schindelin, J.; Arganda-Carreras, I.; Frise, E., et al., Fiji: an open-source platform for biological-image analysis. *Nature methods* **2012,** *9* (7), 676-682.

37. Pettersen, E. F.; Goddard, T. D.; Huang, C. C., et al., UCSF ChimeraX: Structure visualization for researchers, educators, and developers. *Protein Science* **2021,** *30* (1), 70-82.

38. Parslow, A.; Cardona, A.; Bryson-Richardson, R. J., Sample drift correction following 4D confocal time-lapse imaging. *Journal of visualized experiments: JoVE* **2014,** (86).

39. Rudge, T. J.; Steiner, P. J.; Phillips, A., et al., Computational modeling of synthetic microbial biofilms. *ACS synthetic biology* **2012,** *1* (8), 345-352.

40. Reshes, G.; Vanounou, S.; Fishov, I., et al., Cell shape dynamics in Escherichia coli. *Biophysical journal* **2008,** *94* (1), 251-264.

41. Starruß, J.; Peruani, F.; Jakovljevic, V., et al., Pattern-formation mechanisms in motility mutants of Myxococcus xanthus. *Interface focus* **2012,** *2* (6), 774-785.

42. Venkateswaran, K.; Moser, D. P.; Dollhopf, M. E., et al., Polyphasic taxonomy of the genus Shewanella and description of Shewanella oneidensis sp. nov. *International Journal of Systematic and Evolutionary Microbiology* **1999,** *49* (2), 705-724.

43. Yan, T.; Richardson, C. J.; Zhang, M., et al., Computational correction of spatially variant optical aberrations in 3D single-molecule localization microscopy. *Optics express* **2019,** *27* (9), 12582-12599.

44. He, K.; Zhang, X.; Ren, S., et al. In *Deep residual learning for image recognition*, Proceedings of the IEEE conference on computer vision and pattern recognition, 2016; pp 770-778.

45. Zunair, H.; Rahman, A.; Mohammed, N., et al. In *Uniformizing techniques to process CT scans with 3D CNNs for tuberculosis prediction*, International Workshop on PRedictive Intelligence In MEdicine, Springer: 2020; pp 156-168.

46. Van der Walt, S.; Schönberger, J. L.; Nunez-Iglesias, J., et al., scikit-image: image processing in Python. *PeerJ* **2014,** *2*, e453.

47. Liao, P.-S.; Chen, T.-S.; Chung, P.-C., A fast algorithm for multilevel thresholding. *J. Inf. Sci. Eng.* **2001,** *17* (5), 713-727.

48. Tinevez, J.; Cao, Y., Simple tracker. *MATLAB Cent File Exc* **2016**.

49. Jaccard, P., The distribution of the flora in the alpine zone. 1. *New phytologist* **1912,** *11* (2), 37-50.

50. Wang, J.; Zhang, M.; Zhang, J., et al., Graph-Theoretic Post-Processing of Segmentation With Application to Dense Biofilms. *IEEE Transactions on Image Processing* **2021,** *30*, 8580-8594.

51. Csurka, G.; Larlus, D.; Perronnin, F., et al. In *What is a good evaluation measure for semantic segmentation?*, Bmvc, 2013; p 10.5244.

52. Matula, P.; Maska, M.; Sorokin, D. V., et al., Cell Tracking Accuracy Measurement Based on Comparison of Acyclic Oriented Graphs. *PLoS One* **2015,** *10* (12), e0144959.

53. Zhang, J.; Zhang, M.; Wang, Y., et al., Optically Accessible Microfluidic Flow Channels for Noninvasive High-Resolution Biofilm Imaging Using Lattice Light Sheet Microscopy. *The Journal of Physical Chemistry B* **2021**.

54. Liu, R.; Jia, J. In *Reducing boundary artifacts in image deconvolution*, 2008 15th IEEE International Conference on Image Processing, IEEE: 2008; pp 505-508.

55. Starck, J.-L.; Pantin, E.; Murtagh, F., Deconvolution in astronomy: A review. *Publications of the Astronomical Society of the Pacific* **2002,** *114* (800), 1051.

56. Tinevez, J., SIMPLETRACKER a simple particle tracking algorithm that can deal with gaps. *Jean-Yves Tinevez* **2012**.

57. Ulman, V.; Maska, M.; Magnusson, K. E. G., et al., An objective comparison of cell-tracking algorithms. *Nat Methods* **2017,** *14* (12), 1141-1152.

58. Wen, C.; Miura, T.; Voleti, V., et al., 3DeeCellTracker, a deep learning-based pipeline for segmenting and tracking cells in 3D time lapse images. *Elife* **2021,** *10*, e59187.

59. Zhang, M.; Zhang, J.; Wang, Y., et al., Non-Invasive Single-Cell Morphometry in Living Bacterial Biofilms, GitHub Repository: BCM3D, DOI:10.5281/zenodo.4088658. 2020.

60. Magnusson, K. E.; Jalden, J.; Gilbert, P. M., et al., Global linking of cell tracks using the Viterbi algorithm. *IEEE Trans Med Imaging* **2015,** *34* (4), 911-29.

61. Moen, E.; Borba, E.; Miller, G., et al., Accurate cell tracking and lineage construction in live-cell imaging experiments with deep learning. *bioRxiv* **2019**, 803205.

62. Qin, B.; Fei, C.; Bridges, A. A., et al., Cell position fates and collective fountain flow in bacterial biofilms revealed by light-sheet microscopy. *Science* **2020,** *369* (6499), 71-77.

Chapter 6 Imaging the Effect of Bile Salts on Biofilm Formation of *Shigella flexneri*

6.1 Introduction

Shigella flexneri is an intracellular pathogen that causes watery or bloody diarrhea by invading colonic epithelial cells[1, 2]. Though many aspects of the *S. flexneri* invasion process have been thoroughly studied, there is a significant knowledge gap in how the bacterium survives during host gastrointestinal transit, where it is exposed to numerous hazardous factors such as antimicrobial peptides, proteases, and, particularly, bile salts in the small intestine[3-8]. As an essential component of digestion, the amphipathic structure of bile salts results in detergent-like properties that provide antimicrobial activity by compromising bacterial membrane integrity[9]. Many enteric pathogens including *S. flexneri*, however, can exploit bile salts as cues to adjust virulence traits[6, 10]. Pope et al. first reported that *S. flexneri* shows increased adherence to HeLa cells after exposure to the bile salt deoxycholate [11]. Faherty et al. further identified the *S. flexneri* effectors required for bile-induced bacterial adherence, OspE1 and OspE2 proteins[12]. IcsA is another factor that was found to promote hyper-adhesiveness and invasion upon DOC exposure[7].

Recent studies have also hypothesized that *S. flexneri* may use biofilm formation as a survival strategy in the presence of bile salts[4, 13]. Though biofilm formation is a commonly adaptive trait of microorganisms under harsh conditions, previous studies have shown that *S. flexneri* lacks various adherence factors thought to be important for biofilm formation, including type 1 fimbria, flagella, and Type IV pilus[13, 14]. Thus, this observation may suggest alternative mechanisms utilized by microorganisms in biofilm formation. However, current studies of *S. flexneri* biofilms are limited to static culture conditions and ensemble-level analysis, due to the lack of high

resolution, non-invasive 3D imaging techniques and cellular level image analysis pipelines. To characterize biofilm formation of *S. flexneri* in the presence of bile salts, an experiment performed at biologically relevant conditions with single-cell information of live *S. flexneri* biofilms is necessary.

Here, we imaged biofilm formation of *S. flexneri* under media flow in the presence and absence of bile salts by combining lattice light sheet microscopy (**Chapter 2**), a microfludic system (**Chapter 3**) and deep-learning based image analysis (**Chapter 4** and **5**). Preliminary experiments and cellular level analysis of image data have shown that *S. flexneri* exhibits a higher degree of aggregation in the presence of bile salts, matching with previous studies performed at the static culture conditions[4, 13].

6.2 Materials and Methods

6.2.1 Flow channel operation

Spectinomycin resistant *S. flexneri 2457T* expressing mCherry (pMMB vector, IPTG inducible) were cultured at 37 °C overnight in LB medium with 100 μg/ml spectinomycin. Overnight cultures were diluted 100 times into the LB and induced with 4mM IPTG. Diluted cultures were grown to an optical density at 600 nm (OD_{600}) of 0.4 – 1.0, and then diluted to OD_{600} = 0.05 in 25 % TSB medium containing 100 μg/ml spectinomycin and 4mM IPTG with or without 0.4% bile salts (Fisher Scientific) before channel inoculation (details of the channel were shown in **Chapter 3**). For the results reported in this study, a 3 mm square coverslip coated with poly-L-lysine was set on the bottom of the upper channel. The channel was then sterilized using 70% ethanol and rinsed with ddH2O (double distilled water). The channel was then inoculated with live bacterial cell cultures using a syringe. After inoculation, the channel was mounted on a piezo

nanopositioning stage (Mad City Labs, NanoOP100HS) and immersed in a sucrose solution in the basin. The sucrose solution concentration (~1.5 % w/v) used in the basin was determined by matching the refractive index of the growth media, which was 1.3347 and 1.3345 for 25% TSB with and without 0.4% bile salts, respectively. The temperature of the basin media was kept at 37 °C. The channel inlet port was connected to a syringe pump (Harvard Apparatus, Model 22) and the channel outlet port was connected to a waste container using PVC tubing. Before initiating media flow through the channel, cells were given an hour to attach to the poly-l-lysine coated coverslip. Then, the flow rate was increased to 0.5 ml/h for 20 minutes to flush away non-adherent cells. The flow rate was reduced to 0.03 ml/h for the duration of imaging.

A 560 nm light sheet was used to excite mCherry fluorescence. Images were acquired every 30 minutes. At each time point, a 3D image stack containing 301 2D slices was recorded using a 235 nm step size between slices. Each slice was acquired with a short 10 ms exposure time to reduce motion blur from loosely attached and therefore wiggling cells.

6.2.2 Raw data processing

Raw data processing was accomplished using the same procedure as described in **4.2.2 Raw data processing**, which includes deskewing and rotation of image data. All processed data have the same volume; 51 x 51 x 12 μm^3. ChimeraX was used to render 3D image volumes [15].

6.2.3 Bacterial cell segmentation

Cell segmentation was accomplished with *BCM3D 2.0* (**Chapter 5**). The pre-trained model for processing *E. coli* biofilms was applied to infer cells in the convolutional neural network module of *BCM3D 2.0.* The pre-trained model for *E. coli* was amenable for *S. flexneri*, because they have a similar cell shape and size. 3D rendering of segmentation results was performed by 3D Viewer in ImageJ[16].

6.3 Results and discussion

We acquired 3D image stacks of *S. flexneri* every thirty minutes for 6 hours under media flow in the presence and absence of bile salts separately. As shown in **Figure 6.1**, *S. flexneri* continued to grow at both conditions, but a quick visual inspection shows that the cells are more densely packed when bile salts are present in the medium. To quantify the difference in growth, we analyzed the 3D image stacks using cell segmentation.

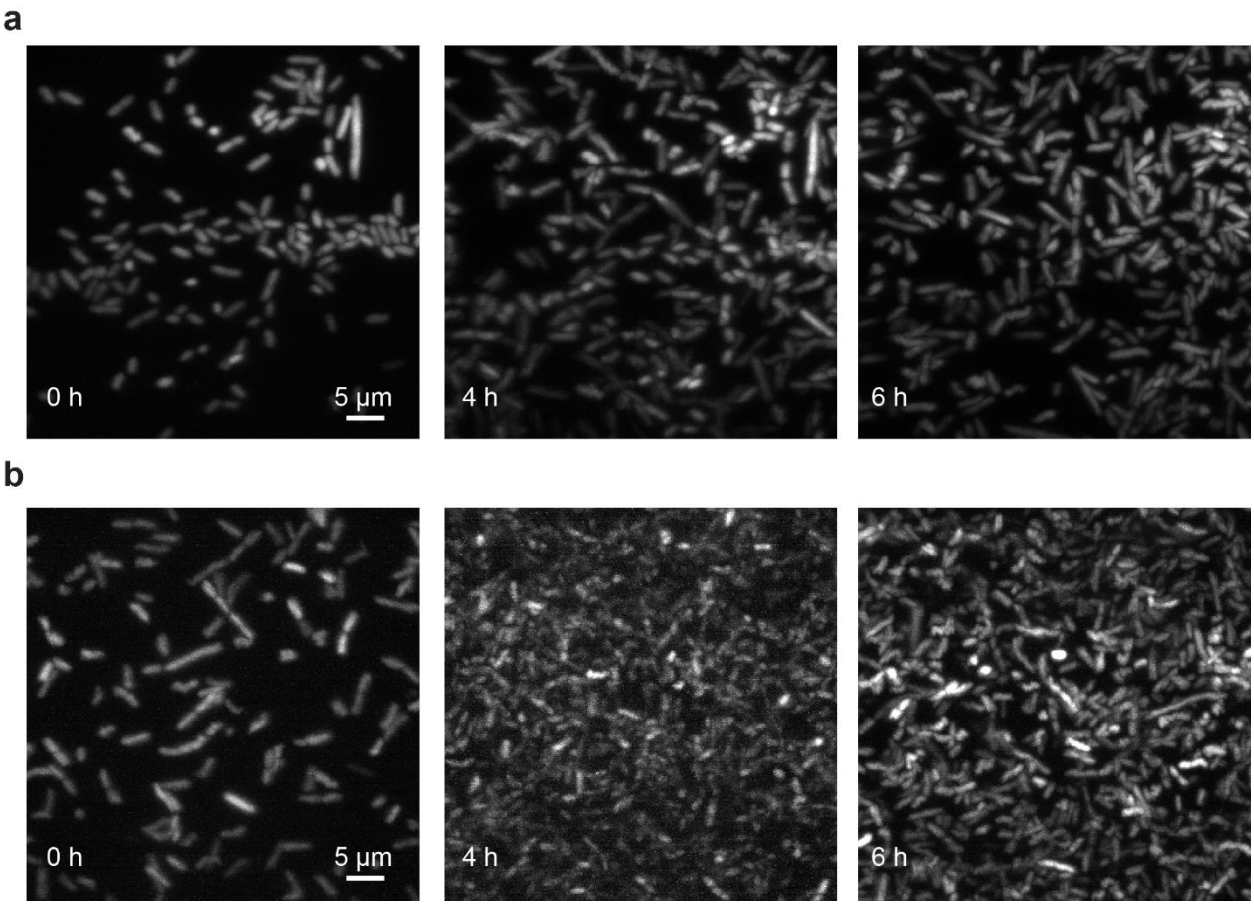

Figure 6.1 Live imaging of mCherry expressing *S. flexneri*. (a) Maximum intensity projections showing the initial 6 hours of *S. flexneri* development under fluid flow without bile salts. (b) Maximum intensity projections showing the initial 6 hours of *S. flexneri* development under media flow with 0.4% bile salts.

Segmentation results show that there are 172 cells in the medium without bile salts and 203 cells in the medium with 0.4% bile salts at the initial time-point, indicating a similar initial density of *S. flexneri* growth at both conditions. After 6 hours, the number of cells increased to 1229 under fluid flow in the presence of 0.4% bile salts, while this number only increased to 464 in the absence of bile salts. Previous studies[4] have shown that growth of *S. flexneri* is not significantly altered with 0.4% bile salts. Thus, we hypothesize that the difference in cell number is due to increased aggregation of cells within the field of view. This is supported by previous studies which have shown that *S. flexneri* more easily aggregate in the presence of bile salts which were performed in previous static culture experiments and ensemble analysis[4, 13]. We further analyzed the structure difference between *S. flexneri* aggregates formed after 6 hours of continuous flow with/without 0.4% bile salts (**Figure 6.2ab**). Using the segmentation results, we calculated the Euclidean distance between each cell to its nearest neighbor using cells centroids. The median value of the nearest neighbor distance in the presence of bile salts is ~23% smaller than the one formed in the absence of bile salts (1.48 μm vs 1.92 μm) (**Figure 6.2cd**), which demonstrates that *S. flexneri* is more densely packed when there are bile salts in the medium. We also analyzed the distance between each cell to the substrate surface. Here we used 10 cells that have the lowest z position as a proxy of the substrate surface. The median value of this distance in the presence of bile salts is ~15% larger than the one in absence of bile salts (4.52 μm vs 3.92 μm) (**Figure 6.2ef**), which indicates *S. flexneri* aggregate formed in the presence of bile salts is thicker.

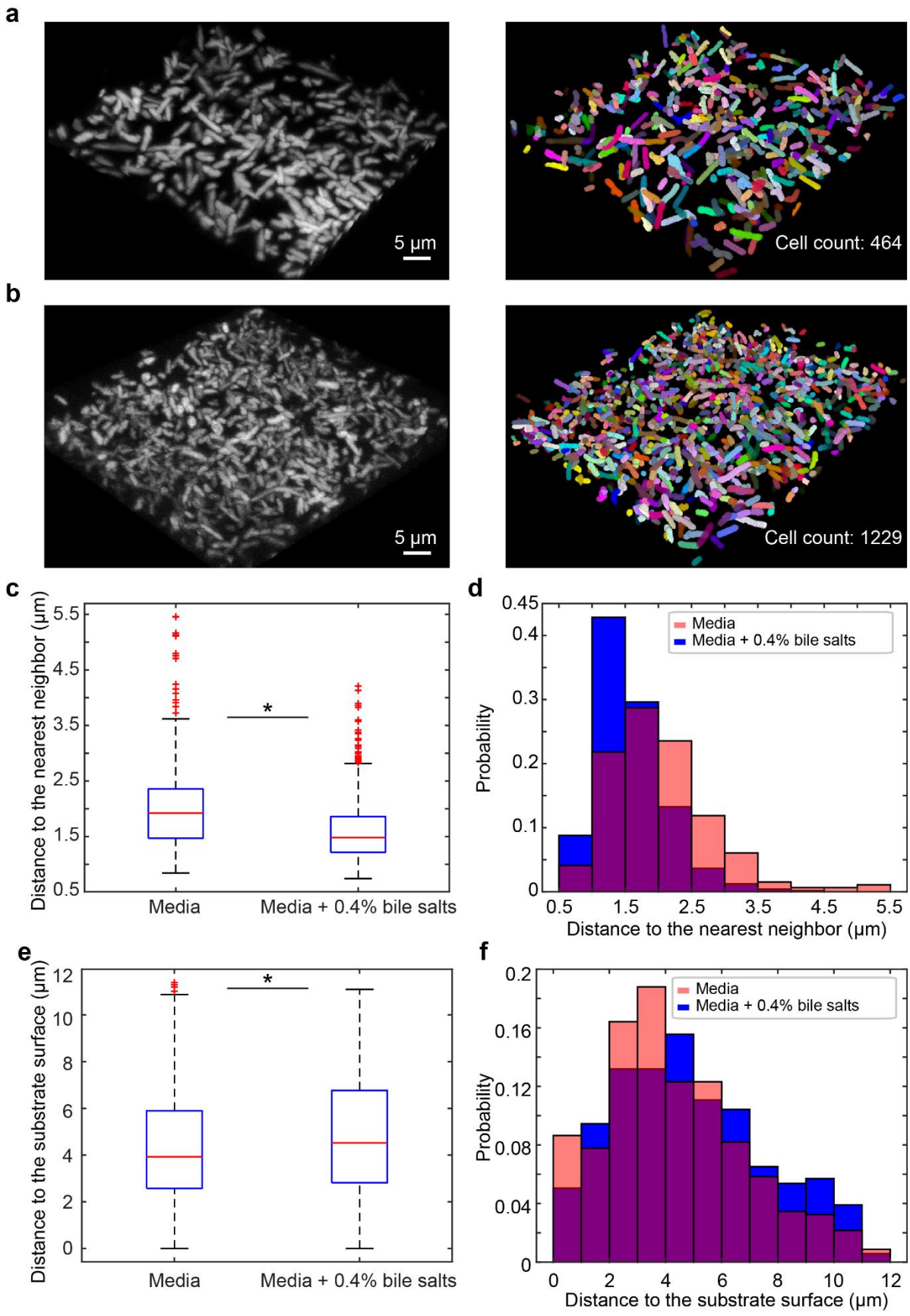
a
5 μm
Cell count: 464
b
5 μm
Cell count: 1229
c
Distance to the nearest neighbor (μm)
5.5
4.5
3.5
2.5
1.5
0.5
*
Media
Media + 0.4% bile salts
d
Probability
0.45
0.4
0.3
0.2
0.1
0
Media
Media + 0.4% bile salts
0.5
1.5
2.5
3.5
4.5
5.5
Distance to the nearest neighbor (μm)
e
Distance to the substrate surface (μm)
12
10
8
6
4
2
0
*
Media
Media + 0.4% bile salts
f
Probability
0.2
0.16
0.12
0.08
0.04
0
Media
Media + 0.4% bile salts
0
2
4
6
8
10
12
Distance to the substrate surface (μm)

Figure 6.2 Quantitative analysis of *S. flexneri* aggregates after 6 hours of continuous growth with and without bile salts. (a) 3D rendering of *S. flexneri* aggregation in the absence of bile salts and its corresponding segmentation result. (b) 3D rendering of *S. flexneri* aggregation in the presence of 0.4% bile salts and its corresponding segmentation result. (c and d) Comparison of the distance to the nearest neighboring cell. (e and f) Comparison of cell distance to the substrate surface. Welch's t-test was applied for statistical analysis using MATLAB. *, P value of <0.01.

6.4 Conclusions and future directions

S. flexneri has long been a major concern in public health, as Shigellosis caused by *S. flexneri* and other *Shigella* species leads to millions of deaths each year[17]. Though many aspects of the *S. flexneri* invasion process have been thoroughly studied, *S. flexneri* use of biofilm formation as a survival strategy during host gastrointestinal transit, especially when there are bile salts present, has only been described in recent studies[4, 13, 14]. In this study, we characterize biofilm formation of *S. flexneri* under media flow in the presence and absence of bile salts through our home-built LLSM and custom flow system. Due to the high spatiotemporal resolution and minimal phototoxicity provided by the LLSM and the optically accessible channel, cellular resolution time-lapse images for live *S. flexneri* were obtained. Cellular level information was extracted using *BCM3D 2.0*. Our preliminary results indicate that *S. flexneri* exhibited a higher degree of aggregation and packed more densely in the media containing bile salts.

Currently, mechanisms governing this phenomenon are largely unknown. Köseoğlu et al. suggest that IcsA, an outer membrane protein required for *S. flexneri* actin-based motility during intracellular infection, plays an important role in aggregative growth of *S. flexneri* in the presence of bile salts by promoting cell-cell contact[13]. Chanin et al. proposed that though *S.flexneri* lacks fimbriae or other traditional adherence factors in common laboratory media, it still produces at

least three potential adherence structures (long polar fimbriae-like structure, type 1 fimbriae-like structure, curli-like structure) in the presence of bile salts, which contribute to biofilm formation[14]. However, all these experiments were performed in static culture conditions and lack cellular information for live biofilms. With the method we proposed in this study, these hypotheses could be tested at the cellular level by imaging live *S. flexneri* biofilms in the future. Another extension of this work could incorporate human organoid-derived epithelia into the flow system, yielding a so-called gut-on-a-chip model[18-20], thus enabling the study of *S. flexneri* in a more biologically relevant condition.

References

1. Jennison, A. V.; Verma, N. K., Shigella flexneri infection: pathogenesis and vaccine development. *FEMS microbiology reviews* **2004,** *28* (1), 43-58.

2. Pizarro-Cerdá, J.; Charbit, A.; Enninga, J., et al. In *Manipulation of host membranes by the bacterial pathogens Listeria, Francisella, Shigella and Yersinia*, Seminars in cell & developmental biology, Elsevier: 2016; pp 155-167.

3. Bernardini, M. L.; Mounier, J.; d'Hauteville, H., et al., Identification of icsA, a plasmid locus of Shigella flexneri that governs bacterial intra-and intercellular spread through interaction with F-actin. *Proceedings of the National Academy of Sciences* **1989,** *86* (10), 3867-3871.

4. Nickerson, K. P.; Chanin, R. B.; Sistrunk, J. R., et al., Analysis of Shigella flexneri resistance, biofilm formation, and transcriptional profile in response to bile salts. *Infection and immunity* **2017,** *85* (6), e01067-16.

5. Schroeder, G. N.; Hilbi, H., Molecular pathogenesis of Shigella spp.: controlling host cell signaling, invasion, and death by type III secretion. *Clinical microbiology reviews* **2008,** *21* (1), 134-156.

6. Sistrunk, J. R.; Nickerson, K. P.; Chanin, R. B., et al., Survival of the fittest: how bacterial pathogens utilize bile to enhance infection. *Clinical microbiology reviews* **2016,** *29* (4), 819-836.

7. Zumsteg, A. B.; Goosmann, C.; Brinkmann, V., et al., IcsA is a Shigella flexneri adhesin regulated by the type III secretion system and required for pathogenesis. *Cell host & microbe* **2014,** *15* (4), 435-445.

8. Marteyn, B.; Gazi, A.; Sansonetti, P., Shigella: a model of virulence regulation in vivo. *Gut microbes* **2012,** *3* (2), 104-120.

9. Begley, M.; Gahan, C. G.; Hill, C., The interaction between bacteria and bile. *FEMS microbiology reviews* **2005,** *29* (4), 625-651.

10. Urdaneta, V.; Casadesús, J., Interactions between bacteria and bile salts in the gastrointestinal and hepatobiliary tracts. *Frontiers in medicine* **2017,** *4*, 163.

11. Pope, L. M.; Reed, K. E.; Payne, S. M., Increased protein secretion and adherence to HeLa cells by Shigella spp. following growth in the presence of bile salts. *Infection and immunity* **1995,** *63* (9), 3642-3648.

12. Faherty, C. S.; Redman, J. C.; Rasko, D. A., et al., Shigella flexneri effectors OspE1 and OspE2 mediate induced adherence to the colonic epithelium following bile salts exposure. *Molecular microbiology* **2012,** *85* (1), 107-121.

13. Köseoğlu, V. K.; Hall, C. P.; Rodríguez-López, E. M., et al., The autotransporter IcsA promotes Shigella flexneri biofilm formation in the presence of bile salts. *Infection and immunity* **2019,** *87* (7), e00861-18.

14. Chanin, R. B.; Nickerson, K. P.; Llanos-Chea, A., et al., Shigella flexneri adherence factor expression in in vivo-like conditions. *Msphere* **2019,** *4* (6), e00751-19.

15. Pettersen, E. F.; Goddard, T. D.; Huang, C. C., et al., UCSF ChimeraX: Structure visualization for researchers, educators, and developers. *Protein Science* **2021,** *30* (1), 70-82.

16. Schindelin, J.; Arganda-Carreras, I.; Frise, E., et al., Fiji: an open-source platform for biological-image analysis. *Nature methods* **2012,** *9* (7), 676-682.

17. Kotloff, K. L.; Winickoff, J. P.; Ivanoff, B., et al., Global burden of Shigella infections: implications for vaccine development and implementation of control strategies. *Bulletin of the World Health Organization* **1999,** *77* (8), 651.

18. Kim, H. J.; Huh, D.; Hamilton, G., et al., Human gut-on-a-chip inhabited by microbial flora that experiences intestinal peristalsis-like motions and flow. *Lab on a Chip* **2012,** *12* (12), 2165-2174.

19. Steinway, S. N.; Saleh, J.; Koo, B.-K., et al., Human Microphysiological Models of Intestinal Tissue and Gut Microbiome. *Frontiers in Bioengineering and Biotechnology* **2020,** *8* (725).

20. Tovaglieri, A.; Sontheimer-Phelps, A.; Geirnaert, A., et al., Species-specific enhancement of enterohemorrhagic E. coli pathogenesis mediated by microbiome metabolites. *Microbiome* **2019,** *7* (1).

Chapter 7 Significance and Future Directions

7.1 Significance

As the major mode of microbial life, biofilms have been widely recognized for their impact on the health of higher living organisms, and the global biogeochemical cycling[1]. To enable either efficient suppression of pathogenic biofilm formations or sufficient utilization of beneficial properties of biofilms[2-4], it is necessary to better understand how macroscopic biofilm properties, such as metabolism and geometric shape, emerge from the individual behaviors of cells.

Fluorescence microscopy, combined with high spatial-temporal resolution and highly specific fluorescence probes, provides a unique way to study the spatial and temporal contexts that affect cellular behaviors in biofilm environments. However, confocal microscopy, the current standard approach to 3D fluorescence imaging, suffers from limitations in acquisition speeds and photodamage[5]. To resolve these limitations, we have utilized lattice light sheet microscopy (LLSM), a newly developed imaging technique that effectively combines excellent spatial-temporal resolution and minimal photodamage, into this study. A LLSM integrated microfluidic system was developed to sustain bacterial biofilm growth for multiple days under precisely controllable physical and chemical conditions. With these tools, we successfully recorded the colonization of glass surfaces by *S. oneidensis* MR-1 biofilms, a well-studied biofilm formation species, under media flow over a time period of three days, visualizing the evolution of single surface-attached cells into a large 3D biofilm at cellular level. Furthermore, the combination of these tools enabled the study of live *S. flexneri* biofilms, an intracellular pathogen that causes watery or bloody diarrhea, at biologically relevant conditions with single cell resolution.

After the acquisition of fluorescence images, the extraction of quantitative information from such images is crucial. In order to quantitatively analyze biofilm-dwelling cells, each individual cell needs to be detected from images, and this is typically referred to as segmentation. In this study, Bacterial Cell Morphometry 3D (*BCM3D*), an integrated image analysis package that combines deep learning with conventional image analysis, and its novel extension version *BCM3D 2.0* were developed. Biologically reasonable segmentation results were obtained for various biofilms even when they contained thousands of densely packed bacterial cells. With these high-performance image analysis pipelines, we demonstrated that the presence of bile salts leads to aggregation of *S. flexneri* at the cellular level, whereas similar results have only been shown at ensemble level before[6, 7].

7.2 Future directions

The combination of the LLSM and the LLSM integrated microfluidic system has proven powerful for noninvasive four-dimensional (4D) imaging of bacterial biofilms at single-cell resolution. Though this combination has only been applied to the study of single-species biofilms in this study, we envision that, it can also be applied to the study of multi-species biofilms using the multi-color imaging ability of our home-built LLSM (three excitation wavelengths now, and could be further increased)[8, 9]. Another extension of this technology could utilize biotic substrates in the microfluidic system. We envision that, with minor modifications, the current microfluidic design can be adapted to image bacterial populations interacting with human organoid-derived epithelia, which have recently been stably reconstituted in dual-channel microphysiological devices[10, 11]. Thus, the system could be used to model the gut microbiome or pathogenesis or gut-colonizing bacteria.

It is important to note that the information derived from imaging data is reliant on a robust analysis system. The performance of *BCM3D* and *BCM3D 2.0* is currently limited by the quality of training data. The current simulated images lack some characteristics of experimentally obtained images, such as unevenly distributed background as well as position-related resolution and contrast. Therefore, an important direction of this work is developing novel simulation methods that can produce realistic and accurate simulated data that more closely resemble microscopy images. Fortunately, recently developed deep learning based image transfer methods, such as CycleGAN, have shown potential for achieving this goal[12, 13]. At present, our simulation of bacterial cells only allows for rod- or spherical- shaped cells which limits its applicability to other model systems, such as the comma-shaped *Vibrio cholerae*. To further improve the generality of the proposed imaging analysis pipeline,[14] we can further modify the simulation algorithm to include other cell shapes and sizes.

Future work for *S. flexneri* has been discussed in details in **Chapter** 6. Briefly, we will probe the biofilm formation mechanism of *S. flexneri* in the presence of bile salts at cellular level.

7.3 Summary

The work presented here enables long duration cellular level imaging of live bacterial biofilms under precisely controllable physical and chemical conditions by combining the homebuilt LLSM and the custom microfluidic system. *BCM3D* and its extension version *BCM3D 2.0* were developed to achieve quantitative image analysis at the single cell level. With these tools, we were able to image and analyze aggregation of *S. flexneri* in the presence of bile salts at the cellular level. In summary, these novel research tools enable us to study the emergent properties of bacterial biofilms in terms of the fully-resolved behavioral phenotypes of individual cells.

References

1. Flemming, H.-C.; Wingender, J.; Szewzyk, U., et al., Biofilms: an emergent form of bacterial life. *Nature Reviews Microbiology* **2016,** *14* (9), 563-575.

2. Verderosa, A. D.; Totsika, M.; Fairfull-Smith, K. E., Bacterial biofilm eradication agents: a current review. *Frontiers in chemistry* **2019,** *7*, 824.

3. Logan, B. E., Exoelectrogenic bacteria that power microbial fuel cells. *Nature Reviews Microbiology* **2009,** *7* (5), 375-381.

4. Zhao, C.-e.; Gai, P.; Song, R., et al., Nanostructured material-based biofuel cells: recent advances and future prospects. *Chemical Society Reviews* **2017,** *46* (5), 1545-1564.

5. Stelzer, E. H., Light-sheet fluorescence microscopy for quantitative biology. *Nature methods* **2015,** *12* (1), 23-26.

6. Köseoğlu, V. K.; Hall, C. P.; Rodríguez-López, E. M., et al., The autotransporter IcsA promotes Shigella flexneri biofilm formation in the presence of bile salts. *Infection and immunity* **2019,** *87* (7), e00861-18.

7. Nickerson, K. P.; Chanin, R. B.; Sistrunk, J. R., et al., Analysis of Shigella flexneri resistance, biofilm formation, and transcriptional profile in response to bile salts. *Infection and immunity* **2017,** *85* (6), e01067-16.

8. Lee, K. W. K.; Periasamy, S.; Mukherjee, M., et al., Biofilm development and enhanced stress resistance of a model, mixed-species community biofilm. *The ISME journal* **2014,** *8* (4), 894-907.

9. Røder, H. L.; Sørensen, S. J.; Burmølle, M., Studying bacterial multispecies biofilms: where to start? *Trends in microbiology* **2016,** *24* (6), 503-513.

10. Steinway, S. N.; Saleh, J.; Koo, B.-K., et al., Human Microphysiological Models of Intestinal Tissue and Gut Microbiome. *Frontiers in Bioengineering and Biotechnology* **2020,** *8* (725).

11. Tovaglieri, A.; Sontheimer-Phelps, A.; Geirnaert, A., et al., Species-specific enhancement of enterohemorrhagic E. coli pathogenesis mediated by microbiome metabolites. *Microbiome* **2019,** *7* (1).

12. Fu, C.; Lee, S.; Joon Ho, D., et al. In *Three dimensional fluorescence microscopy image synthesis and segmentation*, Proceedings of the IEEE conference on computer vision and pattern recognition workshops, 2018; pp 2221-2229.

13. Ma, Z.; Wang, F.; Wang, W., et al., Deep learning for in vivo near-infrared imaging. *Proceedings of the National Academy of Sciences* **2021,** *118* (1).

14. Deng, X.; Sarkar, R.; Labruyere, E., et al. In *Modeling Shape Dynamics During Cell Motility in Microscopy Videos*, 2020 IEEE International Conference on Image Processing (ICIP), IEEE: 2020; pp 2491-2495.